Synthesis And Characterization of Copper Zinc Tin Sulfide Nanoparticles And Thin Films

A DISSERTATION

SUBMITTED TO THE FACULTY OF THE GRADUATE SCHOOL

OF THE UNIVERSITY OF MINNESOTA

BY

Ankur Khare

IN PARTIAL FULFILLMENT OF THE REQUIREMENTS

FOR THE DEGREE OF

DOCTOR OF PHILOSOPHY

Eray S. Aydil, Co-Adviser

David J. Norris, Co-Advisor

June, 2012

Acknowledgements

I am deeply indebted to my advisors, Prof. Eray S. Aydil and Prof. David J. Norris, for their invaluable guidance throughout my stay here as a graduate student. They have been a great source of support and inspiration for me, and have helped me grow up as a qualified PhD from an inexperienced undergraduate. My advisors have been very liberal in allowing me to choose my own research topics and do the research I truly liked, while guiding me along to avoid the pitfalls.

I am grateful to all the Aydil and Norris group members past and present who have helped me with my work. In particular, I am grateful to Dr. Andrew Wills, Dr. Michael Behr, Dr. Bin Liu, Dr. Kurtis Leschkies, Boris Chernomordik, Selin Tosun, and Melissa Johnson for their invaluable help. I am also grateful to the other group members, Neema Rastgar, Sriharsha Jayanti, Brian Merrit, Jonathan Hubbard, and Xin Zhang for creating a lively and enjoyable workplace.

I would also like to express my gratitude towards the undergraduates who helped me with my work: Tessie Panthani, Lauren Ammerman, and Matthew Shea. In addition, I would like to thank my collaborators, Prof. Matteo Cococcioni, and Dr. Burak Himmetoglu, for their patience in teaching me DFT calculations and helping me at various stages of computational work.

Finally, I am forever indebted to my family for their constant encouragement and support at every stage of my life. Without them, I would not have been what I am today.

Abstract

Copper zinc tin sulfide (Cu_2ZnSnS_4, or CZTS) is emerging as an alternative material to the present thin film solar cell technologies such as $Cu(In,Ga)Se_2$ and CdTe. All the elements in CZTS are abundant, environmentally benign, and inexpensive. In addition, CZTS has a band gap of ~1.5 eV, the ideal value for converting the maximum amount of energy from the solar spectrum into electricity. CZTS has a high absorption coefficient ($>10^4$ cm^{-1} in the visible region of the electromagnetic spectrum) and only a few micron thick layer of CZTS can absorb all the photons with energies above its band gap. CZT(S,Se) solar cells have already reached power conversion efficiencies >10%.

One of the ways to improve upon the CZTS power conversion efficiency is by using CZTS quantum dots as the photoactive material, which can potentially achieve efficiencies greater than the present thin film technologies at a fraction of the cost. However, two requirements for quantum-dot solar cells have yet to be demonstrated. First, no report has shown quantum confinement in CZTS nanocrystals. Second, the syntheses to date have not provided a range of nanocrystal sizes, which is necessary not only for fundamental studies but also for multijunction photovoltaic architectures.

We resolved these two issues by demonstrating a simple synthesis of CZTS, Cu_2SnS_3, and alloyed $(Cu_2SnS_3)_x(ZnS)_y$ nanocrystals with diameters ranging from 2 to 7 nm from diethyldithiocarbamate complexes. As-synthesized nanocrystals were characterized using high resolution transmission electron microscopy, X-ray diffraction, Raman spectroscopy, and energy dispersive spectroscopy to confirm their phase purity. Nanocrystals of diameter less than 5 nm were found to exhibit a shift in their optical absorption spectra towards higher energy consistent with quantum confinement and previous theoretical predictions.

Thin films from CZTS nanocrystals deposited on Mo-coated quartz substrates using drop casting were found to be continuous but highly porous. Annealing CZTS nanocrystal films at temperatures as low as 400°C led to an intense grain growth;

however, thin films from CZTS nanocrystals cracked on annealing due to their high porosity. Although quantum confinement in CZTS is only accessible in nanocrystals of diameters less than 5 nm, the high volume of the ligands as compared to the volume of the nanocrystals makes it a challenge to deposit continuous compacted thin films from small nanocrystals.

Films deposited from thermal decomposition of a stoichiometric mix of metal dithiocarbamate complexes were found to be predominantly CZTS. These films from complexes were found to be continuous but microporous. The diameter of the spheres making up the microporous structure could be changed by changing the anneal temperature. The structural composition of the final film could be altered by changing the heating rate of the complexes.

CZTS exists in three different crystal structures: kesterite, stannite, and pre-mixed Cu-Au (PMCA) structures. Due to the similarity in the crystal structures, it is extremely difficult to distinguish them based on X-ray diffraction. We computed the phonon dispersion curves for the three structures using *ab-initio* calculations, and found characteristic discontinuities at the Γ-point which can potentially be used to distinguish the three. In addition, the Γ-point phonon frequencies, which correspond to the Raman peak positions, for the three structures were found to be shifted from each other by a few wavenumbers. By deconvoluting the experimental Raman spectra for both CZTS and $Cu_2ZnSnSe_4$ (CZTSe) using Gaussian peaks, we observed that the most intense Raman scattering peak in both CZTS and CZTSe is a sum of two different peaks which correspond to scattering from their respective kesterite and stannite phases.

The electronic, structural, and vibrational properties of a series of CZTS-CZTSe alloys (CZTSSe) were studied using *ab-initio* calculations. The S-to-Se ratio and the spatial distribution of the anions in the unit cell were found to determine the energy splitting between the electronic states at the top of the valence band and the hole mobility in CZTSSe alloys and solar cells. X-ray diffraction patterns and phonon distribution curves were found to be sensitive to the local anion ordering. The predicted Raman

scattering frequencies and their variation with x agree with experimentally determined values and trends.

Table of Contents

List of Tables

List of Figures

Chapter 1
Introduction

1.1 The Need for Renewable Energy

According to recent studies, the global demand for energy is expected to increase by approximately 50% within the next 25 years.[1] Currently, >80% of the world's energy is being produced by burning fossil fuels such as coal, oil, and natural gas. These fuels produce greenhouse gases upon combustion. In addition, the energy produced from these sources is becoming expensive. Solar energy is abundant, non-polluting, and can provide a significant fraction of the world's energy demand.

A solar cell is a device which can convert sunlight into electricity. All the world's energy demand can be met if we cover only 0.1% of the earth's surface with about 10% efficient solar cells. In spite of this great potential, energy derived from solar cells comprised only about 0.005% of the total energy produced in the US in 2010.[2] The present bottle neck to widespread use of solar cells is their production and installation cost.[3] The most commonly used solar panels are made from high purity, crystalline silicon. Processing silicon is expensive and increases the overall cost of production of the solar panels.

Thin film solar cells are emerging as an alternative technology to silicon-based solar cells. In these devices, thin (~1 μm) films of semiconductor materials such as cadmium telluride (CdTe) and copper indium gallium diselenide (CIGS) are used in lieu of a thick (~100 μm) silicon wafer. As the absorption coefficient of typical thin film absorber materials is ~100 times higher than crystalline silicon, a 100 times thinner layer of thin film materials can absorb an equivalent amount of energy as crystalline silicon. In addition, purity and crystal quality requirements on thin film solar cell materials are less stringent than in crystalline silicon solar cells, as the grain boundaries in thin films

materials enhance charge separation and transport, and permit only negligible recombination.[4] Thus, thin film solar cells are cheaper to produce than silicon solar cells.

Although thin film solar cells such as those based on CIGS and CdTe have already achieved impressive power conversion efficiencies of about 15-20% in the laboratory, the semiconductor materials commonly used for their production are either toxic (*e.g.*, cadmium) or rare in the earth's crust (*e.g.*, indium, tellurium). Both the cost and abundance of these materials in the earth's crust are plotted in Figure 1.1. For long term viability of thin films solar cells, we need alternative materials that are non-toxic and abundant in the earth's crust. One such material is copper zinc tin sulfide (Cu_2ZnSnS_4; commonly known as CZTS). CZTS is made of copper, zinc, tin, and sulfur which are very abundant in the earth's crust, inexpensive, and environmentally benign.[5,6] In addition, CZTS has a band gap of ~1.5 eV, the ideal value for converting the maximum amount of energy from the solar spectrum into electricity.[7] CZTS also has a high absorption coefficient (> 10^4 cm^{-1} in the visible region of the electromagnetic spectrum) and only a few micron thick layer of CZTS can absorb all the photons with energies above its band gap.

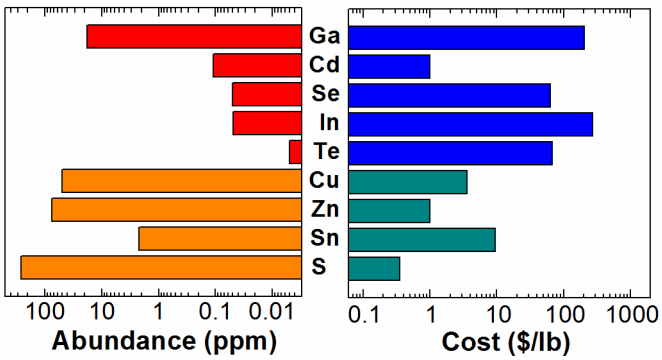

Figure 1.1 A comparison of the abundance in the earth's crust and cost of the various elements used for manufacturing thin film solar cells. Data is plotted on a logarithmic scale.

Thin film solar cells are commonly fabricated using vacuum deposition techniques such as sputtering or co-evaporation, which contribute significantly to their

production cost. Moreover, throughputs can be low. Casting films from colloidal dispersions of semiconductor nanocrystals is an alternative to vacuum deposition.[8] Nanocrystals are small crystals of semiconductor materials with diameters on the order of 1 to 100 nanometers. They can be dispersed in various solvents such as toluene as shown in Figure 1.2. Such dispersions are also referred to as inks and they can be used in ultrahigh throughput roll-to-roll deposition techniques such as slot coating under atmospheric conditions. Thin films from nanocrystals can be annealed to form thin polycrystalline films suitable for solar cell fabrication. Such production techniques are expected to lower the cost of thin film solar cells significantly. Solar cells made using nanocrystal inks have been shown to match or even excel the efficiencies of devices made by vacuum based deposition techniques.[9,10]

Figure 1.2 CZTS nanocrystals dispersed in toluene.

Another approach to making CZTS solar cells from nanocrystal dispersions is to develop nanostructured CZTS. Semiconductor nanocrystals (or colloidal quantum dots) have been proposed as a general route to high-efficiency, low-cost photovoltaic devices.[11,12] Nanocrystals that are smaller than a characteristic length known as the exciton Bohr radius are called quantum dots.[13] These nanocrystals are so small that their radial dimensions control their electronic properties through an effect known as quantum confinement. These materials, due to quantum confinement, exhibit optical properties that are tunable with nanocrystal size. In materials where the electronic levels can be changed through composition and quantum confinement, one can independently control both the effective band gap, and the location of the lowest unoccupied electronic level

(*e.g.*, electron affinity). Thus, multilayered devices containing films of quantum dots of different sizes could yield inexpensive multijunction solar cells.[14] Further, quantum dots can potentially allow the Shockley-Queisser power-conversion limit for Si (31%) to be exceeded up to 66% through multiple exciton generation[15-17] or hot-electron extraction.[18] However, the best quantum-dot solar cells to date[17,19] have utilized lead chalcogenide nanocrystals that do not satisfy sustainability goals. There are very few reports of quantum dot solar cells from abundant nontoxic materials. In particular, it is difficult to simultaneously control the stoichiometry and size for quaternary semiconductors such as CIGS or CZTS, making it a challenge to synthesize quantum dots of these materials.

1.2 Quantum Confinement in Semiconductor Quantum Dots

The carriers (electrons or holes) in a semiconductor begin to feel confined by the material boundaries when the size of the semiconductor becomes smaller than their Bohr radius. This phenomenon is known as quantum confinement. A nanoscale particle exhibiting quantum confinement is referred to as a quantum dot (QD). The continuous density of states in bulk semiconductors become discrete and quantized in quantum dots.

The effective bandgap of a semiconductor QD as a function of radius R is given by[20]

$$E_g^{QD}(R) = E_g + \frac{\hbar^2\pi^2}{2R^2}\left[\frac{1}{m_e} + \frac{1}{m_h}\right] - \frac{1.8e^2}{\varepsilon R} \qquad (1.1)$$

where E_g is the bandgap for the bulk semiconductor, ħ is Plank's constant, m_e and m_h are the effective masses of the electron and the hole, respectively, and ε is the dielectric constant of the material. The second term on the right hand side of Eq. (1.1) is the kinetic energy term and increases as R^{-2} on decreasing the QD radius, R. The third term on the right hand side of Eq. (1.1) arises due to the Coulomb attraction between the electron and the hole, and increases as R^{-1} with decreasing R. Although the decrease of coulomb

attraction counteracts the increase in kinetic energy on decreasing R, for sufficiently small R, the kinetic energy term in Eq. (1.1) dominates the coulomb attraction term. Due to this, the effective bandgap of a QD widens with decreasing radius, and the optical emission and absorption associated with electronic transitions across the band gap shift towards higher energy, a phenomenon known as 'blue shift'. Quantum confinement effects permit the manipulation of the bandgap of QDs of a given material simply by changing their size. This property can be exploited to tune the absorption spectra of a given material to the solar radiation and enable the fabrication of multijunction solar cells.

1.3 Thesis Overview

CZTS is emerging as a new promising material for thin film photovoltaics. In spite of the great potential associated with the material, there is a lack of understanding regarding the control of nanocrystal diameter. Although different syntheses have yielded nanocrystals of different diameters, there is no one synthesis that can give nanocrystals over a range of sizes. In addition, the nanocrystal diameters accessed by most of the syntheses lie in the range 10-20 nm, which is beyond the Bohr diameter for CZTS (<5 nm).

Chapter two describes the progression of CZTS thin film solar cells beginning with the first demonstration of a CZTS heterodiode with CdS in 1988 by Ito and Nakazava[21] to the recently reported 10.1% efficient CZTS solar cell from the group at the IBM T.J. Watson Research Centre.[9] CZTS thin film solar cells from both vacuum-deposition and solution based processing techniques are described. In addition, I also discuss the recent advances in CZTS synthesis through synthetic chemistry.

Chapter three describes the synthesis of Cu_2ZnSnS_4 (CZTS), Cu_2SnS_3 (CTS), and alloyed $(Cu_2SnS_3)_x(ZnS)_y$ nanocrystals of diameters ranging from 2-5 nm from diethyldithiocarbamate complexes. As-synthesized nanocrystals are characterized using

high resolution transmission electron microscopy, X-ray diffraction, Raman spectroscopy, and energy dispersive spectroscopy to confirm the presence of only a single phase of CZTS/CTS. Nanocrystals of diameter less than 5 nm exhibited a shift in their optical absorption spectra towards higher energy consistent with quantum confinement and previous theoretical predictions. This is the first report on size control and quantum confinement in any quaternary semiconductor material. This chapter has been published as Ankur Khare, Andrew W. Wills, Lauren Ammerman, David J. Norris, and Eray S. Aydil, "Size Control and Quantum Confinement in Cu_2ZnSnS_4 Nanocrystals", Chem. Comm. **47**, 11721 (2011).

Chapter four describes thin film deposition using colloidal dispersion of CZTS nanocrystals using drop casting and doctor blading. We could deposit crack free films from colloidal dispersion of CZTS nanocrystals using drop casting. However, the deposited films look porous under scanning electron microscope. CZTS nanocrystal films on annealing become compact at temperatures as low as 400°C and films showed intense grain growth in anneal times as short as five minutes. However, the nanocrystal films cracked on annealing due to the initial porosity of the deposited films. Depositing thin films from larger diameter nanocrystals was surmised to be the key factor in giving compact films after annealing.

Chapter five describes the facile synthesis of microporous films of CZTS beginning with metal dithiocarbamate complexes. Metal diethyldithiocarbamates were found to melt before they decomposed. Annealing films deposited from metal dithiocarbamate complexes in argon atmosphere gave smooth, microporous CZTS films consisting of densely packed micron sized spheres. By changing the anneal temperature, we could vary the diameter of the microspheres from ~100 nm to 1-2 μm.

CZTS and $Cu_2ZnSnSe_4$ (CZTSe) exist in three different crystal structures depending on the arrangement of the metal cations within the tetrahedral holes of the sulfur anion FCC lattice. These three structures have been predicted to have different band gaps and can co-exist at a given temperature due to having similar lattice energies.

Due to the similarity in the crystal structures, it is difficult to distinguish between the three based on X-ray diffraction patterns. In chapter six, I simulate the Raman spectra for the three different structures of CZTS and CZTSe using density functional theory (DFT) calculations. Simulated phonon spectra for the three structures of CZTS showed characteristic discontinuities at the Γ-point due to a difference in longitudinal and transverse optical phonon energies (LO-TO splitting) along different directions. The calculated Raman scattering peak positions for the three structures were found to be shifted from each other by a few wavenumbers. The most intense Raman scattering peak of CZTS and CZTSe thin film samples, on deconvolution, was found to be composed of two different peaks whose peak positions closely matched to that computed using DFT calculations. Raman spectroscopy in conjunction with ab-initio calculations was found to be useful in predicting the structure of a given CZTS/CZTSe thin film sample. This chapter has been published as Ankur Khare, Burak Himmetoglu, Melissa Johnson, David J. Norris, Matteo Cococcioni, and Eray S. Aydil, "Calculation of the lattice dynamics and Raman spectra of copper zinc tin chalcogenides and comparison to experiments" J. Appl. Phys., **111**, 083707 (2012).

The best CZTS solar cells have been fabricated using CZTS-CZTSe alloys instead of phase-pure CZTS or CZTSe; however, the electronic and structural properties of CZTS-CZTSe alloys have not received equal attention as CZTS or CZTSe. In particular, understanding how the anion arrangement affects the properties of CZTSSe alloys is important for improving solar cells based on these materials. In chapter seven, I studied the structural, electronic, and vibrational properties of $Cu_2ZnSn(S_{1-x}Se_x)_4$ alloys as a function of x using ab initio computational methods. I found that the S-to-Se ratio and anion distribution determined the energy splitting between the electronic states at the top of the valence band and the hole mobility in CZTSSe alloys and solar cells. The X-ray diffraction patterns and phonon dispersion curves were also found to be sensitive to the local anion ordering. The predicted Raman scattering frequencies and their behavior with x was found to agree with experimentally determined values and trends. Manipulating anion ordering was found to be one of the possible ways to change the electronic

properties of the synthesized $Cu_2ZnSn(S_{1-x}Se_x)_4$ thin films. This chapter has been published as Ankur Khare, Burak Himmetoglu, Matteo Cococcioni, and Eray S. Aydil, "First principles calculation of the electronic properties and lattice dynamics of $Cu_2ZnSn(S_{1-x}Se_x)_4$" J. Appl. Phys., **111**, 123704 (2012).

1.4 References

1 U.S. Energy Information Administration, *International Energy Outlook* (U.S. Department of Energy, Washington, DC, 2011).

2 U.S. Energy Information Administration, *Annual Energy Outlook* (U.S. Department of Energy, Washington, DC, 2011).

3 C. Wadia, A. P. Alivisatos, and D. M. Kammen, Environ. Sci. Technol. **43**, 2072 (2009).

4 J. B. Li, V. Chawla, and B. M. Clemens, Adv Mater **24**, 720 (2012).

5 D. B. Mitzi, O. Gunawan, T. K. Todorov, K. Wang, and S. Guha, Sol. Energy Mater. Sol. Cells **95**, 1421 (2011).

6 H. Katagiri, Thin Solid Films **480-481**, 426 (2005).

7 W. Shockley, and H. J. Queisser, J. Appl. Phys. **32**, 510 (1961).

8 M. G. Panthani, V. Akhavan, B. Goodfellow, J. P. Schmidtke, L. Dunn, A. Dodabalapur, P. F. Barbara, and B. A. Korgel, J. Am. Chem. Soc. **130**, 16770 (2008).

9 D. A. R. Barkhouse, O. Gunawan, T. Gokmen, T. K. Todorov, and D. B. Mitzi, Prog. Photovolt: Res. Appl. **20**, 6 (2012).

10 Q. Guo, G. M. Ford, W. Yang, B. C. Walker, E. A. Stach, H. W. Hillhouse, and R. Agrawal, J. Am. Chem. Soc. **132**, 17384 (2010).

11 W. U. Huynh, J. J. Dittmer, and A. P. Alivisatos, Science **295**, 2425 (2002).

12 A. Kongkanand, K. Tvrdy, K. Takechi, M. Kuno, and P. V. Kamat, J. Am. Chem. Soc. **130**, 4007 (2008).

13 V. I. Klimov, Nanocrystal Quantum Dots, (CRC Press, 2009).

14 T. Franzl, T. A. Klar, S. Schietinger, A. L. Rogach, and J. Feldmann, Nano Lett. **4**, 1599 (2004).

15 A. Nozik, Physica E: Low-Dimensional Systems and Nanostructures **14**, 115 (2002).

16 J. B. Sambur, T. Novet, and B. A. Parkinson, Science **330**, 63 (2010).

17 O. E. Semonin, J. M. Luther, S. Choi, H. Chen, J. Gao, A. J. Nozik, and M. C. Beard, Science **334**, 1530 (2011).

18 W. A. Tisdale, K. J. Williams, B. A. Timp, D. J. Norris, E. S. Aydil, and X. Y. Zhu, Science **328**, 1543 (2010).

19 A. Pattantyus-Abraham, I. J. Kramer, A. R. Barkhouse, X. Wang, G. Konstantatos, R. Debnath, L. Levina, I. Raabe, M. K. Nazeeruddin, M. Grätzel, and E. H. Sargent, ACS Nano **4**, 3374 (2010).

20 L. E. Brus, J. Chem. Phys. **80**, 4403 (1984).

21 K. Ito, and T. Nakazawa, Jpn. J. Appl. Phys. **27**, 2094 (1988).

Chapter 2
Review of the Existing Status of CZTS Thin-Film Solar Cell Technology

In this chapter, I will review the evolution of the record efficiency for CZTS solar cell along with the progress made towards the fabrication of CZTS thin films and solar cells using both vacuum-based and solution-based deposition techniques.

2.1 Evolution of CZTS Thin Film Solar Cell Efficiency

The first report on CZTS appeared in 1978 in which Hall *et al.* reported the X-ray diffraction pattern for the natural mineral kesterite and stannite, and established them to be structurally similar but distinct minerals.[1] The first report on the photovoltaic response of CZTS appeared in 1988, where Ito and Nakazawa of Shinshu University, Japan fabricated a heterodiode based on the junction between CZTS and cadmium tin oxide (CTO) thin films on a stainless steel substrate. The reported CZTS thin film was fabricated using argon beam sputtering from pressed targets of CZTS and the device gave an open circuit voltage of 165 mV. Ito and Nakazava clarified the bandgap of CZTS to be 1.45 eV, an optimum value for the photoabsorber layer of a single junction solar cell.[2] In 1996, Katagiri *et al.* from Nagaoka National College of Technology, Japan published the first device characteristics of a CZTS thin film solar cell. The solar cell, having the structure ZnO:Al/CdS/CZTS/Mo/SLG(soda lime glass), gave a power conversion efficiency of 0.66% and an open circuit voltage of 400 mV.[3] The CZTS layer in this device was synthesized by sulfidation of a Cu/Sn/Zn stack deposited using electron beam deposition. Friedlmeier *et al.* from Stuttgart University, Germany, in 1997, reported a 2.3% efficient CZTS solar cell with an open circuit voltage of 470 mV.[4] The solar cell had a device structure similar to one fabricated by Katagiri *et al.* with the exception of the

CZTS layer being synthesized by the sulfidation of co-deposited Cu-Zn-Sn films. Katagiri *et al.* set a new record for CZTS device efficiency of 2.63% in 1999 by changing the way they sulfidized the Cu/Sn/ZnS stacks.[5] In 2003, Katagiri *et al.* reported CZTS solar cells with conversion efficiencies of 5.45%.[6] The boost in efficiency was a result of using an improved sulfidation chamber (a stainless steel chamber fitted with a turbo pump as compared to quartz glass tube furnace fitted with a rotary pump) which permitted the use of a higher vacuum during sulfidation; this reduced the contamination from the residual gas. Soaking CZTS thin films in deionized water (DI) was found to preferentially etch metal oxide particles in the CZTS layer. Soaking in DI water helped in increasing the device efficiency to 6.7%, which was the highest efficiency reported till 2010.[7] Mitzi *et al.* in 2010 reported 9.6% efficient solution processed CZTSSe solar cells.[8] The CZTSSe thin films for these devices were deposited by spin-coating a precursor solution in hydrazine followed by sulfidation or partial selenization (for increasing the spectral photoresponse). The device efficiency was recently improved to 10.1%, which currently is the record efficiency for CZTSSe thin film solar cells.[9] The progression of device efficiencies for CZTS(Se) solar cells has been plotted in Figure 2.1.

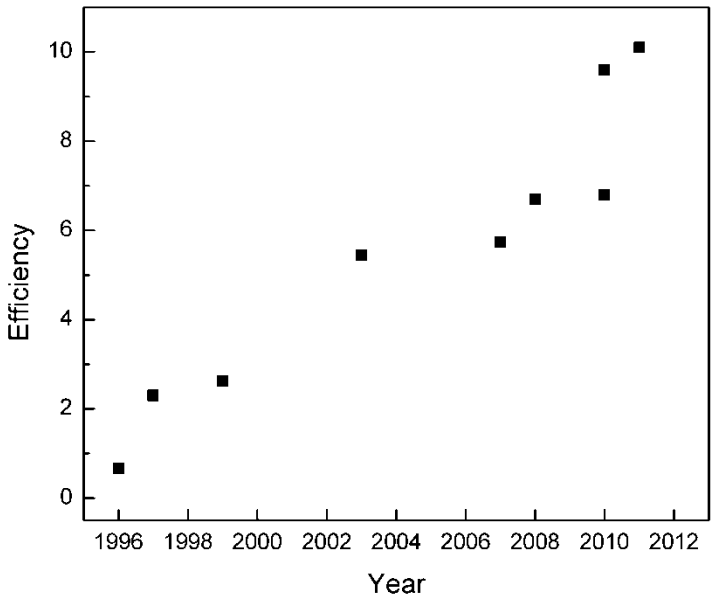

Figure 2.1 Evolution of the record efficiency of CZTS(Se) solar cells vs. year.

2.2 CZTS Thin Film Deposition Techniques

CZTS thin films have been deposited using various techniques such as sputtering, evaporation, spin coating from precursor solution, spray pyrolysis, *etc.* These thin film deposition techniques can be broadly divided into two major categories: vacuum-based techniques and solution-based techniques. In the following section, we will discuss the advances that have been made for the various thin film deposition techniques and the best solar cells fabricated from each of them.

2.2.1 Vacuum-Based Techniques

The vacuum-based approaches mainly involve thin film deposition using sputtering and evaporation. CZTS thin films are typically fabricated by high temperature sufidation of stacks of metals, metal sulfides, or a combination of the two. These processes are typically slow and may require up to several hours for thin film deposition and annealing. Vacuum-based deposition techniques typically give films with controlled stoichiometry and potentially high uniformity.

2.2.1.1 Evaporation

CZTS thin films from evaporation were first reported by Katagiri *et al.* in 1996 by sulfidation of a stack of Cu/Sn/Zn in N_2+H_2S (5%) at 500°C.[3] These solar cells were 0.66% efficient. By a careful analysis of the stoichiometry of the sulfidized films, it was found that long heat treatment re-evaporated the volatile zinc. These cells were improved upon by replacing Zn with ZnS and increasing the annealing temperature to 550°C, which resulted in 2.62% efficient devices.[10] Katagiri *et al.* also reported that replacing Zn with ZnS in the initial precursor stack significantly improved the adhesion of the final film to the Mo/SLG substrate.[11] Further improvements in the devices were made by improving the annealing chamber (replacing the quartz glass tube furnace and rotary pump with a steel chamber and turbo pump), using CdI_2 instead of $CdSO_4$ for CdS deposition, and controllably Na-doping the CZTS films by introducing a Na_2S layer in

between the ZnS precursor layer and Mo. These improvements gave 5.45% efficient solar cells with an open circuit voltage (V_{OC}) of 582 mV and short circuit current (J_{SC}) of 15.5 mA/cm^2.[6] Katagiri *et al.* had trouble with the surface morphology of the 5.45% efficient solar cell reported earlier, which led them to explore different combinations of the precursor stacks to make devices with smoother CZTS layer. In particular, it was found that the use of multiple periods of Cu/SnS_2/ZnS stacks gave final CZTS films with smoother morphology as compared to a Cu/Sn/ZnS stack. The improvement in film morphology is surmised to be from better intermixing of the initial precursors and increased initial sulfur content of the precursor layer (due to replacement of Sn with SnS_2).[12]

Friedlmeier *et al.* from Stuttgart University reported 2.3% efficient CZTS devices from co-evaporation on heated substrates. The substrate temperature was varied between 300 and 600°C. Cu, ZnS, SnS_2 or Sn, and S served as the sources for CZTS films. Films fabricated at substrate temperatures higher than 400°C were found to lose significant amounts of Sn by re-evaporation.[4] Tanaka *et al.* observed that CZTS thin films fabricated by co-evaporation from Cu, Zn, Sn, and S precursors show a preferential orientation along the [112] plane. In the temperature range 400-600°C, grain size was found to increase with substrate temperature.[13] In a later study, Tanaka *et al.* studied the effect of thin film composition on the structural properties of the final film. In the range $0.82 \leq Cu/(Zn+Sn) \leq 1.28$, a higher Cu/(Zn+Sn) ratio was found to result in larger grains. The Cu-rich and Sn-rich films were found to be unsuitable for solar cell applications due to their very low resistivity.[14]

Recently, fast co-evaporation of CZTS thin films has been explored in order to make the thin film deposition more viable for commercial manufacturing. In particular, Schubert *et al.* explored the possibility of depositing CZTS thin films by fast co-evaporation of a Cu-rich film from ZnS, Cu, Sn, and S sources onto a substrate held at 550°C. The as-synthesized thin film had a CuS phase in addition to CZTS, which was removed using a KCN etch. Thin films obtained after a KCN etch had Cu:Zn:Sn≈2:1:1

and the devices made using these films were found to be 4.1% efficient with a V_{OC}, J_{SC}, and fill factor (FF) of 541 mV, 13.0 mA/cm^2, and 59.8%, respectively.[15] In a separate study, Wang *et al.* from IBM fabricated CZTS thin films by co-evaporation from Cu, Zn, Sn, and S sources on a relatively low temperature substrate (110°C), followed by a reactive S anneal on a hot plate at 540°C for a few minutes. The fabricated thin film solar cells had an efficiency of 6.8%, the highest for a pure sulfide CZTS solar cell and had V_{OC}, J_{SC}, and FF of 587 mV, 17.8 mA/cm^2, and 65%, respectively. The CZTS thin film in the reported device had a thickness of only 660 nm. The short reaction time used in the fabrication of the CZTS thin film may be responsible in reducing re-evaporation from the film.[16]

Bar *et al.* have recently reported the effect of KCN etching on the surface properties of CZTS thin films. In particular, KCN etch causes a preferential etching of Cu, and to some extent Sn, and increases the surface bandgap from 1.53 eV to 1.91 eV.[17] In a separate study, the authors studied the effect of oxidation on the surface properties of CZTS thin films, and observed the native oxidation of Sn, Zn, and S (in order of prevalence) on air exposure of the thin films. The surface was found to be Cu-poor and was interpreted to be composed of a Cu-free surface species such as $ZnSnS_3$, or a mixture of ZnS and SnS_2.[18] The ability to tune the surface states by etching or native oxidation was surmised to be a useful tool for the development of future high efficiency CZTS solar cells.

2.2.1.2 Sputtering

Ito and Nakazawa in 1988 employed an argon beam sputtering technique to deposit CZTS thin films from pressed targets of CZTS. They reported CZTS bandgap to be 1.45 eV. This was the first report on the photovoltaic effect of CZTS and the CZTS-cadmium tin oxide heterojunction gave a V_{OC} of 165 mV.[2] Tanaka *et al.* fabricated CZTS thin films by annealing heated Cu/Zn/Sn (bottom) stacks in S flux. Films sputtered on a substrate at room temperature followed by a high temperature anneal were found to peel off easily. However, sputtering on heated substrates followed by S anneals at the same

temperature gave well-adhesive films. Stoichiometric CZTS films were obtained for substrate temperatures less than 400°C. However, the loss of Zn at high temperatures (due to the high vapor pressure of Zn) gave Zn-poor films at temperatures above 450°C. Using ZnS instead of Zn in the initial stack was suggested as a solution to this problem.[19]

The best solar cells using sputtering have been fabricated by Katagiri *et al.* Through reactive co-sputtering of Cu, SnS, and ZnS in H_2S atmosphere (20%), Katagiri *et al.* fabricated a 5.74% efficient CZTS solar cell.[20] The sample was rotated (20 rpm) while sputtering the precursors for fine intermixing and uniformity of the precursors. It was found that Cu/(Zn+Sn)=0.87, Zn/Sn=1.15, and S/(Cu+Zn+Sn)=1.18 gave the best devices. Later, it was also reported that soaking these films in deionized water prior to CdS deposition resulted in preferential etching of metal oxide particles in the CZTS layer. This improved the device efficiency further to 6.77%, giving the most efficient pure sulfide CZTS devices to date.[7] Katagiri *et al.* also explored the effect of variation of Cu:Zn:Sn ratio on CZTS device performance and published a useful composition map for CZTS absorbers. It was observed that highly efficient CZTS solar cells are only obtained in a narrow composition range around Zn/Sn≈1.25 and Cu/(Zn+Sn)≈0.9.[21] In addition, the variation of H_2S concentration from 5% to 20% was found to have little effect on device properties, thereby suggesting the use of lower H_2S concentration for anneals to reduce the wear of the sulfidation chamber.

Fernandes *et al.* studied the effect of variation of the initial precursor stack on the final film properties and found Cu/Sn/Zn stack to give better quality films as compared to Cu/Zn/Sn stack.[22] Momoseo *et al.* fabricated CZTS thin films from the sulfidation of co-sputtered metallic precursors under elemental sulfur atmosphere. They observed that films annealed in low S vapor pressure (0.1 atm) for over 40 min did not adhere strongly to the substrate and exhibited large voids. In contrast, films annealed at high S vapor pressure (1.5 atm) for 7 min adhered strongly to the substrate and gave larger crystal grains. The solar cells prepared with films annealed at 1.5 atm S vapor pressure were 3.7% efficient.[23] On replacing the n-type CdS layer with ZnO in CZTS solar cells, Htay

et al. obtained a 4.29% efficient solar cell; this efficiency was found to be comparable to that obtained using conventional CdS layer (4.31%). The use of wide bandgap ZnO enhanced the V_{OC} and improved the quantum efficiency for wavelengths less than 510 nm.[24]

Edoff *et al.* have studied the effect of using ZnS precursor instead of Zn on the CZTS thin film/device properties. Using ZnS gave smoother films with fewer voids and decreased Sn losses. However, these films had a smaller grain size as compared to films using Zn. The authors hypothesized the early nucleation in films sputtered from S containing precursors as the cause behind the same.[25] Chalapathy *et al.* fabricated CZTS thin films via S annealing a Cu/ZnSn/Cu precursor stack and found the final thin film morphology to be sensitive to the annealing temperature. In particular, annealing at 560°C gave a bi-layer morphology whereas the one annealed at 580°C did not. The authors reported 4.59% efficient CZTS solar cells.[26]

2.2.1.3 Pulsed Laser Deposition (PLD)

The first CZTS solar cell using PLD was fabricated by Moriya *et al.* where they used KrF laser pulses to ablate a CZTS target. The substrate was held at room temperature during thin film deposition. The CZTS films were post annealed in N_2 atmosphere for an hour for grain growth. Interestingly, the films did not show significant Sn loss as observed in other studies. However, the authors do report the formation of Cu-Sn-S phase along with CZTS. The thin films annealed at 500°C gave 1.74% efficient solar cells.[27] Moholkar *et al.* synthesized CZTS in a way similar to Moriya *et al.* with the exception of annealing the films in an N_2 + H_2S (5%) atmosphere at 400°C. The CZTS devices were 3.14% efficient.[28]

2.2.1.4 Chemical Vapor Deposition (CVD)

Ramasamy *et al.* fabricated the first CZTS thin film using aerosol assisted CVD by using a toluene solution of the diethyldithiocarbamate complexes of Cu, Zn, and an alkyl derivative of Sn. The three complexes were found to decompose in a narrow

temperature range of 280-300°C which facilitated the formation of a single phase of CZTS as compared to multiple phases of ZnS, SnS, and Cu_xS. Stoichiometric control of the final film appeared to be difficult, as films prepared at different substrate temperatures had variable stoichiometry.[29] Washio *et al.* have synthesized CZTS thin films by sulfidation of oxide thin films prepared by open atmosphere CVD. Oxide thin films were annealed for three hours at 520-560°C in an N_2+H_2S (5%) atmosphere. Although all the films showed O-Kα peaks in EDX, the solar cells fabricated using these films were found to be 6.03% efficient. The most efficient devices were obtained with the composition ratios Cu/(Zn+Sn)=0.78 and Zn/Sn=1.29.[30]

2.2.2 Solution-Based Techniques

Solution-based techniques are low-cost, high throughput techniques which are being explored as alternatives to the expensive vacuum-based processing techniques. These techniques have shown tremendous potential for CZTS processing as detailed below.

2.2.2.1 Precursor-Ink Based Approaches:

Direct film formation from precursors is highly attractive for commercial production of CZTS thin films due to its compatibility with high throughput roll-to-roll processing techniques such as wire wound rod coating, slot coating, *etc.*

The first sol-gel synthesis of CZTS thin films was reported by Tanaka *et al.* in 2007. Copper (II) acetate monohydrate, zinc (II) acetate dihydrate, and tin (II) chloride dihydrate were used as the metal sources, and 2-methoxyethanol and monoethanolamine were used as the solvent and the stabilizer, respectively. Thin films from precursor solutions were coated onto soda lime glass (SLG) substrates and annealed at 300°C to dry the films. These films were later annealed at 500°C in an N_2+H_2S (5%) atmosphere for 1 hr. The as-synthesized films were found to have a stoichiometric composition. The XRD pattern matched CZTS and the bandgap was found to be 1.49 eV, which is consistent

with that established for CZTS.[31] Solar cells with films synthesized using a similar approach gave an efficiency of 1.01%. This device, with a structure of glass/Mo/CZTS/CdS/Al:ZnO/Al, also had its transparent conducting oxide layer (AL:ZnO) deposited using sol-gel approach. This made the Al:ZnO layer several orders of magnitude more resistive than that deposited using sputtering and is one of the likely reasons for the relatively poor device performance. This was the first device in which the absorber, the buffer layer, and the TCO were all deposited from solution.[32] By variation of the stoichiometry of the CZTS absorber, the solar cell efficiency was improved to 2.03%. The best solar cell was obtained by using Cu/(Zn+Sn)=0.80 and Zn/Sn=1.15. In addition, it was found that CZTS films deposited using Cu/(Zn+Sn)<0.8 gave large grains.[33] The same group in a later report discussed the effect of annealing temperature on the morphology of the final CZTS thin film. Films annealed at temperatures higher than 450°C had ~ 2μm big CZTS grains. In addition, low temperature annealed films had a contamination from Cu_xS phase, which got eliminated for films annealed at temperatures greater than 500°C.[34] In a separate study, it was found out that H_2S concentration of 3% gave the largest grains and the highest efficiency solar cells for H_2S concentration in the range $3\%<[H_2S]<20\%$.[35]

Todorov *et al.* synthesized suspensions of CZTS particles by reacting metal salts (complexed with triethnolamine) with dissolved elemental sulfur in ethylene glycol at 170°C for 3 hours. The resultant suspensions were coated onto glass substrates and annealed at 550°C for 10 min in sulfur atmosphere. XRD pattern of the synthesized thin films matched CZTS. This approach necessitated the addition of organic binders for the synthesis of crack-free films; however, addition of binders impeded grain growth.[36] In an analogous approach, a precursor film was obtained by spin coating a precursor solution composed of copper acetate hydrate, zinc chloride, tin (II) chloride dihydrate, and thiourea (S source) dissolved in dimethylsulfoxide onto glass substrates and annealing the film at 580°C for 2.5 min on a hot plate inside a glove box. A thicker precursor film obtained after repeating this step several times was annealed in a Se atmosphere at 500°C for 20 min to obtain a CZTSSe film. Devices made from such films were found to be

4.1% efficient. The CZTSSe thin films synthesized by this process did not have any carbon rich layer near the Mo/CZTSSe interface which is typically seen in CZTSSe thin films from nanocrystal dispersions.[37]

Todorov *et al.* from the IBM T.J. Watson Research Center developed a mixed CZTSSe ink from copper (I) sulfide, tin (II) sulfide/selenide, and zinc (II) sulfide/ selenide dissolved in hydrazine. In this approach, Cu and Sn precursors dissolved in hydrazine readily upon the addition of excess chalcogen, whereas the Zn precursor reacted with the metal chalcogenide solution to form solid particles of $ZnS(Se)N_2H_4$. The dissolved components act as binders, thereby eliminating the need for organic binders and the solid particles act as stress relief centers, thereby preventing film cracking. Thin films from precursors deposited on Mo-coated SLG substrates by spin coating were annealed for 5 min on a hot plate in the presence of S for grain growth to give CZTSSe films. Solar cells fabricated from CZTSSe films and having a device structure SLG/Mo/CZTSSe/CdS/ZnO/ITO, were found to be 9.66% efficient and had V_{OC}, J_{SC}, and FF of 516 mV, 28.6 mA/cm^2, and 65%, respectively.[8] The device efficiency was recently improved to 10.1%. This currently stands as the highest efficiency for CZTSSe solar cells. The device efficiency was found to be limited by short minority carrier lifetime, interfacial recombination, and high series resistance.[9] The biggest limitation of this process is the toxicity and high reactivity of hydrazine, which makes it difficult to scale up the process for commercial production. In order to make the devices more viable for large scale manufacturing, the precursor solutions prepared in hydrazine were diluted with an equal amount of water and then used for thin film deposition. Devices made in this manner were 8.1% efficient.[38]

Recently, Woo *et al.* have synthesized CZTS precursor films by spin coating slurries of Cu_2S, Zn, Sn, and S milled in ethanol onto a Mo-coated SLG substrate. Solar cells fabricated from these films annealed in an N_2+H_2S (5%) atmosphere for 30 min at 530°C were found to be 5.14% efficient. The use of low melting point Zn (420°C) and Sn

(231°C) precursors is hypothesized to aid reactive liquid phase sintering between constituent particles and/or intermediate compounds.[39]

2.2.2.2 Nanocrystal Ink Based Approaches

CZTS nanocrystal (NC) based inks were first developed in 2009 with the publication of three reports within a short span of two months. The published syntheses involved nucleation and growth of NCs by the reaction at an elevated temperature of salts of Cu, Zn, and Sn (typically chlorides or acetylacetonates) complexed with oleylamine, with an oleylamine-sulfur complex. The synthesized NCs had diameters in the range 10-20 nm and a bandgap of ~1.5 eV.[40-42] Selenization of doctor bladed thin films from CZTS NCs dispersed in hexanethiol at 500°C for 20 min gave large grained CZTSSe films, with device efficiency of 7.2%. These devices, however, were found to have a carbon-rich layer at the Mo/CZTSSe interface which is responsible for limiting the efficiency of these devices.[43]

CZTS nanorods of diameter ~ 200 nm were synthesized by Shi *et al.* using template directed synthesis with metal chlorides, ethylenediamine, and sulfur/selenium (for CZTS/CZTSe) precursors. The nanowires could be easily extracted by dissolving the template using NaOH solution.[44] Wurtzite phase CZTS nanoprisms and nanoplates have been synthesized recently by replacing oleylamine with dodecanethiol as capping agent. The NCs had a bandgap of 1.4 eV.[45] Singh *et al.* have synthesized wurtzite nanorods of diameter 11 nm and length 35 nm by using a mixture of dodecanethiol and tert-dodecyl mercaptan as capping agents. The nanorods were also assembled into perpendicularly aligned arrays by controlled evaporation from solution.[46] By variation of the stoichiometry of the CZTS NCs, Dai *et al.* varied the bandgap from 1.23 eV to 3.48 eV. The nanocrystal diameter was found to be ~3.5 nm, independent of stoichiometry. Dye sensitized solar cells fabricated from these NCs were found to be 0.03% efficient.[47]

2.2.2.3 Spray Pyrolysis

One of the earliest attempts for non-vacuum deposition of CZTS involved the use of spray pyrolysis. Nakayama and Ito deposited CZTS thin films by spraying a solution of metal chlorides and thiourea (sulfur source) in deionized water onto heated glass substrates at 280-360°C. The as-deposited films from deionized water were found to be significantly S-poor. However, a post-deposition anneal in $Ar+H_2S$ (5%) at 550°C gave a nominally stoichiometric film. Cu-rich films contained traces of Cu_xS whereas Zn-poor films contained Cu_2SnS_3 impurity phase.[48] Madarasz *et al.* studied the thermal decomposition of Cu (I), Zn (II), and Sn (II) thiourea complexes.[49] Kumar *et al.* optimized the deposition process to give a single phase of CZTS without post-anneal by using a substrate temperature of 370°C and an optimized precursor concentration. The films showed a direct bandgap of 1.43 eV, consistent with CZTS.[50] Prabhakar and Jampana found the conductivity of spray deposited CZTS films to increase with Na-diffusion from SLG and Cu-deficiency in the film. The effect of Na-diffusion was found to be more significant than Cu-deficiency and the film conductivity was found to increase by an order of magnitude on using SLG as compared to borosilicate glass.[51]

Rajeshmon *et al.* deposited CZTS thin films from an aqueous solution of cuprous chloride, zinc acetate, stannous/stannic chloride, and thiourea, and found the films synthesized from stannic chloride to have larger grains and higher crystallinity than the ones from stannous chloride. Films synthesized using stannic chloride gave V_{OC} and J_{SC} of 380 mV and 2.40 mA/cm^2, respectively.[52]

2.2.2.4 Electrochemical Deposition

The first CZTS films from electrochemical deposition were synthesized by Scragg *et al.* by annealing a metal stack of Zn/Sn/Cu (bottom) in sulfur atmosphere at 550°C for 2 hours. The solar cells fabricated using these films were found to be 0.8% efficient. The low efficiency was attributed to a high series resistance and a high shunt conductance.[53] It was not possible to get a phase pure CZTS film by this technique even after changing the

stoichiometry of the precursors. Zn/Sn=1 was found to give the best quality films. In addition, annealing in N_2+H_2S (5%) was found to give larger grains.[54] The improvement to the deposition process involved the use of Cu/Sn/Cu/Zn stacks, the use of a rotating disc electrode for sample deposition (for improved large scale uniformity of the deposited films), and a KCN etch to remove the Cu_xS phase. This gave a 3.2% efficient solar cell.[55]

Araki *et al.* synthesized CZTS thin films by annealing co-electrodeposited Cu-Zn-Sn films in S atmosphere for 2 hours. Slightly Zn-rich films gave the best device efficiency of 3.16%. Copper (II) sulfate pentahydrate, zinc sulfate heptahydrate, tin (II) chloride dihydrate, and tri-sodium citrate dihydrate were used for the co-electrodeposition. The co-electrodeposited films did not exhibit any phase separation after annealing.[56] Ennaoui *et al.*, using a similar thin film deposition process, fabricated a 3.4% efficient solar cell. The Cu-Zn-Sn films were annealed in Ar+H_2S (5%) with a total processing time of 8 hrs, which involved a 2 hr. anneal at 550°C. The presence of Zn-rich regions (probably ZnS), Zn-poor regions (probably Cu_2SnS_3), and voids near the Mo/CZTS interface are thought to be responsible in limiting the device efficiency.[57] In-situ X-ray diffraction study of the annealing process for co-electrodeposited films revealed the formation of Cu_2SnS_3 and ZnS which react at a temperature of about 570°C to give a single phase of CZTS. The formation reactions for Cu_2SnS_3 differed for Cu-poor films vs. Cu-rich samples.[58]

Pawar *et al.* have demonstrated a single step co-electrodeposition of S along with the metals by using $CuSO_4$, $ZnSO_4$, $SnSO_4$, and $Na_2S_2O_3$ (sulfur source) in an aqueous electrolytic bath at room temperature. The as-deposited films were annealed in an Ar atmosphere at 550°C for 1 hr. for grain growth and did not require any post deposition sulfidation step. The bandgap of the film annealed at 550°C was found to be 1.50eV.[59]

Ahmed *et al.* recently published a 7.3% efficient CZTS solar cell using electrodeposition which is currently the record efficiency for a pure sulfide CZTS solar cell. CZTS thin films were synthesized from Cu/Zn/Sn or alternately Cu/Sn/Zn stacks via a two-step anneal process: (i) a low-temperature anneal at 210-350°C for forming a

uniform (Cu,Zn) and (Cu,Sn) alloy, and (ii) an anneal of these alloy films at a high temperature of 585°C in a S atmosphere for 15 mins. The CZTS grains in the final films are 1-2 μm. Annealing at temperatures less than 580 °C led to the formation of either a Cu_2S or Cu_2SnS_3 phase in the film. The champion devices had a V_{OC}, J_{SC}, and FF of 567 mV, 22 mA/cm^2, and 58.1%, respectively. The low fill factor was due to the high resistance of the back contact arising from the thick layer of MoS_2 formed during sulfidation.[60]

2.3 References

1 S. R. Hall, J. T. Szymanski, and J. M. Stewart, Can. Mineral. **16**, 131 (1978).
2 K. Ito, and T. Nakazawa, Jpn. J. Appl. Phys. **27**, 2094 (1988).
3 H. Katagiri, N. Sasaguchi, S. Hando, S. Hoshino, J. Ohashi, and T. Yokota, Miyazaki, Japan (1996) pp. 745.
4 T. M. Friedlmeier, N. Wieser, T. Walter, H. Dittrich, and H. W. Schock, Belford, UK (1997) pp. 1242.
5 H. Katagiri, K. Saitoh, T. Washio, H. Shinohara, T. Kurumadani, and S. Miyajima, Sapporo, Japan (1999) pp. 647.
6 H. Katagiri, K. Jimbo, K. Moriya, and K. Tsuchida, Osaka, Japan (2003), pp. 2874.
7 H. Katagiri, K. Jimbo, S. Yamada, T. Kamimura, W. S. Maw, T. Fukano, T. Ito, and T. Motohiro, Appl. Phys. Express **1**, 041201/1 (2008).
8 T. K. Todorov, K. B. Reuter, and D. B. Mitzi, Adv. Mater. **22**, E156 (2010).
9 D. A. R. Barkhouse, O. Gunawan, T. Gokmen, T. K. Todorov, and D. B. Mitzi, Prog. Photovolt: Res. Appl. **20**, 6 (2012).
10 H. Katagiri, K. Saitoh, T. Washio, H. Shinohara, T. Kurumadani, and S. Miyajima, Sol. Energy Mater. Sol. Cells **65**, 141 (2001).
11 H. Katagiri, N. Ishigaki, T. Ishida, and K. Saito, Jpn. J. Appl. Phys. **40**, 500 (2001).
12 H. Katagiri, Thin Solid Films **480-481**, 426 (2005).
13 T. Tanaka, D. Kawasaki, M. Nishio, Q. Guo, and H. Ogawa, Phys. Status Solidi C **3**, 2844 (2006).
14 T. Tanaka, A. Yoshida, D. Saiki, K. Saito, Q. Guo, M. Nishio, and T. Yamaguchi, Thin Solid Films **518**, S29 (2010).
15 B. Schubert, B. Marsen, S. Cinque, T. Unold, R. Klenk, S. Schorr, and H. Schock, Prog. Photovolt: Res. Appl. **19**, 93 (2011).
16 K. Wang, O. Gunawan, T. Todorov, B. Shin, S. J. Chey, N. A. Bojarczuk, D. Mitzi, and S. Guha, Appl. Phys. Lett. **97**, 143508 (2010).

17 M. Bar, B. Schubert, B. Marsen, S. Krause, S. Pookpanratana, T. Unold, L. Weinhardt, C. Heske, and H. Schock, Appl. Phys. Lett. **99**, 152111 (2011).
18 M. Bar, B. Schubert, B. Marsen, S. Krause, S. Pookpanratana, T. Unold, L. Weinhardt, C. Heske, and H. Schock, Appl. Phys. Lett. **99**, 112103 (2011).
19 T. Tanaka, T. Nagatomo, D. Kawasaki, M. Nishio, Q. Guo, A. Wakahara, A. Yoshida, and H. Ogawa, J. Phys. Chem. Solids **66**, 1978 (2005).
20 K. Jimbo, R. Kimura, T. Kamimura, S. Yamada, W. S. Maw, H. Araki, K. Oishi, and H. Katagiri, Thin Solid Films **515**, 5997 (2007).
21 H. Katagiri, K. Jimbo, M. Tahara, H. Araki, and K. Oishi, The Influence of the Composition Ratio on CZTS-Based Thin Film Solar Cells, (Cambridge Univ Press, 2009), pp. M04-01.
22 P. Fernandes, P. M. P. Salome, and A. F. da Cunha, Semicond. Sci. Technol. **24**, 105013 (2009).
23 N. Momose, M. T. Htay, T. Yudasaka, S. Igarashi, T. Seki, S. Iwano, Y. Hashimoto, and K. Ito, Jpn. J. Appl. Phys. **50**, 01BG09 (2011).
24 M. T. Htay, Y. Hashimoto, N. Momose, K. Sasaki, H. Ishiguchi, S. Igarashi, K. Sakurai, and K. Ito, Jpn. J. Appl. Phys. **50**, 032301 (2011).
25 C. Platzer-Björkman, J. Scragg, H. Flammersberger, T. Kubart, and M. Edoff, Sol. Energy Mater. Sol. Cells **98**, 110 (2012).
26 R. B. V. Chalapathy, G. S. Jung, and B. T. Ahn, Sol. Energy Mater. Sol. Cells **95**, 3216 (2011).
27 K. Moriya, K. Tanaka, and H. Uchiki, Jpn. J. Appl. Phys. **46**, 5780 (2007).
28 A. Moholkar, S. S. Shinde, A. R. Babar, K. Sim, H. K. Lee, K. Y. Rajpure, P. S. Patil, C. H. Bhosale, and J. H. Kim, J. Alloys Compounds **509**, 7439 (2011).
29 K. Ramasamy, M. A. Malik, and P. O'Brien, Chem. Sci. **2**, (2011).
30 T. Washio, T. Shinji, S. Tajima, T. Fukano, T. Motohiro, K. Jimbo, and H. Katagiri, J. Mater. Chem. **22**, 4021 (2012).
31 K. Tanaka, N. Moritake, and H. Uchiki, Solar Energy Mater. Solar Cells **91**, 1199 (2007).
32 K. Tanaka, M. Oonuki, N. Moritake, and H. Uchiki, Sol. Energy Mater. Sol. Cells **93**, 583 (2009).
33 K. Tanaka, Y. Fukui, N. Moritake, and H. Uchiki, Sol. Energy Mater. Sol. Cells **95**, 838 (2011).
34 K. Maeda, K. Tanaka, Y. Nakano, and H. Uchiki, Jpn. J. Appl. Phys. **50**, 05FB08 (2011).
35 K. Maeda, K. Tanaka, Y. Fukui, and H. Uchiki, Sol. Energy Mater. Sol. Cells **95**, 2855 (2011).
36 T. Todorov, M. Kita, J. Carda, and P. Escribano, Thin Solid Films **517**, 2541 (2009).
37 W. Ki, and H. W. Hillhouse, Adv. Energy Mater. **1**, 732 (2011).
38 T. Todorov, O. Gunawan, S. J. Chey, T. G. de Monsabert, A. Prabhakar, and D. B. Mitzi, Thin Solid Films **519**, 7378 (2011).
39 K. Woo, Y. Kim, and J. Moon, Energy Environ. Sci. **5**, 5340 (2012).
40 S. C. Riha, B. A. Parkinson, and A. L. Prieto, J. Am. Chem. Soc. **131**, 12054 (2009).
41 Q. Guo, H. W. Hillhouse, and R. Agrawal, J. Am. Chem. Soc. **131**, 11672 (2009).

42 C. Steinhagen, M. G. Panthani, V. Akhavan, B. Goodfellow, B. Koo, and B. A. Korgel, J. Am. Chem. Soc. **131**, 12554 (2009).
43 Q. Guo, G. M. Ford, W. Yang, B. C. Walker, E. A. Stach, H. W. Hillhouse, and R. Agrawal, J. Am. Chem. Soc. **132**, 17384 (2010).
44 L. Shi, C. Pei, Y. Xu, and Q. Li, J. Am. Chem. Soc. **133**, 10328 (2011).
45 X. Lu, Z. Zhuang, Q. Peng, and Y. Li, Chem. Commun. **47**, 3141 (2011).
46 A. Singh, H. Geaney, F. Laffir, and K. M. Ryan, J. Am. Chem. Soc. **134**, 2910 (2012).
47 P. Dai, X. Shen, Z. Lin, Z. Feng, H. Xu, and J. Zhan, Chem. Commun. **46**, 5749 (2010).
48 N. Nakayama, and K. Ito, Appl. Surf. Sci. **92**, 171 (1996).
49 J. Madarász, P. Bombicz, M. Okuya, and S. Kaneko, Solid State Ionics **141–142**, 439 (2001).
50 Y. B. K. Kumar, P. U. Bhaskar, G. S. Babu, and V. S. Raja, Phys. Status Solidi A **207**, 149 (2010).
51 T. Prabhakar, and N. Jampana, Sol. Energy Mater. Sol. Cells **95**, 1001 (2011).
52 V. G. Rajeshmon, C. S. Kartha, K. P. Vijayakumar, C. Sanjeeviraja, T. Abe, and Y. Kashiwaba, Solar Energy **85**, 249 (2011).
53 J. J. Scragg, P. J. Dale, L. M. Peter, G. Zoppi, and I. Forbes, Phys. Status Solidi (b) **245**, 1772 (2008).
54 J. J. Scragg, P. J. Dale, and L. M. Peter, Thin Solid Films **517**, 2481 (2009).
55 J. J. Scragg, D. M. Berg, and P. J. Dale, J. Electroanal. Chem. **646**, 52 (2010).
56 H. Araki, Y. Kubo, K. Jimbo, W. S. Maw, H. Katagiri, M. Yamazaki, K. Oishi, and A. Takeuchi, Phys. Status Solidi (c) **6**, 1266 (2009).
57 A. Ennaoui, M. Lux-Steiner, A. Weber, D. Abou-Ras, I. Kötschau, H. -. Schock, R. Schurr, A. Hölzing, S. Jost, R. Hock, T. Voß, J. Schulze, and A. Kirbs, Thin Solid Films **517**, 2511 (2009).
58 R. Schurr, A. Hölzing, S. Jost, R. Hock, T. Voβ, J. Schulze, A. Kirbs, A. Ennaoui, M. Lux-Steiner, A. Weber, I. Kötschau, and H. Schock, Thin Solid Films **517**, 2465 (2009).
59 S. M. Pawar, B. S. Pawar, A. V. Moholkar, D. S. Choi, J. H. Yun, J. H. Moon, S. S. Kolekar, and J. H. Kim, Electrochim. Acta **55**, 4057 (2010).
60 S. Ahmed, K. B. Reuter, O. Gunawan, L. Guo, L. T. Romankiw, and H. Deligianni, Adv. Energy Mater. **2**, 253 (2012).

Chapter 3

A General Synthesis Scheme for the Size Control and Quantum Confinement of Cu_2ZnSnS_4-type Nanocrystals.

Here, we present a generalized synthesis of quantum-confined colloidal copper zinc tin sulfide (Cu_2ZnSnS_4), copper tin sulfide (Cu_2SnS_3), and alloyed $(Cu_2SnS_3)_x(ZnS)_y$ nanocrystals (NCs) of varying sizes using thermal decomposition of copper, zinc, and tin diethyldithiocarbamate complexes. The NCs were characterized using X-ray diffraction, Raman spectroscopy, optical absorption, and energy dispersive spectroscopy. The optical absorption spectra of NCs with diameters less than 5 nm were found to shift towards higher energy due to quantum confinement.

3.1 Introduction

To be sustainable, future electronic materials must deliver desirable optoelectronic properties while containing only abundant and benign elements. While silicon can satisfy these requirements, it has well known limitations that necessitate the use of other materials in several important applications. Unfortunately, many of these other materials, such as GaAs or CdTe, have rare and toxic elements. The field of sustainable electronics (or *sustronics*) aims to develop new electronic materials that avoid these problems.

One example is Cu_2ZnSnS_4 (CZTS), which is emerging as a promising new sustainable semiconductor for solar cells. CZTS has a high absorption coefficient (~10^4 cm^{-1}) and an electronic bandgap (~1.5 eV)[1,2] that is nearly ideal for photovoltaics. Indeed, thin-film $Cu_2ZnSn(S,Se)_4$ solar cells were recently demonstrated with an overall power conversion efficiency > 10%.[3]

To improve upon this result, one potential strategy would be to develop nanostructured CZTS. For example, semiconductor NCs (or colloidal quantum dots)[4] have been proposed as a general route to high-efficiency, low-cost photovoltaic devices.[5,6] These materials are solution processible and, due to quantum confinement, exhibit optical properties that are tunable with NC size. In materials where the electronic levels can be changed through composition and quantum confinement, one can independently control both the effective band gap, and the location of the lowest unoccupied electronic level (e.g., electron affinity). Thus, multilayered devices containing films of quantum dots of different sizes could yield inexpensive multijunction solar cells.[7] Further, quantum dots can potentially allow the Shockley-Queisser power-conversion limit for Si (31%) to be exceeded through multiple exciton generation[8-10] or hot-electron extraction.[11] However, the best quantum-dot solar cells to date[10,12] have utilized lead chalcogenide NCs that do not satisfy sustainability goals. CZTS NCs could solve this problem while preserving the advantages of quantum dots.

Recently, several synthetic approaches to CZTS NCs have been reported.[13-16] However, two requirements for quantum-dot solar cells have yet to be demonstrated. First, no report has shown quantum confinement in CZTS NCs, which is critical for exploiting the advantages discussed above in solar cells. Second, the syntheses to date have not provided a range of NC sizes, which is necessary not only for fundamental studies but also for multijunction photovoltaic architectures.

Herein we resolve these two issues by demonstrating a simple synthesis that provides CZTS NCs with diameters ranging from 2 to 5 nm. This allows us to observe the effect of quantum confinement in the optical absorption spectra. In addition, we have generalized the synthesis to include Cu_2SnS_3 (CTS) and alloyed $(Cu_2SnS_3)_x(ZnS)_y$.

3.2 Experimental Section:

Materials: Copper (II) chloride dihydrate ($CuCl_2.2H_2O$, ACS grade, 99+%), tin (IV) chloride pentahydrate ($SnCl_4.5H_2O$, 98%), zinc chloride ($ZnCl_2$, reagent grade, 98%), sodium diethyldithiocarbamate trihydrate (Nadedc.$3H_2O$, ACS grade), oleylamine (OM, technical grade, 70%), dodecanethiol (DDT, ≥98%), oleic acid (OA, technical grade, 90%), 1-octadecene (ODE, technical grade, 90%), chloroform (HPLC grade, ≥99.8%), methanol (HPLC grade, ≥99.9%) and toluene (HPLC grade, 99.9%) were purchased from Sigma-Aldrich. Reagent alcohol (histological grade, 90% ethyl alcohol, 5% methyl alcohol, 5% butyl alcohol) was obtained from Fisher Scientific. All chemicals were used as delivered without further purification. Ultra-high purity water (18 MΩ) was obtained from a Millipore Direct-Q water purification system.

Synthesis of Copper Diethyldithiocarbamate [$Cu(dedc)_2$]: 9.0 g of sodium diethyldithiocarbamate was dissolved in 150 mL of reagent alcohol and added dropwise to a solution of 4.23 g of copper chloride in 50 mL reagent alcohol (85 mg/mL) with constant stirring. The black precipitate that formed upon reaction was filtered and washed multiple times with ultra-high purity water before drying in a desiccator. $Cu(dedc)_2$ crystals were purified by recrystallization from chloroform and dried overnight in vacuum before use. The crystals melted at 200 °C.

Synthesis of Zinc Diethyldithiocarbamate [$Zn(dedc)_2$)]: 9.0 g of sodium diethyldithiocarbamate was dissolved in 150 mL of reagent alcohol and added dropwise to a solution of 3.38 g of zinc chloride in 50 mL of reagent alcohol (68 mg/mL) with constant stirring. The white precipitate that formed upon reaction was filtered and washed multiple times with ultra-high purity water before drying in a desiccator. $Zn(dedc)_2$ crystals were purified by recrystallization from chloroform and dried overnight in vacuum before use. The crystals melted at 181 °C.

Synthesis of Tin Diethyldithiocarbamate [$Sn(dedc)_4$]: 12.85 g of sodium diethyldithiocarbamate was dissolved in 200 mL of reagent alcohol and added dropwise

to a solution of 2.5 g of tin tetrachloride in 50 mL of reagent alcohol (50 mg/mL) with constant stirring. The orange precipitate that formed upon reaction was filtered and washed multiple times with ultra-high purity water before drying in a desiccator. $Sn(dedc)_4$ crystals were purified by recrystallization from acetone and dried overnight in vacuum before use. The crystals melted at 170 °C.

Synthesis of CZTS NCs: The CZTS NCs were synthesized under dry nitrogen gas using a Schlenk line. In a typical synthesis, 36 mL of octadecene and 4 mL of oleic acid were mixed in a 100 mL three-neck flask. 54 mg of $Cu(dedc)_2$, 27.2 nm of $Zn(dedc)_2$, and 53.4 mg of $Sn(dedc)_4$ were then added to this mixture and the flask was connected to the Schlenk line and degassed multiple times at 60 °C. The crystals dissolved on stirring to give a brown solution. The contents of the flask were heated to 175°C and a specific volume of oleylamine was injected into the mixture. The NC size was tuned by changing the amount of oleylamine that was injected. For example, to synthesize NCs with an average diameter of 5 nm, 0.5 mL of oleylamine was injected into the flask to initiate nucleation. The NCs were then allowed to grow for 4 minutes before quenching the reaction by immersing the flask in water. For the synthesis of 2.5, 3.5, and 4 nm diameter NCs, 4, 2 and 1 ml OM was injected, respectively.

The NCs were precipitated from the dispersion using reagent alcohol and were centrifuged for 5 minutes at 4000 rpm. The supernatant was discarded and the NCs were redispersed in toluene. The precipitation and dispersion steps were repeated multiple times to remove excess oleylamine and oleic acid. Finally, the NCs were dispersed in toluene and stored for later use.

Synthesis of 2 nm CZTS NCs: In a typical synthesis, 54 mg of $Cu(dedc)_2$, 27.2 nm of $Zn(dedc)_2$, and 53.4 mg of $Sn(dedc)_4$ were added to a 25 mL 3 neck flask containing 6 ml dodecanethiol. The flask was then connected to the Schlenk line and degassed multiple times at 60 °C. At 150°C, 1 ml OM was injected into the flask and its contents heated to 175°C. The NCs were then allowed to grow for 4 minutes before quenching the reaction

by immersing the flask in water. The NCs were cleaned the same manner as for the 5 nm CZTS NCs.

Synthesis of Cu_2SnS_3 (CTS) NCs: CTS NCs were synthesized in a manner similar to CZTS except for using only $Cu(dedc)_2$ (54 mg) and $Sn(dedc)_4$ (53.4 mg) with no Zn. Injecting 1.25, 2, and 4 ml OM gave NCs of diameter 3.5, 3, and 2 nm, respectively.

Synthesis of alloyed $(Cu_2SnS_3)_x(ZnS)_y$ NCs: $Cu(dedc)_2$, $Zn(dedc)_2$, and $Sn(dedc)_4$ were added to a 100 ml three neck flask containing 36 mL of octadecene and 4 mL of oleic acid with the weights chosen according to the ratio x:y. For example, when x:y=1:3, 35.9 mg $Cu(dedc)_2$, 54.4 mg $Zn(dedc)_2$, and 35.25 mg $Sn(dedc)_4$ were used. All the other procedures for the synthesis and cleaning of the NCs remain the same as in the case of stoichiometric CZTS. 4 ml OM was added to get quantum confined NCs.

Characterization Techniques: X-ray diffraction (XRD) patterns for the NCs were collected and recorded using a Bruker-AXS microdiffractometer equipped with a Cu-K_α X-ray source. The NCs were examined and imaged using an FEI Tecnai G^2 F30 transmission electron microscope (TEM) with an acceleration potential of 300 kV. Optical absorbance spectra from NCs dispersed in toluene was measured using a Cary 5 spectrophotometer. Pure toluene was to obtain the background spectrum. Energy dispersive spectroscopy (EDX) measurements used for the elemental analysis of the deposited films were carried out on a JEOL 6700 FESEM equipped with an energy dispersive spectrophotometer (Thermo-Noran Vantage SIX). The accelerating voltage was kept constant as 15 keV. The spatial- and thickness-averaged elemental concentrations were determined using the phi-rho-z method with theoretical standard element sensitivity factors after subtracting the background from the acquired X-ray spectra. Raman measurements were carried out using a Witec confocal Raman microscope. The samples were excited using an Argon laser at 514.5 nm. The Raman scattering signal was analyzed using a monochromator with a grating of 1800 lines/mm. Raman scattering was collected from thin films of NCs that were cast on molybdenum-coated glass substrates from a dilute dispersion in toluene. Fourier transform infrared

(FTIR) absorption spectra were collected using a Nicolet Magna 550 series II FTIR spectrophotometer with an attenuated total reflection (ATR) accessory (Harrick Scientific) and a Glowbar source. The infrared beam was focused normal onto the 45° beveled edge of the trapezoidal Ge ATR crystal ($5 \times 1 \times 0.1$ cm^3). Aliquots of colloidal CZTS suspensions were cast onto the Ge ATR crystal and allowed to dry before recording their FTIR spectrum. Thermal analysis was carried out with a Pyris /Diamond TG-DTA 6300 (produced from Perkin-Elmer) analyzer with ~20 mg of sample heated at a rate of 10°C/min.

3.3 Results and Discussion

CZTS NCs were synthesized using copper, zinc, and tin diethyldithiocarbamates, which can individually decompose thermally to produce their corresponding sulphides (e.g., CuS, ZnS, and SnS_2).[17] In principle, CZTS NCs can be obtained when stoichiometric mixtures of these three complexes are heated together. However, since the decomposition temperatures of copper, zinc, and tin diethyldithiocarbamates are 220 °C, 240 °C, and 175 °C, respectively (Figure 3.1), decomposition of the precursors at different temperatures can result in unwanted phases such as ZnS, SnS_2, and CuS. To avoid this, we utilized the addition of oleylamine, which can lower the decomposition temperature of all three complexes to a narrow temperature range.[18] The mechanism of oleylamine promoted thermal decomposition of metal alkyldithiocarbamate complexes was investigated by Jung *et al.* who hypothesized that oleylamine coordinates with the thiocarbonyl carbon of the dithiocarbamate ligand and accelerates decomposition.[18] Thus, simultaneous decomposition of the copper, zinc, and tin dithiocarbamate complexes can be triggered by the sudden injection of oleylamine into a mixture of the three complexes. The amine is added when the mixture temperature is below that needed for the decomposition of the individual complexes, but above that needed for the decomposition of the complexes in the presence of the amine.

When the appropriate stoichiometric mixture of the precursors are used in the reaction solution (i.e., 2:1:1 for copper, zinc, and tin diethyldithiocarbamates, respectively), this approach leads to nucleation and subsequent growth of CZTS NCs. The concentration of the nuclei available for growth is determined by the amount of oleylamine injected. By varying the amount of oleylamine injected into the solution, we were able to tune the average diameter of the NCs. Specifically, the final NC size decreased when the volume of oleylamine injected into the solution was increased. The growth time of the NCs did not influence their final size. Attenuated-total-reflection Fourier transform infrared spectra of the NCs showed that the NCs are capped both with oleylamine and oleic acid ligands (Figure 3.2).

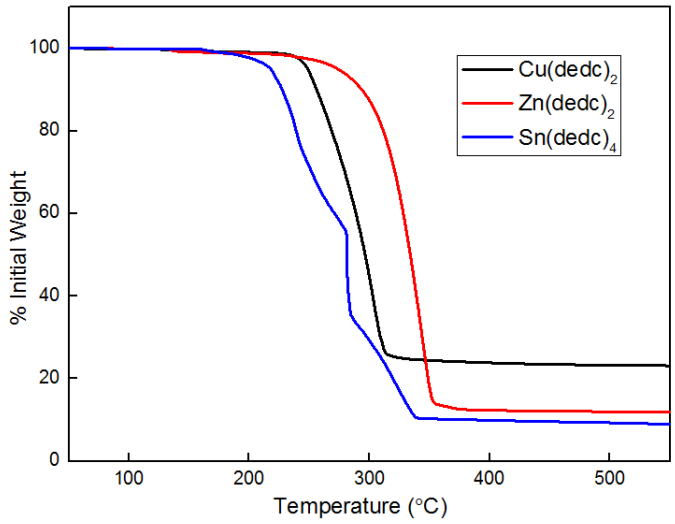

Figure 3.1 Weight of metal diethyldithiocarbamate complexes remaining as a function of temperature determined through thermogravimetric analysis using a Perkin Elmer Pyris Diamond TG/DTA 6300.

Figure 3.3 shows high resolution transmission electron micrographs (HRTEM) of individual CZTS NCs. By changing the volume of oleylamine, NCs of average sizes 5, 4, 3.5, 2.5, and 2 nm were obtained. The HRTEM images confirm that the quantum dots are crystalline and exhibit lattice spacings that are consistent with CZTS.

To confirm that the NCs are CZTS, we employed several additional characterization methods to confirm their stoichiometry and structure. First, we used energy dispersive spectroscopy (EDX) to determine the elemental composition of the NC ensembles. Table 3.1 shows the results of the EDX analysis. All four elements are present, and the Zn:Cu and Sn:Cu atomic ratios are approximately 1:2 as expected. The NCs are also slightly rich in sulphur.

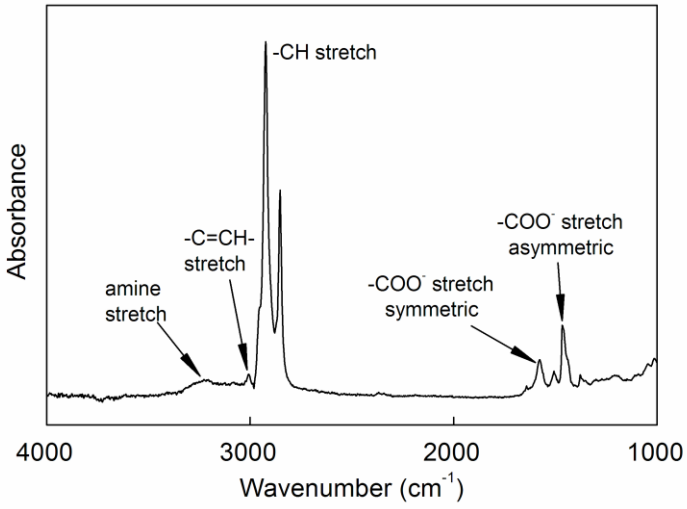

Figure 3.2 ATR-FTIR spectra from CZTS NCs. The FTIR data suggests that both oleylamine and oleic acid act as capping ligands for the NCs.

Second, we collected X-ray diffraction (XRD) from NCs drop-casted onto silicon as a function of NC size. CZTS crystallizes in a tetragonal crystal structure with c≈2a. CZTS crystal structure is similar to two zinc blende lattices stacked on top of each other with Cu, Zn, and Sn occupying half of the tetrahedral voids within the sulfur face centered lattice (Figure 3.4a).[19] Cu_2SnS_3 (CTS) and ZnS result when the occupied half of the tetrahedral voids is filled with Cu and Sn, and Zn, respectively (Figure 3.4b,c).[21,22] Consequently, CZTS, CTS, and ZnS have nearly identical XRD patterns as shown in Figure 3.5. The XRD patterns in Figure 3.5 were simulated using Crystal Diffract®. The XRD simulations were performed using lattice parameters and Wyckoff site positions of the atoms taken from Refs. 20, 21, and 22 for CZTS, CTS, and ZnS, respectively. The

similarities in the three XRD patterns are not only due to the similarities between the three structures but also due to the proximity of the Zn and Cu in the periodic table with atomic masses 65.4 and 63.6, respectively. The presence of the (110) and (121) XRD peaks have been used for distinguishing CZTS from ZnS in the bulk.[23] These peaks, however, become indistinguishable from the background due to broadening of the diffraction peaks for NCs smaller than 5 nm. Based on the XRD alone, one can only determine that either one or a mixture of CZTS, CTS, and ZnS are present. XRD patterns of CZTS NCs synthesized using the method described above are shown in Figure 3.6. The crystallite sizes extracted from the width of the (112) diffraction peak at 28.5° using the Debye-Scherrer equation range from 2 to 5 nm, in agreement with the HRTEM images. The observed diffraction peaks also match those expected for CZTS (JCPDS 01-075-4122).

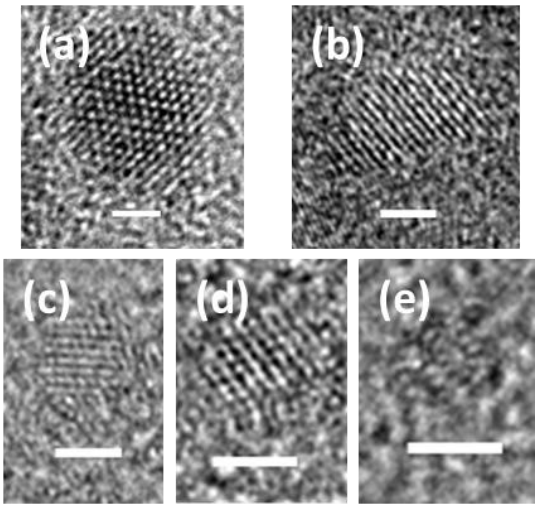

Figure 3.3 HRTEM images of synthesized CZTS NCs with diameters of: (a) 5 nm, (b) 4 nm, (c) 3.5 nm, (d) 2.5 nm, and (e) 2nm. The NCs are single crystalline. All scale bars are 2 nm.

To distinguish CZTS from CTS and ZnS, we use Raman scattering. Figure 3.7 shows Raman scattering data from NC films cast onto Mo-coated glass substrates from colloidal dispersions. Raman scattering data for five different NC sizes are shown. In

each case, only a single Raman peak at 337 cm^{-1} is detected. The location of this peak matches that expected from bulk CZTS (338 cm^{-1}).[24] Raman peaks for Cu_xS, ZnS, and SnS_2 are expected at 472 cm^{-1}, 351 cm^{-1}, and 315 cm^{-1}, respectively.[24] The linewidths in Figure 3.7 are larger than those typically observed in bulk CZTS. Broadening of Raman peaks has been observed previously for NCs of other materials and attributed to phonon confinement within the NCs.[25] In principle, this could mask the presence of Raman peaks due to ZnS and SnS_2. However, when we anneal films of our NCs, a single sharp peak at 338 cm^{-1} is observed with no detectable Raman scattering at the frequencies expected for ZnS or SnS_2 (Figure 3.8). Thus, we conclude that our NCs are CZTS and other sulfide phases are not present, at least within the detection limit of Raman scattering.

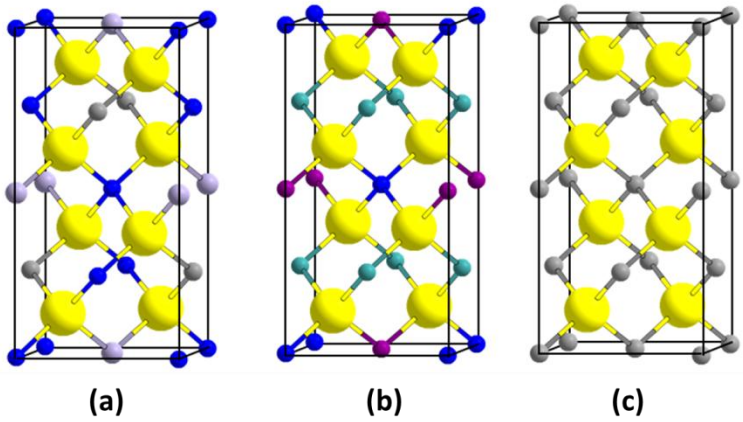

Figure 3.4 Schematic representation of (a) CZTS, (b) CTS, and (c) ZnS structures.

After confirming that the NCs were CZTS, we proceeded to examine their optical properties. As stated above, effects due to quantum confinement have not yet been observed for CZTS NCs. In general, the optical transitions of a bulk semiconductor should shift to higher energy if the optically excited electron hole pair is confined within the NC boundary.[26,27] Figure 3.9 shows the absorption spectra from our NCs as a function of size. The inset to Figure 3.9 shows a Tauc plot for the corresponding absorbance

curves. The bandgap of CZTS NCs increases progressively from 1.5 to 1.85 eV as the NC diameter reduces from 5 to 2 nm. There was no photoluminescence from the NCs. Using the values of dielectric constant and effective masses from Ref. 28, we estimate the exciton Bohr radius, a_{exc}, for CZTS NCs to be between 2.5-3.3 nm.[27] Thus, we expect the NCs with diameters less than ~5 nm to begin exhibiting quantum confinement effects consistent with our experimental observations.

The NC synthesis described above is general and may be extended to synthesize other NCs related to CZTS. We extended this synthetic approach to make CTS as well as alloyed $(Cu_2SnS_3)_x(ZnS)_y$ NCs. CTS can be synthesized by using only Cu and Sn diethyldithiocarbamates in the ratio 2:1 and the method to vary the NC size is similar to that used for controlling the NC sizes during the synthesis of CZTS NCs. Figure 3.10 shows the HRTEM of 2-3.5 nm diameter CTS NCs synthesized using this approach. Elemental analysis using EDX (Table 3.1) reveals that the Sn:Cu ratio is approximately 1:2 as expected. The CTS samples are also sulfur rich, similar to CZTS.

Figure 3.11 shows the XRD from CTS NCs as a function of size. The crystallite sizes extracted from the width of the $(\bar{2}\,\bar{3}\,1)$ diffraction peak at 28.4° using the Debye-Scherrer equation range from 2 to 3.5 nm, in agreement with the HRTEM images. The observed diffraction peaks also match those expected for CTS (JCPDS 00-027-0198). The Raman scattering peaks for all the CTS NCs is ~337 cm^{-1} (Figure 3.12). This is very close to the Raman scattering peak for tetragonal Cu_2SnS_3 (space group $I\bar{4}2m$) at 336 cm^{-1}.[29] Cubic Cu_2SnS_3 (space group $F\bar{4}3m$) has its most intense Raman scattering peak at 303 cm^{-1}.[29] Given the broadening of the Raman scattering peaks and within the detection limit of Raman scattering, the synthesized NCs appear to be tetragonal Cu_2SnS_3 with no other binary phases.

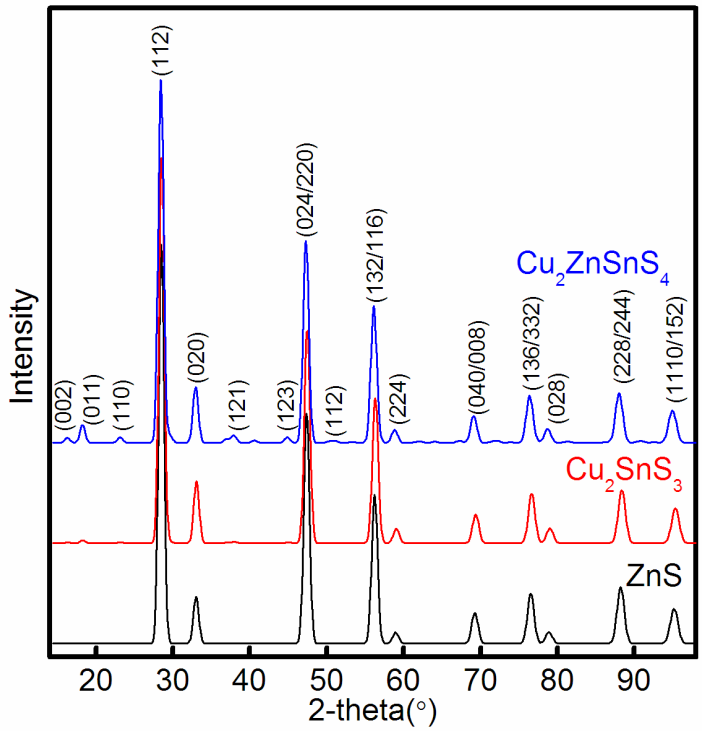

Figure 3.5 Simulation of XRD patterns for CZTS, CTS, and ZnS.

Figure 3.13 shows the optical absorption spectra of CTS NCs as a function of size. CTS NCs show a large absorption peak in the IR region of the electromagnetic spectrum which we attribute to plasmon absorption similar to that recently observed in Cu_2S NCs.[30] CZTS NCs do not show a plasmonic absorption peak. This absorption in the IR for Cu_2S has been attributed to local surface plasmon resonances and arises due to p-type carriers in vacancy doped NCs.[30] The plasmonic absorption peak interferes with extraction of a band gap from the CTS absorption spectra because the rising edge of the absorption spectra was covered by the plasmonic absorption peak.

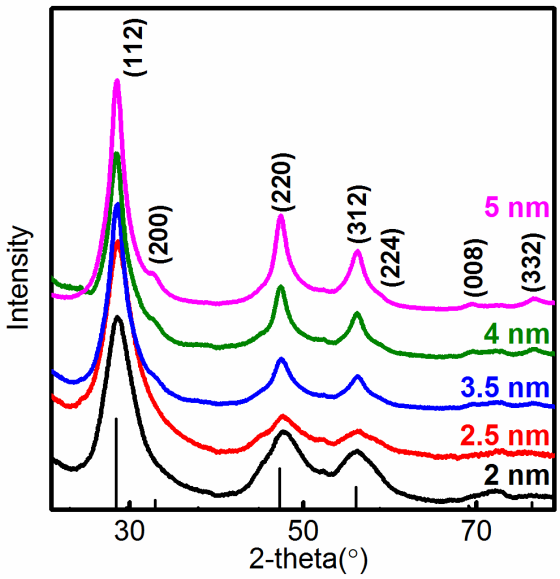

Figure 3.6 XRD from CZTS NCs (Cu Kα radiation). The stick reference powder XRD pattern is that for the CZTS Kesterite structure (JCPDS 01-075-4122). The average particle diameters determined from a Scherrer analysis of the width of the (112) diffraction peak are indicated next to each pattern.

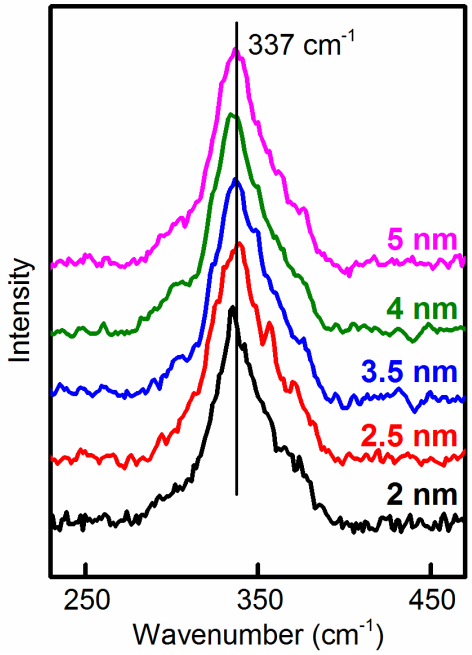

Figure 3.7 Room temperature Raman spectra for our CZTS NCs as a function of their average diameter. Bulk CZTS exhibits a peak at 338 cm^{-1}.

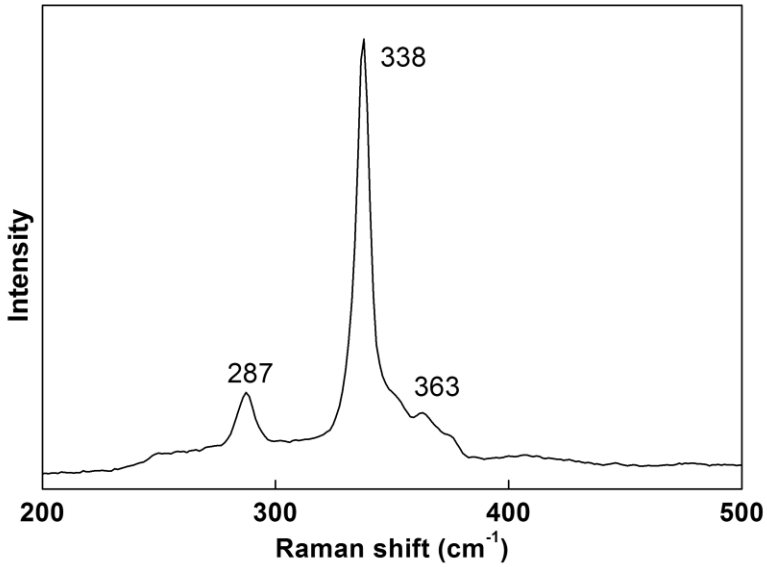

Figure 3.8 Raman spectra from thin films of CZTS NCs annealed at 550 °C. The Raman peaks match those for bulk CZTS.

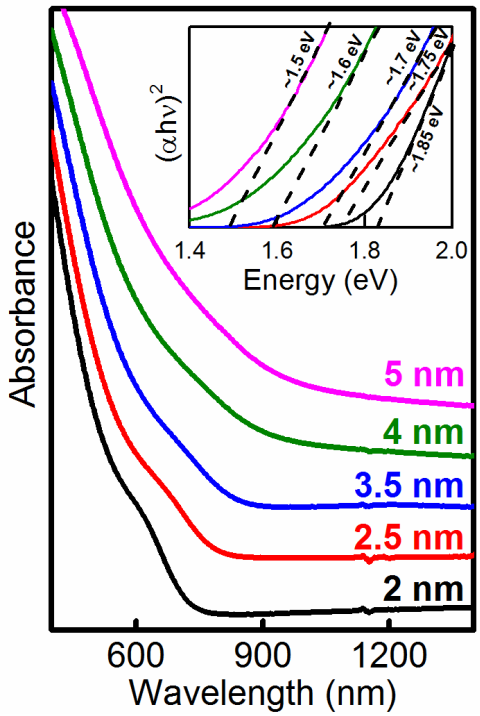

Figure 3.9 Room temperature optical absorption spectra for our CZTS NCs as a function of their average diameter. Inset shows the Tauc plot for the corresponding absorbance curves.

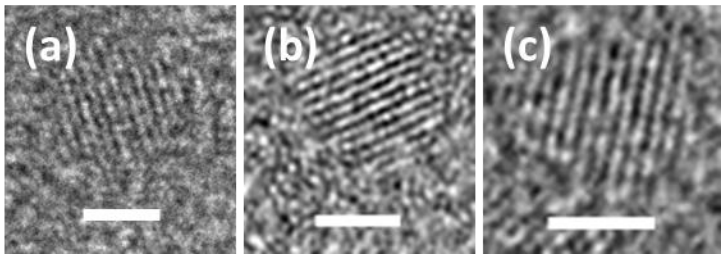

Figure 3.10 HRTEM images of synthesized CTS NCs with diameters of: (a) 3.5 nm, (b) 3 nm, and (c) 2 nm. The NCs are single crystalline. All scale bars are 2 nm.

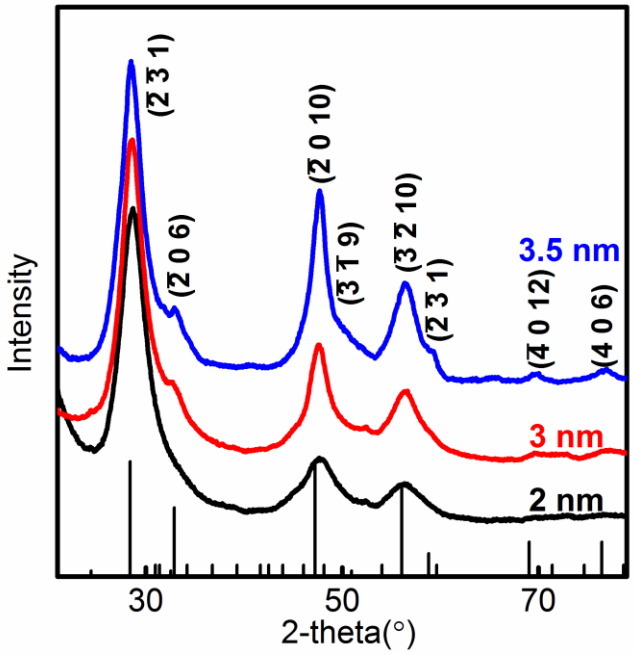

Figure 3.11 XRD from CTS NCs (Cu Kα radiation). The stick reference powder XRD pattern is that for the Cu_2SnS_3 structure (JCPDS 00-027-0198). The average particle diameters determined from a Scherrer analysis of the width of the (-2-31) diffraction peak are indicated next to each pattern.

CZTS can be viewed as a 1:1 alloy of CTS and ZnS. By changing the CTS:ZnS ratio, the band gap of the resulting alloy can be tuned from 1.35 eV (for tetragonal CTS) to 3.63 eV (for ZnS).[16] In order to generalize the CZTS synthesis, we also synthesized alloyed $(Cu_2SnS_3)_x(ZnS)_y$ NCs by varying the ratio of Cu_2SnS_3:ZnS. In particular, we chose four specific ratios of 1:6, 1:3, 3:1, and 6:1 for this study. These correspond to

$Cu_{0.89}Zn_{2.67}Sn_{0.44}S_4$ NCs, $Cu_{1.33}Zn_2Sn_{0.66}S_4$ NCs, $Cu_{2.40}Zn_{0.40}Sn_{1.2}S_4$ NCs, and $Cu_{2.53}Zn_{0.21}Sn_{1.26}S_4$ NCs, respectively. For this synthesis, we injected 4ml oleylamine into the reaction flask to accelerate nucleation and form small NCs. All the results for alloyed NCs have been plotted along with the data for stoichiometric quantum-confined CZTS NCs synthesized with 4 ml OM. Figure 3.14 shows that the alloyed NCs have sizes similar to stoichiometric CZTS. Sn:Cu and Zn:Cu atomic ratios were found to be very close to the ratios of the metal dithiocarbamate precursors (Table 3.1) charged into the reaction solution, confirming the robust and facile control of NC stoichiometry that can be achieved using this synthesis technique. The alloyed NCs were also found to be sulphur rich similar to the stoichiometric CZTS NCs.

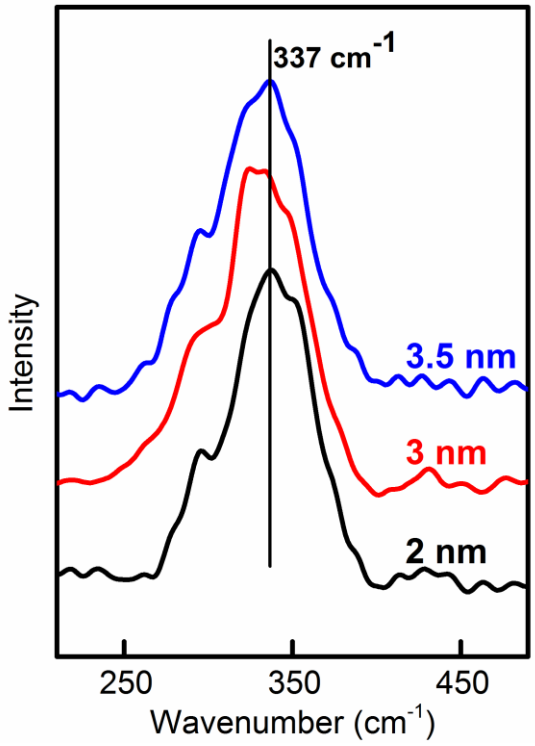

Figure 3.12 Room temperature Raman spectra for the CTS NCs as a function of their average diameter. Bulk CTS exhibits a peak at 336 cm^{-1}. The CTS Raman spectra have been averaged with a 4-point FFT filter to reduce the noise in the scattering data.

Figure 3.15 shows the XRD from the alloyed NCs as a function of their stoichiometry. The crystallite sizes extracted from the width of the (112) diffraction peak at 28.5° using the Debye-Scherrer equation (2.5-3 nm) are in agreement with HRTEM images. The observed diffraction peaks also match those expected for CZTS (JCPDS 01-075-4122). The Raman scattering peak for the alloyed NCs is at ~339 cm^{-1} (Figure 3.16), which is very close to that observed from stoichiometric CZTS. Drawing from our analysis of stoichiometric CZTS, we conclude that the alloyed NCs are also phase pure and other binary sulfide phases such as Cu_xS or SnS are not present, at least within the detection limit of Raman scattering.

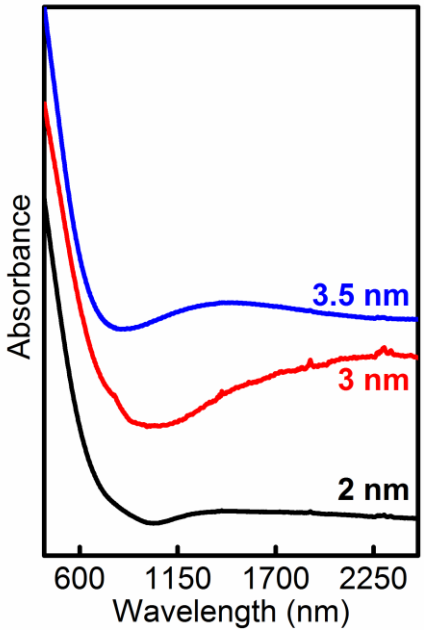

Figure 3.13 Room temperature optical absorption spectra for our CTS NCs as a function of their average diameter. The local plasmon absorption peak in the IR decreases with diameter of the NCs.

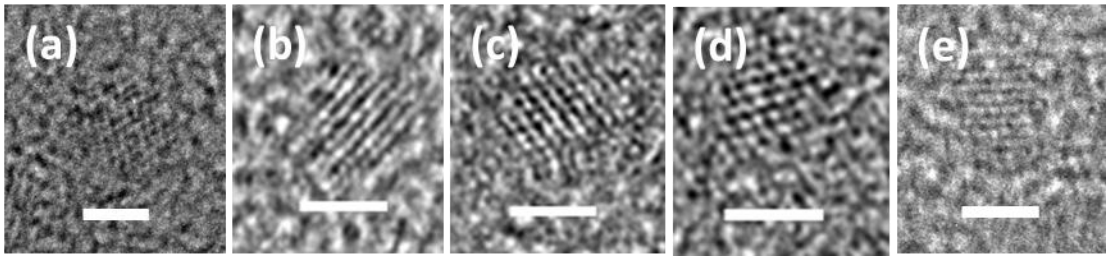

Figure 3.14 HRTEM images of synthesized alloyed NCs with Cu_2SnS_3:ZnS ratio of: (a) 1:6, (b) 1:3, (c) 1:1, (d) 3:1, and (e) 6:1. The NCs are single crystalline. All scale bars are 2 nm.

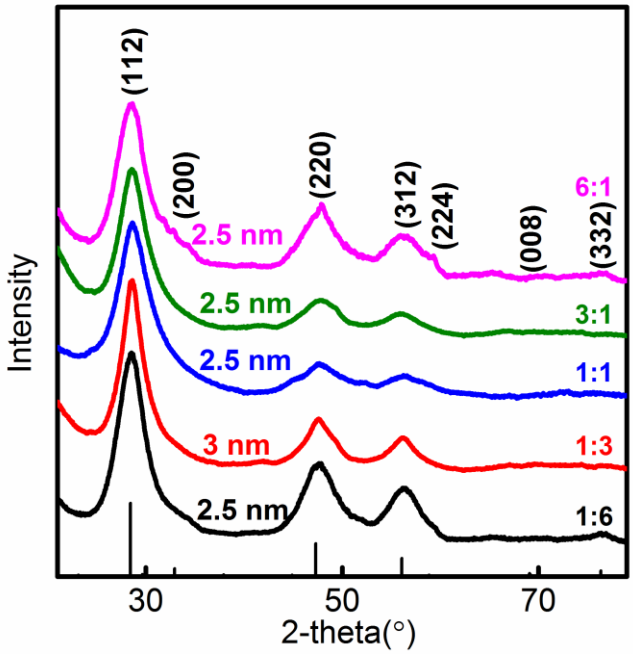

Figure 3.15 XRD patterns from alloyed NCs (Cu Kα radiation) as a function of Cu_2SnS_3:ZnS ratio. The stick reference powder XRD pattern is that for the CZTS Kesterite structure (JCPDS 01-075-4122). The average particle diameters determined from a Scherrer analysis of the width of the (112) diffraction peak are indicated next to each pattern.

After confirming the structure and phase purity of the alloyed NCs, we proceeded to examine their optical properties. Figure 3.17 shows the absorption spectra from the alloyed NCs as a function of stoichiometry. The bandgap of alloyed NCs increases when the Cu_2SnS_3: ZnS ratio decreases from 6:1 to 1:6. ZnS has a bandgap of 3.6 eV, whereas

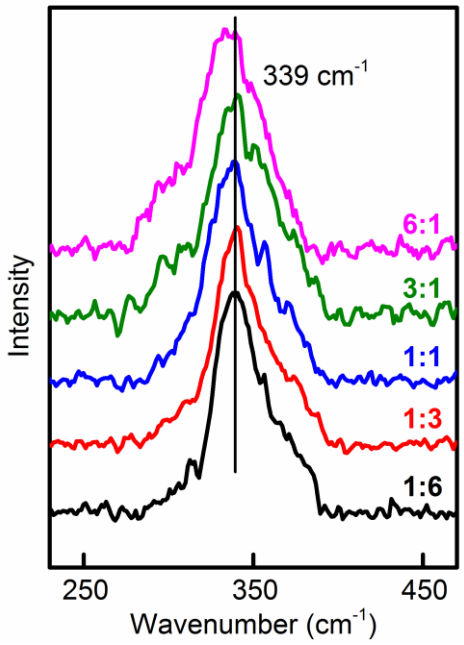

Figure 3.16 Room temperature Raman spectra for alloyed NCs as a function of Cu_2SnS_3:ZnS ratio. Bulk CZTS exhibits a peak at 338 cm^{-1}.

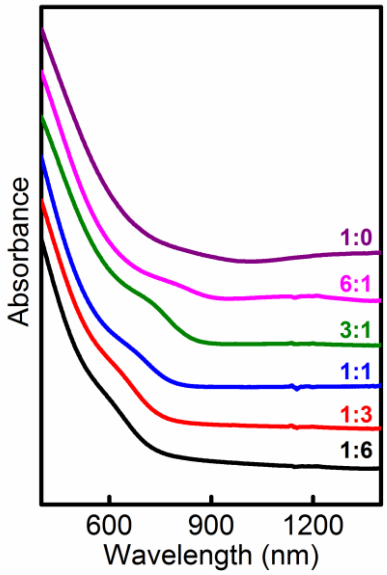

Figure 3.17 Room temperature optical absorption spectra for alloyed NCs as a function of Cu_2SnS_3:ZnS ratio. These NCs are of diameter 2.5-3 nm.

Table 3.1 Elemental composition of the CZTS, CTS, and alloyed NCs from EDX as a function of the average NC diameter. Elemental composition for the alloyed NCs has been reported as a function of Cu_2SnS_3:ZnS ratio. The elemental composition is reported with respect to the amount of copper within the sample.

Sample	Diameter	Zn/Cu	Sn/Cu	S/Cu
Ideal CZTS		0.50	0.50	2.00
CZTS NC	**5nm**	0.50	0.57	2.33
CZTS NC	**4nm**	0.50	0.56	2.40
CZTS NC	**3.5nm**	0.50	0.54	2.38
CZTS NC	**2.5nm**	0.49	0.56	2.32
CZTS NC	**2nm**	0.49	0.59	2.53
Ideal CTS		0.00	0.50	1.50
CTS NC	**3.5nm**	0.00	0.54	1.80
CTS NC	**3nm**	0.00	0.51	1.60
CTS NC	**2nm**	0.00	0.54	1.74
Alloyed NCs				
Ideal 1:3		1.50	0.50	3.00
1:3 NC	**3 nm**	1.36	0.58	3.85
Ideal 3:1		0.17	0.50	1.67
3:1 NC	**2.5 nm**	0.18	0.58	2.33
Ideal 1:6		3.00	0.50	4.50
1:6 NC	**2.5 nm**	2.63	0.56	5.17
Ideal 6:1		0.08	0.50	1.58
6:1 NC	**2.5 nm**	0.06	0.54	2.01

the bandgap for tetragonal Cu_2SnS_3 has been reported to be 1.35 eV.[29] Thus, for similar diameter NCs, those with stoichiometry 1:3 (more ZnS as compared to stoichiometric CZTS) will have a larger bandgap than stoichiometric CZTS and vice versa. The rising edge of the optical absorption curve shifts towards higher wavelength (lower energy) on changing the alloy stoichiometry from 1:6 to 6:1, with the CTS NCs having the minimum in its absorption spectrum further lower in energy than the 6:1 alloy. This trend matches well with the decrease in the theoretical band gap on increasing the CTS content within

the alloy. CZTS NCs of diameter 2.5 nm are quantum-confined and exhibit a band gap of 1.75 eV. In addition, the absorption spectra of 2.5 nm CZTS exhibits an absorption hump ~650 nm as a signature of the electronic transitions between 1Se-1Sh levels.[4] The alloyed NCs also exhibit an absorption hump similar to the quantum-confined stoichiometric CZTS NCs. The absorption humps also shift to lower energies on changing the alloy composition from 1:6 to 6:1, as expected from their stoichiometry. The presence of an absorption hump in the absorption spectra of the alloyed NCs confirms that the alloyed NCs are quantum-confined.

3.4 Summary

In summary, we report a general synthesis of CZTS NCs from thermally decomposable diethyldithiocarbamate complexes where the average NC diameter could be changed controllably between 2 and 5 nm. Characterization using HRTEM, XRD, and Raman spectroscopy confirm the phase purity of the CZTS NCs. NCs of diameters < 5nm exhibit shifts in their optical transitions which are consistent with quantum confinement. By changing the ratio of the initial metal precursors, we were able to synthesize quantum-confined alloyed $(Cu_2SnS_3)_x(ZnS)_y$ NCs along with CTS NCs. The general synthesis of quantum confined CZTS NCs presented here can be used for synthesis of CZTS quantum dots with varying band gaps and electron affinities by changing the NC diameter and stoichiometry, thus making it possible to use these NCs for fabricating multi-junction CZTS quantum dot solar cell.

3.5 References

1 H. Katagiri, Thin Solid Films **480-481**, 426 (2005).
2 D. B. Mitzi, O. Gunawan, T. K. Todorov, K. Wang, and S. Guha, Sol. Energy Mater. Sol. Cells **95**, 1421 (2011).

3 D. A. R. Barkhouse, O. Gunawan, T. Gokmen, T. K. Todorov, and D. B. Mitzi, Prog. Photovolt: Res. Appl. **20**, 6 (2012).
4 V. I. Klimov, Nanocrystal Quantum Dots, (CRC Press, 2009).
5 W. U. Huynh, J. J. Dittmer, and A. P. Alivisatos, Science **295**, 2425 (2002).
6 A. Kongkanand, K. Tvrdy, K. Takechi, M. Kuno, and P. V. Kamat, J. Am. Chem. Soc. **130**, 4007 (2008).
7 T. Franzl, T. A. Klar, S. Schietinger, A. L. Rogach, and J. Feldmann, Nano Lett. **4**, 1599 (2004).
8 A. Nozik, Physica E **14**, 115 (2002).
9 J. B. Sambur, T. Novet, and B. A. Parkinson, Science **330**, 63 (2010).
10 O. E. Semonin, J. M. Luther, S. Choi, H. Chen, J. Gao, A. J. Nozik, and M. C. Beard, Science **334**, 1530 (2011).
11 W. A. Tisdale, K. J. Williams, B. A. Timp, D. J. Norris, E. S. Aydil, and X. Y. Zhu, Science **328**, 1543 (2010).
12 A. Pattantyus-Abraham, I. J. Kramer, A. R. Barkhouse, X. Wang, G. Konstantatos, R. Debnath, L. Levina, I. Raabe, M. K. Nazeeruddin, M. Grätzel, and E. H. Sargent, ACS Nano **4**, 3374 (2010).
13 Q. Guo, H. W. Hillhouse, and R. Agrawal, J. Am. Chem. Soc. **131**, 11672 (2009).
14 C. Steinhagen, M. G. Panthani, V. Akhavan, B. Goodfellow, B. Koo, and B. A. Korgel, J. Am. Chem. Soc. **131**, 12554 (2009).
15 S. C. Riha, B. A. Parkinson, and A. L. Prieto, J. Am. Chem. Soc. **131**, 12054 (2009).
16 Q. Liu, Z. Zhao, Y. Lin, P. Guo, S. Li, D. Pan, and X. Ji, Chem. Commun. **47**, 964 (2011).
17 D. Pan, X. Wang, H. Zhou, W. Chen, C. Xu, and Y. Lu, Chem. Mater. **21**, 2489 (2009).
18 Y. K. Jung, J. I. Kim, and J. K. Lee, J. Am. Chem. Soc. **132**, 178 (2010).
19 S. Chen, X. G. Gong, A. Walsh, and S. Wei, Appl. Phys. Lett. **94**, 041903 (2009).
20 S. R. Hall, J. T. Szymanski, and J. M. Stewart, Can. Mineral. **16**, 131 (1978).
21 X. Chen, H. Wada, A. Sato, and M. Mieno, J. Solid State Chem. **139**, 144 (1998).
22 R. W. G. Wyckoff, Crystal Structures, (Wiley, New York, 1963), pp. 110.
23 A. J. Cheng, M. Manno, A. Khare, C. Leighton, S. A. Campbell, and E. S. Aydil, J. Vac. Sci. Technol. A **29**, 051203 (2011).
24 P. A. Fernandes, P. M. P. Salome, and A. F. da Cunha, Thin Solid Films **517**, 2519 (2009).
25 D. Bersani, P. P. Lottici, and X. Z. Ding, Appl. Phys. Lett. **72**, 73 (1998).
26 L. E. Brus, J. Chem. Phys. **80**, 4403 (1984).
27 A. L. Efros, and A. L. Efros, Sov. Phys. Semicond. **16**, 772 (1982).
28 C. Persson, J. Appl. Phys. **107**, 053710 (2010).
29 P. A. Fernandes, P. M. P. Salomé, and A. F. d. Cunha, J. Phys. D **43**, 215403 (2010).
30 J. M. Luther, P. K. Jain, T. Ewers, and A. P. Alivisatos, Nat. Mater. **10**, 361 (2011).

Chapter 4
Thin Film Deposition From Colloidal Dispersions of CZTS Nanocrystals

In this chapter, I will discuss the process of depositing thin films from CZTS nanocrystals (NCs) using drop casting and doctor blading. By varying the concentration of the NC dispersion, we could deposit continuous films from NC dispersions with crack widths no larger than ~100 nm. Annealing NC films at temperatures ranging from 275-600 °C in air-free atmospheres led to grain growth and compaction of films. NCs begin to show intense grain growth at temperatures much below the melting point. However, NC films crack when they are annealed because the starting films have high porosity and internal stresses that build up during drying. Our results suggest that larger diameter NCs should be used for reducing both the film porosity and the internal stresses which in turn may lead to the formation of dense, crack free CZTS thin films.

4.1 Introduction

Thin film deposition from colloidal NC dispersions is being explored as an alternative to vacuum-based deposition techniques such as sputtering and evaporation.[1] Thin films can be deposited uniformly and rapidly on large scale from colloidal NC dispersions using roll-to-roll coating methods. On smaller (*e.g.*, 1”×1”) scale, spin coating, dip coating, drop casting, and doctor blading may be used and these are the methods typically used for laboratory-scale solar cell research. Amongst these methods, spin coating wastes more than 90% of the initial solution during deposition. In addition, spin coating is difficult to scale up for large scale industrial applications. Layer-by-layer dip coating, although highly successful for fabricating thin films for quantum dot solar cells,[2,3] is suitable only for depositing several hundred nanometer thick films. In layer-by-

layer dip coating, the substrate is dipped into the colloidal solution multiple times (*e.g.*, 2-20) and dried. Sometimes dipping is combined with a second step to remove or replace the ligands on the NC surfaces to immobilize the NCs already deposited onto the substrate surface. Each dipping cycle deposits only a few monolayers of NCs. Consequently, it may take hundreds of dipping cycles to deposit 1-2 μm thick films (typical thickness of a CZTS absorber layer) from 5 nm diameter NCs. Thus, layer-by-layer dip coating is not suitable for industrial production. It is tedious and slow for laboratory research.

Drop casting from NC dispersions has been used in the past for depositing NC thin films.[1] Although drop casting from NC dispersions cannot be scaled up for industrial production, unlike spin coating, it does not waste NCs and yields reasonable thickness films much faster than layer-by-layer dip coating. Doctor blading is a technique very similar to slot coating and is one of the techniques frequently used for commercial thin film production. In this chapter, we chose to deposit thin films from CZTS NC dispersions using drop casting and doctor blading to test the viability of these approaches to depositing NC thin films from ~5 nm diameter CZTS NCs.

4.2 Experimental Section

Thin Films Using Drop Casting: All the films were cast from 5 nm diameter CZTS NCs which were synthesized as described in Chapter 3. Post synthesis, the NCs were cleaned twice, as described previously, and dispersed in toluene. Typical concentrations were 6 mg/ml (0.13% volume solids in solution). The concentration of the NC dispersion was adjusted by changing the total toluene volume used to disperse a fixed weight of CZTS NCs. The NC weight was determined by assuming the synthesis yield to be ~90%. Mo-coated fused silica substrates were used for thin film deposition. Metallic rectangular masks (250 μm thick, 0.75”×0.75”, Figure 4.1) were used for depositing thin films from colloidal NC dispersions.

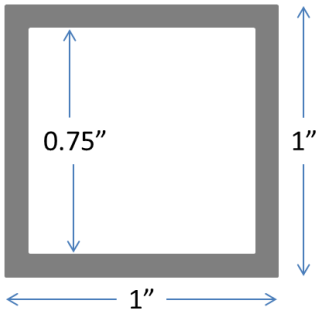

Figure 4.1 A schematic of the mask used for thin film deposition using drop casting.

The mask was secured to the substrate with binder clips to prevent the solution from leaking out and wetting the bottom of the substrate. The mask-covered substrate was placed on a leveled surface and 120 µL of 6 mg/ml NC solution was poured inside the mask using precision pipettes. Following, the substrate was covered with an inverted funnel for slow evaporation of the solution (Figure 4.2). These conditions resulted in evaporation rates that were 3-4 µL/min. After the film dried (~30-45 min), the mask was removed and the film was treated with 10% pyridine solution by volume in acetonitrile for 4-5 minutes to exchange oleylamine and oleic acid ligands with pyridine. Following, the film was dried on a hot plate at 200 °C for a minute. The above thin film deposition steps were repeated 4 times to give 3-4 µm thick CZTS NC films.

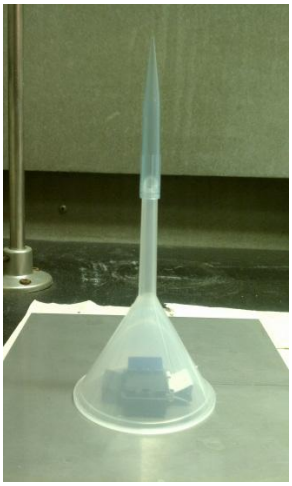

Figure 4.2 Photograph of a NC film being dried under an inverted funnel.

Films from Doctor Blading: As-synthesized CZTS NCs were cleaned twice as described previously and dried under flowing nitrogen. Dried powders of CZTS NCs were redispersed in 1-hexanethiol and sonicated for an hour to give a paste of concentration 200 mg/ml (4.4% volume of solids in solution). Scotch tape™ was used as doctor blading guide and tape thickness determined the initial thickness of the doctor bladed film (40 microns). Small amount of NC paste was applied in between the guides and a flat spatula was used to match the thickness of the NC film to that of the guide. Subsequently, the NC films were dried by placing them for 1 minute on a hot plate maintained at 300 °C. NC films cracked on drying. A second coat of the paste was then applied in a manner similar to the first one to fill the cracks in the first layer, thus giving the final film. Each layer of NC films was found to be ~5 μm thick.

Annealing: NC films were annealed in an argon atmosphere on a heating stage. Prior to annealing the NC films, the anneal chamber containing the heating stage was degassed and filled back with nitrogen multiple times to reduce the oxygen concentration within the chamber. During annealing, the argon flow rate was set to 200 sccm. The heating rate of the stage was set to 10 °C/min for films annealed between 275-500 °C. For films annealed at 600 °C, the heating rate was set to 120 °C/min to quickly heat the film to the required temperature and minimize sulfur loss during the heating process. Typically, the films were annealed for 15 minutes. The anneal temperatures reported here correspond to the actual temperature of the stage and were measured using a thermocouple. The set point temperatures were higher than the measured temperatures.

Characterization Details: X-ray diffraction (XRD) patterns from the NC films were collected and recorded using a Bruker-AXS microdiffractometer equipped with a Cu-Kα X-ray source. Raman scattering from the films was measured using a Witec confocal Raman microscope equipped with an argon laser for excitation at 514.5 nm. The Raman scattered photons were collected and detected using a monochromator with an 1800 lines/mm grating. Optical images were acquired using Hirox KH 7700 digital video microscope. Scanning electron microscopy (SEM) images were obtained using a JEOL

6500 field-emission gun microscope. Fourier transform infrared (FTIR) absorption spectra were collected using a Nicolet Magna 550 series II FTIR spectrophotometer with an attenuated total reflection (ATR) accessory (Harrick Scientific) and a Glowbar source. The infrared beam was focused normal onto the 45° beveled edge of the trapezoidal Ge ATR crystal ($5 \times 1 \times 0.1$ cm^3). Aliquots of colloidal CZTS suspensions were cast onto the Ge ATR crystal and allowed to dry before recording their FTIR spectrum.

4.3 Results and Discussion

The morphology and thickness of thin films drop cast from NC dispersions were found to depend sensitively on the dispersion concentration, the amount of excess ligand in the dispersion solution, the drying rate, whether the metal mask was used, and use of a leveled surface. Some of the observed phenomena are well known. For example, when the films were left to dry in air without a funnel, the films exhibited concentric rings at its edges where the NC film was thicker. These types of patterns are similar to the coffee-ring patterns that form when coffee containing small ground coffee particles dries on a surface. Such coffee-ring patterns have been previously observed in thin film coatings and have been attributed to the pinning of the contact line of the drying drop and subsequent concentration of particles at the contact line.[4] Pinning and sliding of the contact line gives rise to concentric ring like pattern. The coffee-ring pattern formation is promoted by fast evaporation of solvent. When the solvent evaporation rate is reduced, for example, by covering the substrate with a funnel, uniform NC films without ring patterns were obtained. The substrates must be placed on a leveled surface during drying to obtain uniform films; a slight tilt in the substrate yielded films that were thicker on one edge and thinner on the opposite side. Films cast on Mo-coated glass substrates without using metal mask were nonuniform: the film deposited in the center was much thicker than the film deposited near the edges. The use of metal mask improved film uniformity. Films deposited with a metal mask were uniform in the center: the edges very near the

frame were slightly thicker. Solar cells can be made in the uniform center region without any undesirable effects from the thicker edges. The amount of oleic acid ligand in the NC dispersion used for thin films deposition influenced the thickness and the uniformity of the deposited films; high ligand concentration in the dispersion resulted in no film deposition, whereas low concentrations of the ligand in the dispersion caused the NCs to agglomerate even before the films were cast. The films cast from dispersions that contained agglomerates resulted in isolated islands instead of continuous thin films. The presence of oleic acid ligands prevents the NCs from aggregating in solution. However, an excess of oleic acid prevents the NCs from sticking onto the substrate; as the volume of the solution reduces upon drying, the NCs get pulled towards the edge of the mask due to capillary effect, thereby leading to no film formation. As even very subtle changes in the oleic acid concentration within the solution led to differences in the morphology of the final film, it was difficult to characterize the change in the oleic acid concentration using rheological measurements; the theoretical change in viscosity corresponding to the oleic acid change was found to be too small to be resolved by a rheometer.

The dispersion concentration determined the thickness of the films deposited through drop casting. Figure 4.3 shows the optical images of drop-casted thin films from various concentration NC dispersions. Specifically, films drop-cast from 120 µl of 100 mg/ml, 30 mg/ml, and 3 mg/ml NC dispersions had a thickness of 10 µm, 3 µm, and 800 nm, respectively. The NC dispersion concentrations were estimated by dividing the total yield with the volume of toluene used to disperse the NCs. The film thicknesses were measured near the center of the substrate by means of an optical microscope. The film thicknesses were estimated by measuring the movement of the optical microscope on changing the focus from the top of the substrate to the top of the NC film. Some of the NCs drop-casted on the substrate get lost by seeping under the frame. In addition, the NCs are also lost at the edges as the NC films are thicker at the edges as compared to the center due to the mask. If we assume a uniform thickness of the NC film across the substrate, the NC film from 3 mg/ml solution can be estimated to be 75% porous. The 10 µm and 3 µm films cracked upon drying. Films crack to relax the stresses that are built up

during drying.[5] Figure 4.3 shows that the 10 µm and 3 µm thick films exhibit 100 µm and 2 µm wide cracks, respectively. In contrast, the 800 nm thick film had no visible cracks. Solar cells require ~ 1-2 µm thick films but it was not possible to deposit films that are thicker than 1 µm in a single drop-casting step; a 1-2 µm thick film would crack and result in an electrical short circuit.

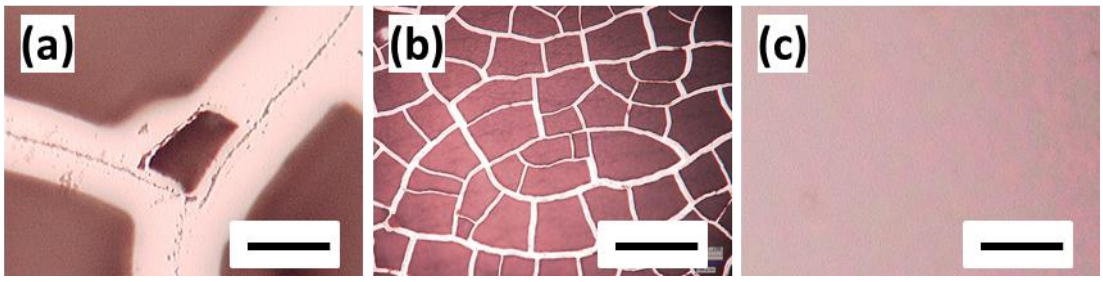

Figure 4.3 Thin films deposited through drop casting from 5 nm CZTS NC dispersions. Films for images (a), (b), and (c) were deposited using NC dispersions of concentration 100 mg/ml, 30 mg/ml, and 3 mg/ml, respectively. Image (d) is a zoomed out version of image (c) showing the absence of cracks over a wide region of the film. All the scale bars are 100 µm long.

As-synthesized NCs are capped with oleylamine and oleic acid ligands as evidenced from FTIR data presented in Chapter 3. The presence of these long alkyl-chain ligands on the NC surface would prevent close packing of the NCs and increase the film's porosity. In addition, annealing NC films containing long chain carbon ligands may lead to residual carbon in the annealed film, thereby affecting the device performance. To remove the oleylamine and oleic acid ligands from the NC surface, we explored the possibility of exchanging them with pyridine and monitored the progress of the ligand-exchange using attenuated total reflectance - Fourier transform infrared (ATR-FTIR). FTIR spectra were collected from NC films cast on trapezoidal Ge ATR-FTIR crystals after 5, 10, and 20 minutes of soaking the films in pyridine. Figure 4.4 shows that the intensity of the C-H stretch region (2800-3000 cm^{-1}) does not change after the initial 5 minutes of soaking in pyridine. Comparing the FTIR spectrum of oleic acid, oleylamine, and pyridine to the experimental spectra of ligand exchanged NC films, the C-H stretch region appears to be arising only from the oleic acid and oleylamine ligands.

Assuming the ratio of the area under the C-H stretch region in the as-synthesized film to the ligand exchanged film to be an indicator of the extent of ligand exchange of the NC films, we estimate that 65% of the initial ligands were exchanged with pyridine ligands after 5 minutes of soaking in neat pyridine. To cast films where the NC surfaces are capped with pyridine, the oleylamine and oleic acid ligands were exchanged with pyridine prior to depositing a second layer of oleylamine and oleic acid capped NCs on the substrate. The ligands on the second layer of NCs were also exchanged with pyridine. In both cases, the ligands were exchanged using 10% pyridine solution in acetonitrile instead of neat pyridine because soaking in neat pyridine caused the NC films to peel off from the substrate. After ligand exchange, the substrates were heated for 1 minute by placing them on a hot plate maintained at 200 °C to evaporate the low boiling point pyridine ligands (b.p. 115 °C) and make the films more compact. When the oleylamine and oleic acid ligands are exchanged with pyridine, the NCs move closer to each other in both the lateral and the vertical directions; this leads to cracking of the films (Figure 4.5) and reduction of the film thickness from 800 nm to 500 nm.

NC ligand exchange is particularly beneficial when depositing multiple layers on top of each other. Casting a second layer of NCs on top of an already dried thin film of NCs capped with oleylamine and oleic acid results in the NCs from the first layer redispersing into solution. This effectively translates into thin film deposition from a solution that is twice the initial concentration and therefore invariably leads to cracking of the resulting films. When the oleylamine and oleic acid ligands of the first layer of NCs are exchanged with pyridine, the NCs are not redispersed into toluene during the casting of the second layer. Thus, the casting of the second layer can be achieved without disturbing the first layer. This relieves the film stress at the interface of the two films and prevents cracking of the film.

Cracking of the film after ligand exchange indicates that it is impossible to obtain a crack-free NC film by depositing only a single layer of NCs. Multilayer NCs deposition is inevitable and is necessary to fill the cracks in a previous layer with the next. The 3

mg/ml dispersion would require 6-8 layers to achieve a final compact layer that is 1-2 µm thick. We, therefore, decided to increase the concentration to 6 mg/ml, and deposited multiple layers using the same. Although these thicker films deposited from oleylamine and oleic acid capped NCs are cracked due to stresses that build up during drying, the crack width is comparable to the width of the cracks formed after ligand exchange. The crack width in the thin films deposited from 6 mg/ml NC dispersions which is ~100-200 nm does not change significantly from the first layer up to the sixth layer deposited on top of it (Figure 4.6). SEM images of CZTS thin films after deposition of 4 layers of NCs (Figure 4.7) indicate that the film is continuous; however the film is very porous as shown in Figure 4.7(b). Assuming a uniformly thick NC film across the substrate, the NC film can be estimated to be 60 % porous. However, as stated before, the actual porosity may be much more than the estimated value.

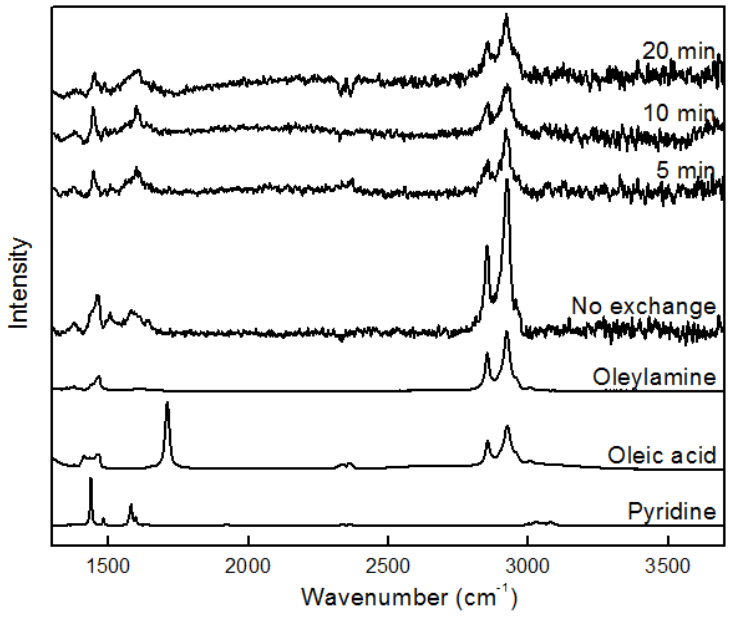

Figure 4.4 FTIR spectra from thin CZTS NC films drop-cast using 30 µL of 3mg/ml CZTS NC dispersion on Ge ATR-FTIR crystal substrates before and after soaking the films in neat pyridine for 5, 10, and 20 minutes. The data was collected using the same NC film on Ge substrate soaked in pyridine for the times indicated on the plot. The C-H peak intensity (2800-3000 cm^{-1}) does not change significantly after 5 minutes of exchange. Individual FTIR spectra have been offset for clarity.

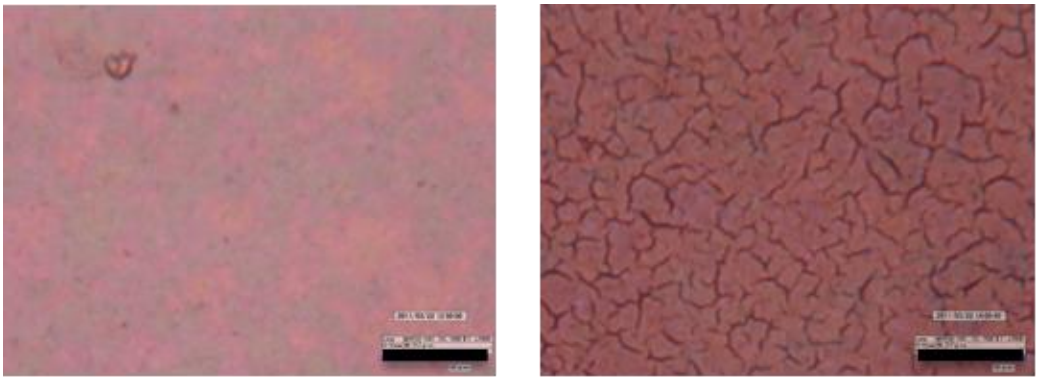

Figure 4.5 A comparison of NC thin films deposited using 120 µL of a 3 mg/ml CZTS NC dispersion before (left) and after (right) ligand exchange. The scale bar is 10 µm long.

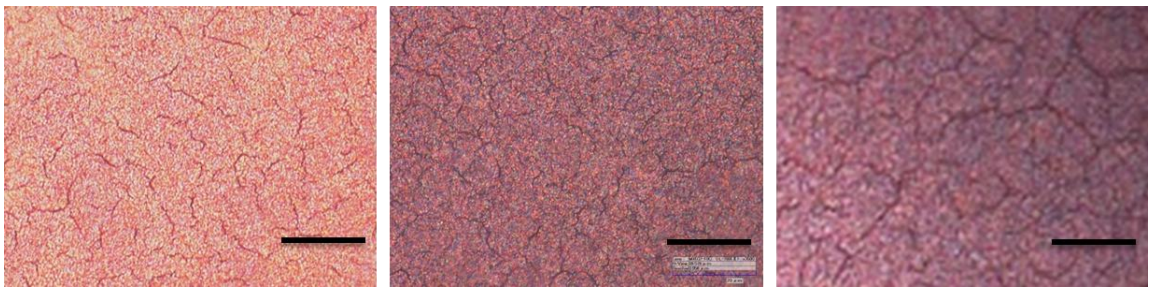

Figure 4.6 CZTS NC films after deposition of 1 (left), 3 (middle), and 6 (right) layers of NCs. All films were deposited using 120 µL of 6 mg/ml CZTS NC dispersions for each deposition cycle and exchanged with pyridine before imaging. All the films look identically cracked with negligible dependence of crack width on the number of deposited layers. The film thickness are 1 µm, 2.9 µm, and 5.9 µm, respectively. The scale bars on all the images are 20 µm.

The NC thin films were annealed in argon atmosphere for grain growth. Bulk CZTS thin films were annealed for different durations between 30 minutes and 4 hours and at temperatures ranging from 500 to 600 °C depending on the specific deposition process. Typically, many researchers anneal thin films either in H_2S gas or in S vapor to keep high sulfur chemical potential over the film.[6-9] This is thought to prevent sulfur loss from the film and diffuse additional sulfur into the film. Selenium vapor is also used to form CZTSe or alloys.[10,11] Weber *et al.* found that thin films annealed without excess S lose Sn and become non-stoichiometric after annealing.[12] In addition, the presence of S

(or Se) promotes grain growth and yields films with grain sizes between 0.5 and 1 μm.[10] Sulfidation of films can be cumbersome and toxic if for example H_2S or H_2Se are used. Since the NC films are already stoichiometric and even have some excess S, we annealed the NC films in argon rather than in S or H_2S to test the viability of this approach.

Figure 4.8 shows the XRD from a NC film that was annealed at 600 °C in argon atmosphere for 4 hours. The XRD pattern suggests that this NC film lost S upon annealing. In fact, the (112) CZTS peak at 2θ=28.5° has virtually disappeared upon annealing. The most intense peak in the XRD pattern was the (101) Cu-Zn alloy peak. In addition, the XRD from this film also exhibited SnO_2 peaks. Thus, this data suggests that upon loss of S from the film, Cu and Zn formed a Cu-Zn alloy, and the remaining Sn was oxidized to form SnO_2. The residual oxygen or water vapor inside the anneal chamber may be responsible for the oxidation of the films. Another possibility is that the quartz substrate may be degassing oxygen upon heating, leading to oxidation of the films. In order to reduce the sulfur loss from the film, we decreased the annealing time from 4 hours progressively to 5 minutes and characterized the resulting films using XRD. Figure 4.9 shows the XRD from films annealed for durations ranging from 5 minutes to 4 hours. As the annealing time is increased, S loss and oxidation of the films worsen progressively and CZTS peak decreases. However, for films that were annealed for 5 minutes, the CZTS peak became sharper than the NC films and remained sharp. In addition, CZTS films from NCs exhibited grain growth even in a short anneal of 5 minutes (see below).

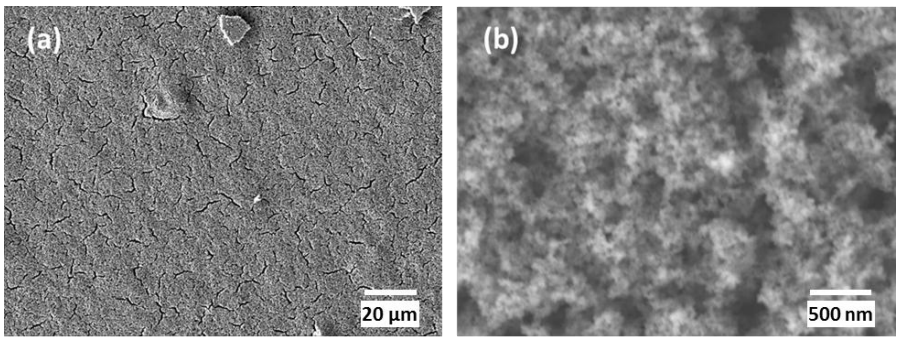

Figure 4.7 SEM images of CZTS NC thin film after deposition of 4 layers of NCs. Although the films look quite continuous, they are very porous. This film was found to be 3.9 μm thick.

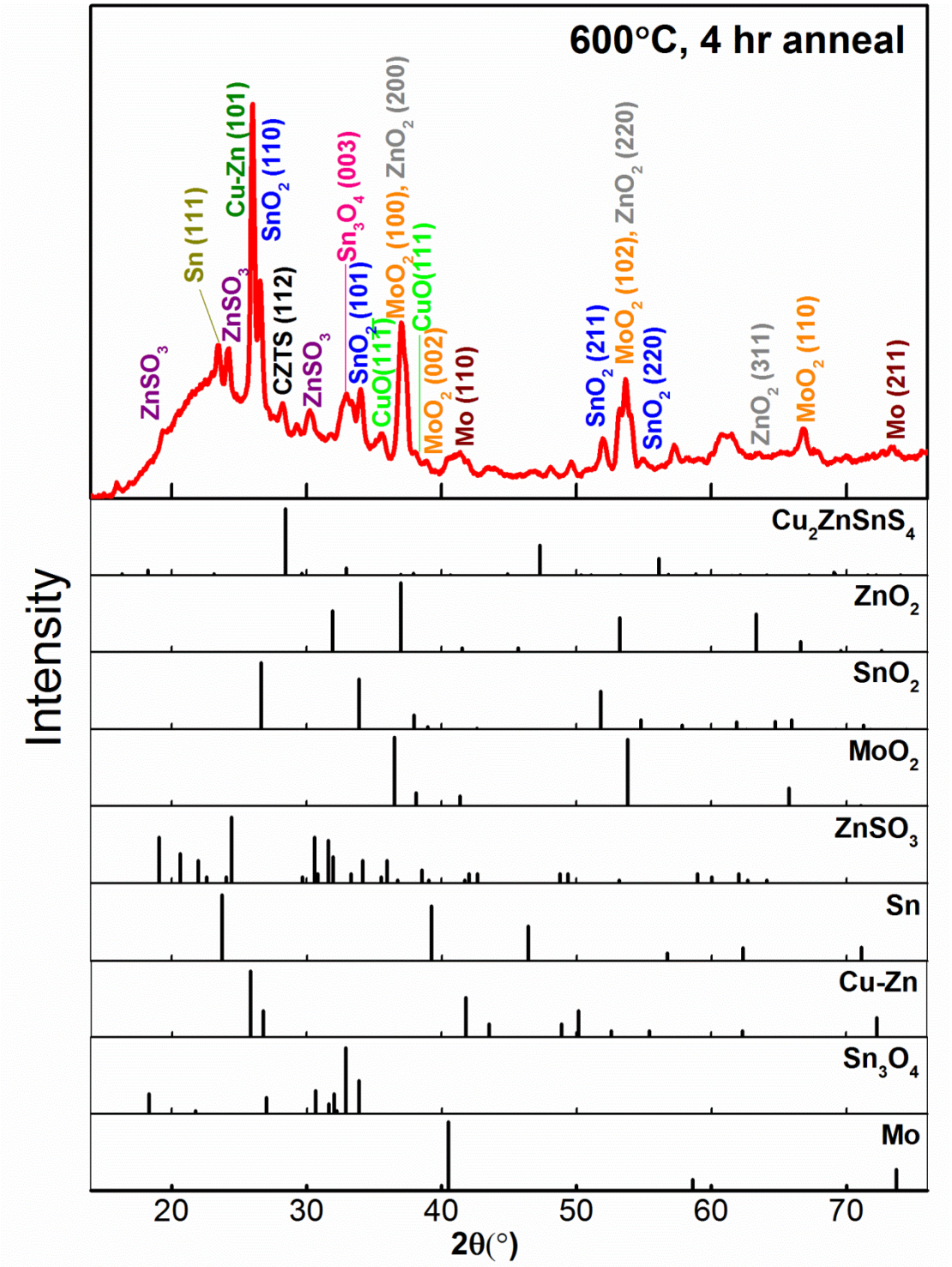

Figure 4.8 XRD pattern from CZTS thin film annealed for 4 hr. in argon at 600 °C. JCPDS patterns of the possible phase impurities are also plotted for comparison.

The annealing temperature was varied from 275-600 °C in order to understand its effect on the grain growth in NC films. Figure 4.10 shows the XRD from films annealed in argon at various temperatures between 275 and 600 °C. All the films were annealed for 15 minutes except that at 600 °C, which was annealed for 5 minutes to minimize the S loss and oxidation. The XRD from all the films look nominally similar and match to that expected from CZTS. The XRD peaks from the NC film annealed at 275 °C is still broad and Scherrer analysis gives an average crystallite size of ~11 nm indicating only limited grain growth compared to the 5 nm crystallite size of the unannealed film. For the films annealed at 350 °C and above, it is not possible to estimate the crystallite size using the Scherrer analysis, as the crystallite size reached the instrument resolution limit which is ~60 nm. Careful examination of the XRD data shows that all the films annealed at temperatures greater than or equal to 350 °C contain a secondary phase along with CZTS (Figure 4.11). Specifically, the films annealed at temperatures between 350-500 °C contained SnO_2 as a minor phase. The film annealed at 6°0 °C contained $Cu_{1.81}S$, but surprisingly it did not contain any SnO_2. This may be due to the shorter anneal time used at 600 °C.

Figure 4.12 shows the SEM images from films annealed at various temperatures between 275 and 600 °C. These images reveal that the films are heavily cracked and form small islands. This may be due to the high porosity of the unannealed NC film. The films annealed at 275 °C look porous like the unannealed drop-cast NC film indicating very little grain growth at that temperature. This is consistent with the broad XRD peaks for this film. The film annealed at 350 °C appears less porous than the 275 °C annealed film. However, it is not easy to extract the grain size from the SEM images as the film is still porous. The film annealed at 425 °C appears very similar to that annealed at 350 °C. The film annealed at 500 °C appears compact and most of the voids between the NCs forming the small islands look filled in. However, the film peeled from the substrate and existed only in patches. Interestingly, while all the films annealed up to 600 °C resembled the morphology of the initial NC film, the film annealed at 600 °C did not show any NC-like morphology. In fact, the film appeared as though formed from molten NCs. However,

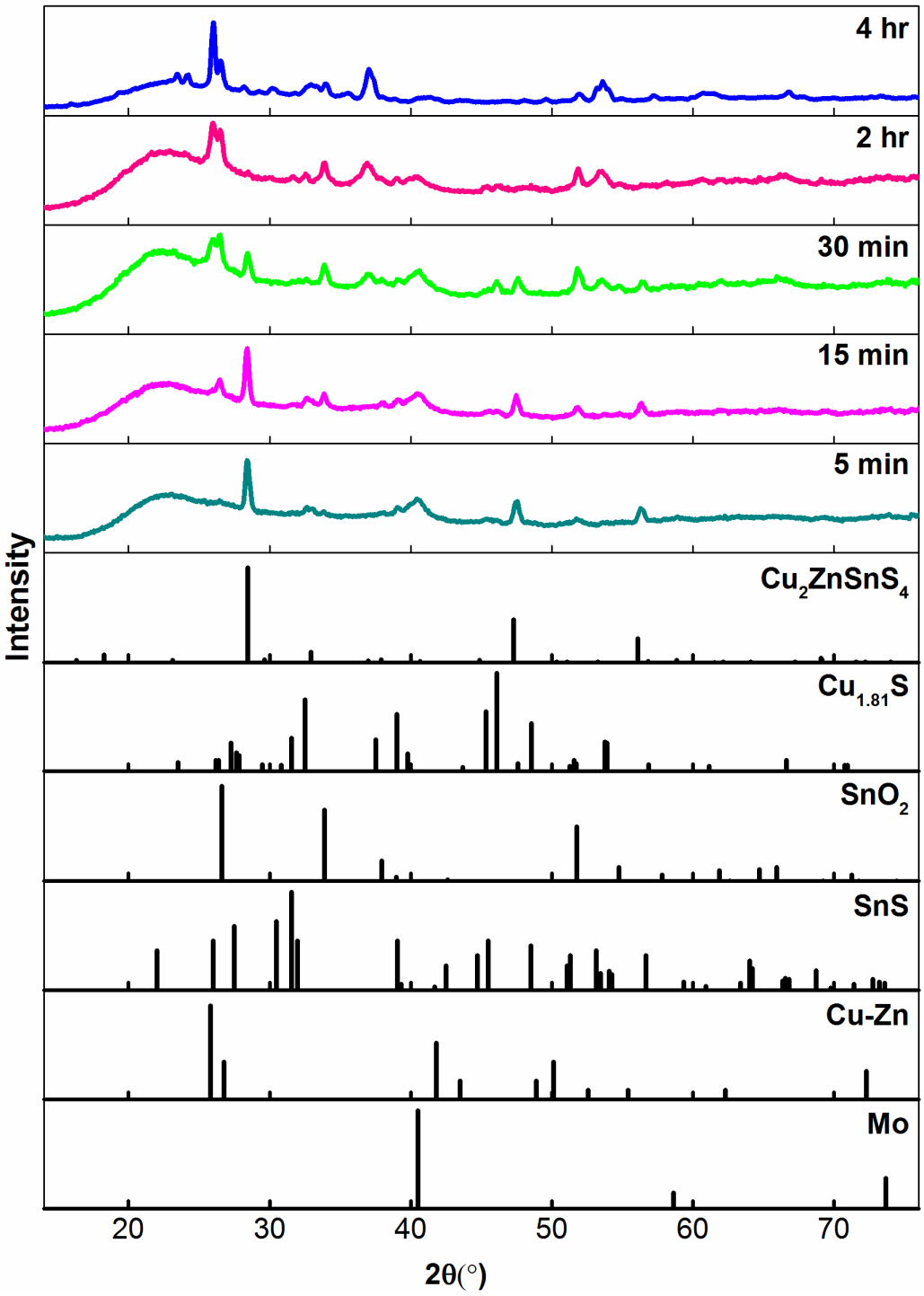

Figure 4.9 XRD patterns from CZTS NC films annealed at 600 °C in argonas a function of time. The anneal time is indicated against individual XRD patterns. Standard JCPDS patterns of probable phases are plotted for comparison.

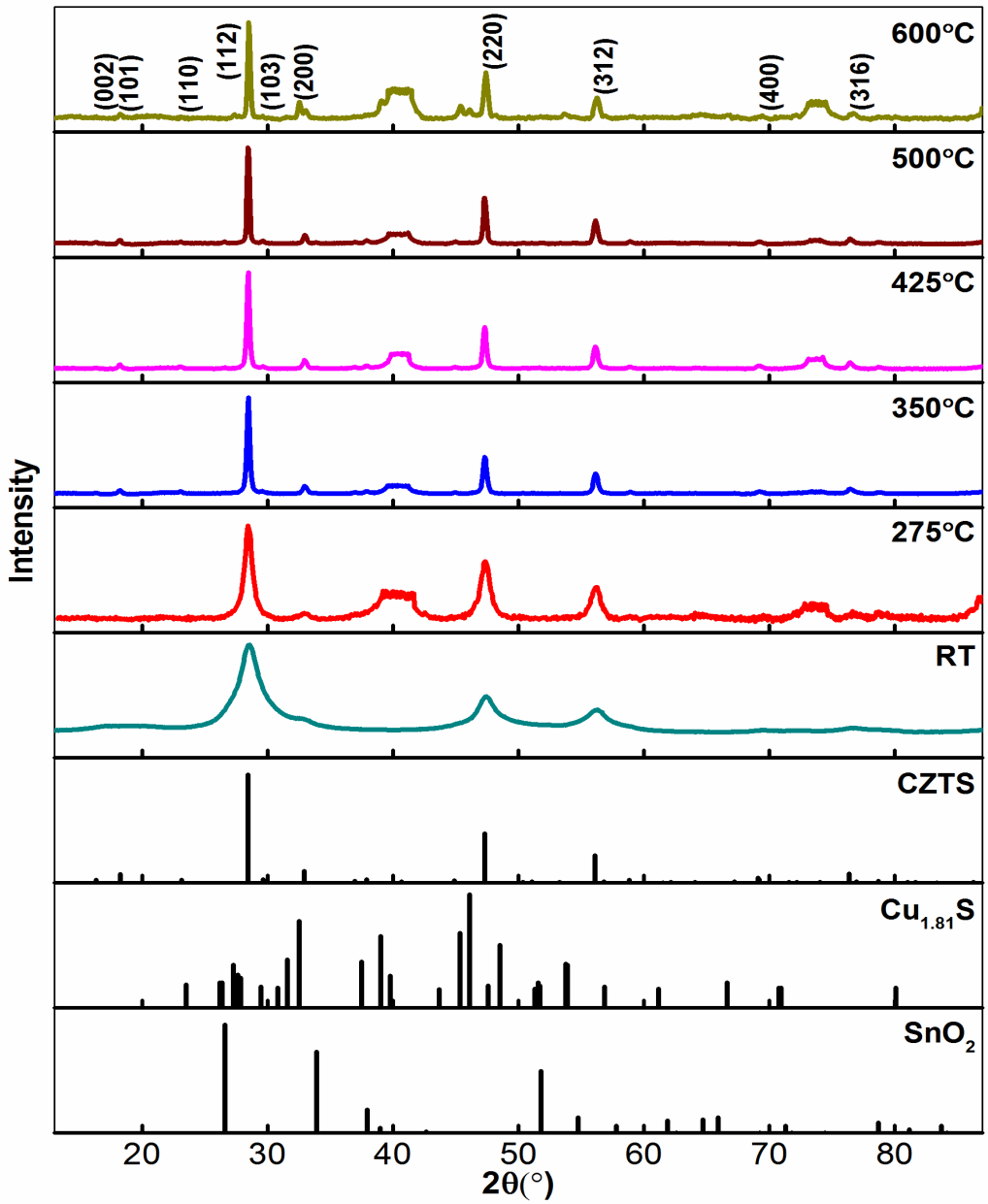

Figure 4.10 Background subtracted XRD patterns for CZTS NC films annealed at temperatures ranging from 275-600 °C. The NC film annealed at 600 °C was annealed for 5 minutes. All other films were annealed for 15 minutes. The XRD pattern for the unannealed film has also been plotted for comparison. The JCPDS patterns for CZTS, $Cu_{1.81}S$, and SnO_2 have been plotted for reference. XRD peaks for CZTS have been indexed for the 600 °C annealed film XRD pattern. Mo substrate peaks at 2θ=40.5°, 73.7° have been clipped for clarity.

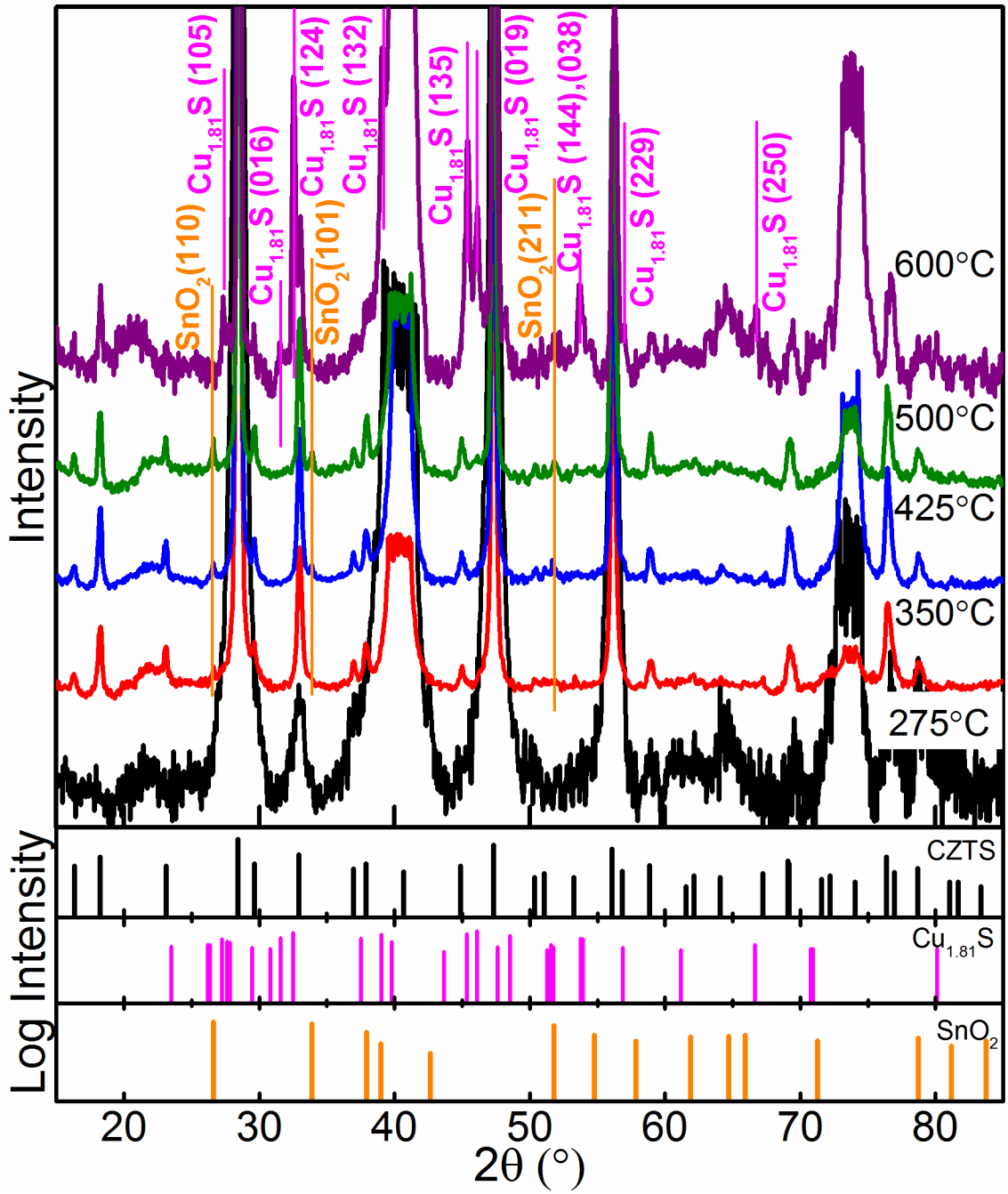

Figure 4.11 Background subtracted XRD patterns for NC films annealed at various temperatures. The plot highlights the peaks of the minor phases present within the samples. SnO_2 peaks have been marked in orange whereas $Cu_{1.81}S$ peaks have been marked in pink. The JCPDS patterns for CZTS, $Cu_{1.81}S$ and SnO_2 have been plotted on a log scale to highlight the minor peaks. Mo substrate peaks at 2θ=40.5°, 73.7° have been clipped for clarity. XRD patterns for the different films have been offset for clarity.

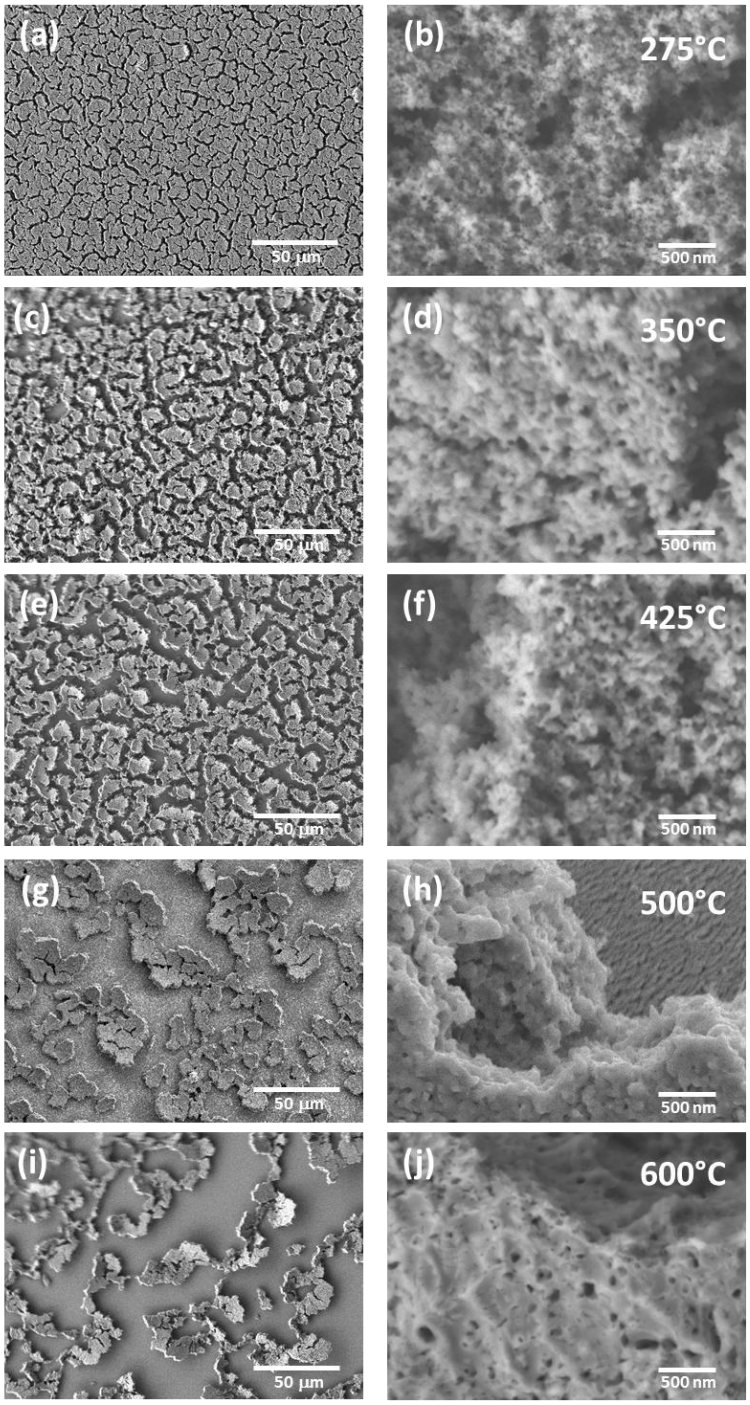

Figure 4.12 SEM images of NC films annealed at temperatures ranging from 275 to 600 °C. Both the images in a given row belong to the same NC film annealed at the temperature indicated on the right. All the images in a given column have the same scale.

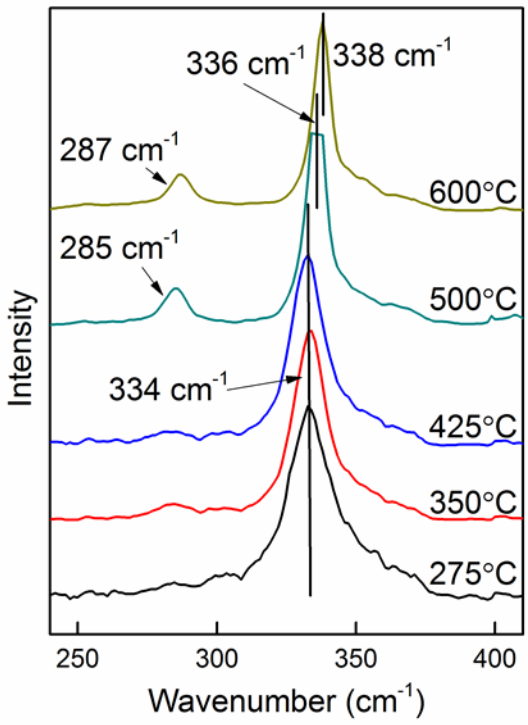

Figure 4.13 Raman spectra from CZTS NCs annealed at temperatures ranging from 275 to 600 °C. The most intense Raman scattering peak progressively shifts from 334-338 cm^{-1} on increasing the anneal temperature. Individual Raman spectra have been offset for clarity.

some voids are still present within the annealed film. In addition, this film peeled off from the substrate similar to the one annealed at 500 °C. On increasing the anneal temperature, the surface coverage of the annealed film reduces progressively with the increasing compactness of the film. The film shrinks to form islands as the initial films from NCs are highly porous.

Because one cannot distinguish CZTS from Cu_2SnS_3 and ZnS based on XRD alone, we also analyzed the annealed films using Raman spectroscopy (Figure 4.13).[13,14] The most intense Raman scattering peak for all the films was close to that of CZTS at ~338 cm^{-1}. The Raman scattering peak appeared at 334 cm^{-1} for films annealed between 275 and 425 °C. This peak shifted to 336 cm^{-1} and 338 cm^{-1} for the films annealed at 500 °C and 600 °C, respectively. The films annealed at 500 °C and 600 °C also showed the

second most intense scattering peak for CZTS at ~ 287 cm^{-1}. The CZTS thin film Raman peaks became progressively sharper with increasing annealing temperature.

Thin film formation from NC dispersions using drop casting is caused by diffusion-limited aggregation.[15] Due to this, the deposited films are very porous. As the films densify during annealing they crack. Thin film deposition from higher solid volume fraction dispersions using doctor blading is, not by diffusion-limited aggregation and can yield lower porosity and more compact films. In order to decrease the porosity, we investigated the possibility of depositing NC thin films using doctor blading. Films deposited using doctor blading were also cracked [Figure 4.14 (a)], with crack widths as large as 10 μm in some regions of the film. A second layer of NCs was deposited on the first layer to fill the cracks in the first layer [Figure 4.14 (b)]. Films deposited using two layers of NCs cracked much more than the ones with only a single layer.

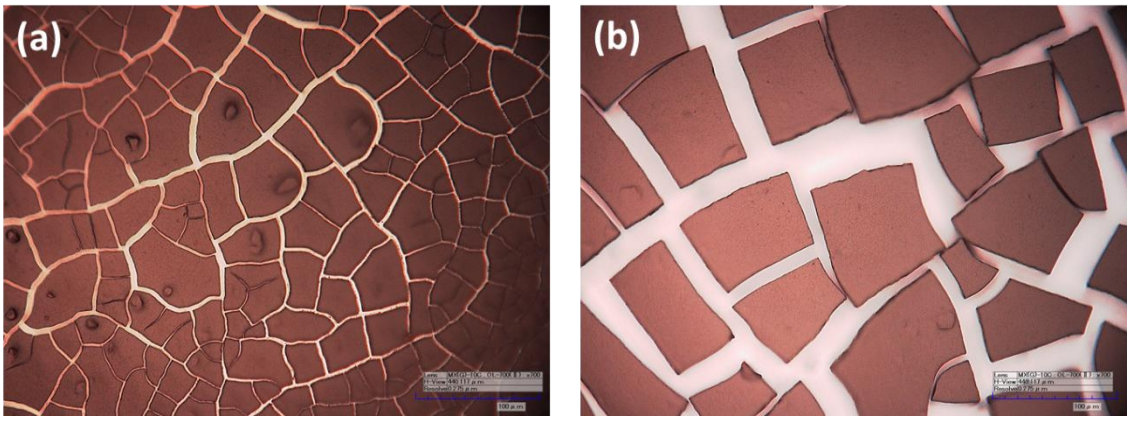

Figure 4.14 CZTS NC films deposited using doctor blading after depositing (a) first layer (b) second layer from a 200mg/ml paste of CZTS NCs dispersed in hexanethiol.

As-synthesized CZTS NCs are capped with oleic acid and oleylamine ligands which are ~ 1 nm long. For a 5 nm diameter NC, the ratio of NC volume to the total volume of NC with ligand is 0.36. This ratio increases to 0.58 for 10 nm diameter NCs and 0.75 for 20 nm diameter NCs. This indicates that even if the NCs are perfectly packed with an FCC packing, only about 27% of the total volume is occupied by NCs with the rest 73% being empty. Thus, NC diameter appears to be one of the primary

reasons for the large porosity within the annealed films. NCs of larger diameter are needed for depositing compact films from NC dispersions.

4.4 Conclusion

In conclusion, CZTS thin films were deposited using drop casting from dispersions of 5 nm diameter CZTS NCs. The drop cast films can be made continuous, with crack widths no larger than 100 nm. However, the films are >75% porous. Annealing the NC films in argon atmosphere at temperatures ranging from 275-600 °C led to grain growth and compaction of the films. Annealed films were nominally CZTS with a small impurity phase of either SnO_2 or $Cu_{1.81}S$. The NC films cracked upon annealing and peeled off from the substrate. The primary reason for the cracking observed in the annealed films appears to be due to the small diameter of the NCs. Larger diameter NCs may give more continuous and compact films upon annealing.

4.5 References

1 M. G. Panthani, V. Akhavan, B. Goodfellow, J. P. Schmidtke, L. Dunn, A. Dodabalapur, P. F. Barbara, and B. A. Korgel, J. Am. Chem. Soc. **130**, 16770 (2008).
2 K. S. Leschkies, R. Divakar, J. Basu, E. Enache-Pommer, J. E. Boercker, C. B. Carter, U. R. Kortshagen, D. J. Norris, and E. S. Aydil, Nano Lett. **7**, 1793 (2007).
3 K. S. Leschkies, T. J. Beatty, M. S. Kang, D. J. Norris, and E. S. Aydil, ACS Nano **3**, 3638 (2009).
4 R. D. Deegan, O. Bakajin, T. F. Dupont, G. Huber, S. R. Nagel, and T. A. Witten, Nature **389**, 827 (1997).
5 W. P. Lee, and A. F. Routh, Langmuir **20**, 9885 (2004).
6 T. Washio, T. Shinji, S. Tajima, T. Fukano, T. Motohiro, K. Jimbo, and H. Katagiri, J. Mater. Chem. **22**, 4021 (2012).
7 K. Woo, Y. Kim, and J. Moon, Energy Environ. Sci. **5**, 5340 (2012).
8 W. Ki, and H. W. Hillhouse, Adv. Energy Mater. **1**, 732 (2011).
9 H. Katagiri, Thin Solid Films **480-481**, 426 (2005).
10 Q. Guo, G. M. Ford, W. Yang, B. C. Walker, E. A. Stach, H. W. Hillhouse, and R. Agrawal, J. Am. Chem. Soc. **132**, 17384 (2010).

11 T. K. Todorov, K. B. Reuter, and D. B. Mitzi, Adv. Mater. **22**, E156 (2010).
12 A. Weber, R. Mainz, and H. W. Schock, J. Appl. Phys. **107**, 013516 (2010).
13 A. J. Cheng, M. Manno, A. Khare, C. Leighton, S. A. Campbell, and E. S. Aydil, J. Vac. Sci. Technol. A **29**, 051203 (2011).
14 P. A. Fernandes, P. M. P. Salome, and A. F. da Cunha, Thin Solid Films **517**, 2519 (2009).
15 T. A. Witten, and L. M. Sander, Phys. Rev. Lett. **47**, 1400 (1981).

Chapter 5

Facile Synthesis of Microporous Films of Cu_2ZnSnS_4 From Dithiocarbamate Complexes

We have synthesized microporous films of Cu_2ZnSnS_4 using a facile synthesis technique employing the thermal decomposition of metal dithiocarbamate complexes. As-synthesized films were characterized using XRD, SEM, Raman spectroscopy, and EDX, and established to be CZTS. Films from thermal decomposition of metal dithiocarbamates were found to be microporous, with the size of the microspheres being dependent on the anneal temperature. The effect of the variation in heating rate and the addition of oleylamine to the structural properties of the annealed films was also studied.

5.1 Introduction

Cu_2ZnSnS_4 (CZTS), $Cu_2ZnSnSe_4$ (CZTSe), and their alloys $Cu_2ZnSn(S,Se)_4$ (CZTSSe) are emerging as promising materials for thin film solar cells.[1-3] These materials contain earth abundant, inexpensive, and environmentally benign elements. Moreover, the absorption coefficient of CZTS, CZTSe, and their alloy CZTSSe in the visible region of the electromagnetic spectrum is $>10^4$ cm^{-1},[2,3] and a 1 μm thick layer of these materials can absorb most of the photons with energies greater than their respective band gaps. CZTS and CZTSe have bandgaps of 1.45 and 1 eV, respectively, while the CZTSSe bandgap can be tuned to cover the range between these two values. This range of bandgap energies is ideal for achieving the highest theoretical efficiencies in a single junction solar cell.[4] Recently, a CZTSSe solar cell with overall power conversion efficiencies exceeding 10% has been reported.[5] The potential for CZTS as a photocathode material for water splitting has also been explored.[6] In that study, a CZTS electrode with a hollow columnar surface structure gave the highest photocurrent. Using a microporous

film of CZTS as photocathode could further enhance the photocatalytic activity of such a cell.

CZTS thin films have been synthesized using several techniques, including, vacuum deposition processes, such as co-evaporation,[7] co-sputtering,[8] sulfidation of copper-zinc-tin film stacks, [9] chemical vapor deposition,[10] and pulsed laser deposition,[11] and solution based techniques, such as chemical bath deposition,[12] electrodeposition,[13] spin coating from precursor solutions,[14] and casting from nanocrystal dispersions.[15-18] Here, we report the facile synthesis of CZTS microporous films beginning with environmentally benign metal dithiocarbamate complexes.

5.2 Experimental section

Materials: Copper (II) chloride dihydrate ($CuCl_2.2H_2O$, ACS grade, 99+%), tin (IV) chloride pentahydrate ($SnCl_4.5H_2O$, 98%), zinc chloride ($ZnCl_2$, reagent grade, 98%), sodium diethyldithiocarbamate trihydrate (Nadedc.$3H_2O$, ACS grade), chloroform (HPLC grade, ≥99.8%), oleylamine (OM, technical grade, 70%), and acetone (ACS Reagent, ≥99.5%) were purchased from Sigma-Aldrich. Reagent alcohol (histological grade, 90% ethyl alcohol, 5% methyl alcohol, 5% butyl alcohol) was obtained from Fisher Scientific. All chemicals were used as delivered without further purification. Ultra-high purity water (18 MΩ) was obtained from a Millipore Direct-Q water purification system.

Synthesis of Copper Diethyldithiocarbamate [$Cu(dedc)_2$]: 9.0 g of sodium diethyldithiocarbamate was dissolved in 150 mL of reagent alcohol and added dropwise to a solution of 4.23 g of copper chloride in 50 mL reagent alcohol (85 mg/mL) with constant stirring. The black precipitate that formed upon reaction was filtered and washed multiple times with ultra-high purity water before drying in a desiccator. Copper diethyldithiocarbamate crystals were purified by recrystallization from chloroform and dried overnight in vacuum before use. The crystals melted at 200 °C.

Synthesis of Zinc Diethyldithiocarbamate [$Zn(dedc)_2$]: 9.0 g of sodium diethyldithiocarbamate was dissolved in 150 mL of reagent alcohol and added dropwise to a solution of 3.38 g of zinc chloride in 50 mL of reagent alcohol (68 mg/mL) with constant stirring. The white precipitate that formed upon reaction was filtered and washed multiple times with ultra-high purity water before drying in a desiccator. Zinc diethyldithiocarbamate crystals were purified by recrystallization from chloroform and dried overnight in vacuum before use. The crystals melted at 181 °C.

Synthesis of Tin Diethyldithiocarbamate [$Sn(dedc)_4$]: 12.85 g of sodium diethyldithiocarbamate was dissolved in 200 mL of reagent alcohol and added dropwise to a solution of 2.5 g of tin tetrachloride in 50 mL of reagent alcohol (50 mg/mL) with constant stirring. The orange precipitate that formed upon reaction was filtered and washed multiple times with ultra-high purity water before drying in a desiccator. Tin diethyldithiocarbamate crystals were purified by recrystallization from acetone and dried overnight in vacuum before use. The crystals melted at 170 °C.

Synthesis of Copper-zinc-tin Diethyldithiocarbamate [$Cu_2ZnSn(dedc)_{10}$]: 7.26 g of sodium diethyldithiocarbamate was dissolved in 150 mL of reagent alcohol and added dropwise to a solution of 1 g copper chloride, 0.40 g zinc chloride, and 1.03 g of tin tetrachloride (Cu:Zn:Sn=2:1:1) in 100 mL of reagent alcohol with constant stirring. The grey precipitate that formed upon reaction was filtered and washed multiple times with ultra-high purity water before drying in a desiccator. The dried powder melted at 151°C.

Microporous Film Deposition: 250 µL of 0.025 M solution of copper diethyldithiocarbamate, zinc diethyldithiocarbamate, and tin dimethyldithiocarbamate in chloroform was dropped onto a 1”×1” Mo-coated fused silica substrate and allowed to dry slowly by covering the substrate with an inverted funnel (Figure 4.2). This film was heated in an air-free atmosphere at a rate of 15 °C/min to 150 °C. Subsequently, the films were heated to 275 °C. The heating rate between 150-275 °C was varied between 0.5 and 30 °C/min. After reaching 275 °C, the films were heated at a rate of 10 °C/min to a final temperature of 375 °C where they were annealed for 2 hr. Following this heating and

annealing protocol, the films were cooled to room temperature at the natural cooling rate of the holder that the substrates were placed on by turning off the heater.

Films from copper-zinc-tin diethyldithiocarbamate were deposited by drop casting 250 μL of 0.2 M solution in chloroform onto a 1"×1" Mo-coated fused silica substrate and allowed to dry slowly by covering the substrate with an inverted funnel (Figure 4.2). This film was heated in air-free atmosphere from ambient to 550 °C at ramp rates ranging from 10 to 80 °C/min and annealed at 550 °C for 15 minutes. After annealing, the films were cooled to room temperature at the natural cooling rate of the holder that the substrates were placed on by turning off the heater.

Characterization Details: X-ray diffraction (XRD) patterns from the films were collected and recorded using a Bruker-AXS microdiffractometer equipped with a Cu-K_α X-ray source. A Bruker D8 Advance equipped with a Cu-K_α X-ray source was used to heat the thin films in-situ in XRD. Raman scattering from the films was collected using a Witec confocal Raman microscope. The films were excited using an Argon laser at 514.5 nm. The Raman scattered photons were collected and dispersed using a monochromator with an 1800 lines/mm grating. Scanning electron microscope (SEM) images were obtained using a JEOL 6500 field-emission gun microscope fitted with an energy dispersive x-ray (EDX) detector. Thermal analysis was carried out with a Pyris /Diamond TG-DTA 6300 (produced from Perkin-Elmer) analyzer with ~20 mg of sample heated at a rate of 10 °C/min.

5.3 Results and Discussion

Figure 5.1 a,b show the differential scanning calorimetric (DSC) and the thermogravimetric (TGA) curves, respectively, for copper diethyldithiocarbamate, zinc diethyldithiocarbamate, tin diethyldithiocarbamate, and tin dimethyldithiocarbamate. All the diethyldithiocarbamate complexes have the desirable property that they melt before they decompose. The melting temperatures for copper diethyldithiocarbamate, zinc

diethyldithiocarbamate, and tin diethyldithiocarbamate are 201, 183, and 170 °C, respectively, and they decompose at 305, 350, and 242°C, respectively. Because the complexes melt before they decompose and the ligands are all the same, a stoichiometric mixture of these three complexes is also expected to melt before decomposition and form a homogeneous liquid mixture. Figure 5.2 (b) shows the DSC and TGA curves for copper-zinc-tin diethyldithiocarbamate. We note that the metal stoichiometry of this complex (Cu:Zn:Sn= 2:1:1) is identical to that of CZTS and is identical to a 2:1:1 mixture of copper diethyldithiocarbamate, zinc diethyldithiocarbamate, and tin diethyldithiocarbamate. Copper-zinc-tin diethyldithiocarbamate melts at 151°C and decomposes at ~ 290 °C.

There are several advantages to depositing thin films using these complexes. First, a thin film deposited by decomposing a homogeneous liquid (melt) will likely be uniform in composition. Second, melting the complexes will relieve the stresses that develop during drying of the precursor thin film and eliminate the cracks that may have formed during drying. These advantages are especially useful for depositing thin films of multi-component materials such as CZTS. Precursor complexes can easily be applied onto substrates in their liquid state to deposit thin films using roll-to-roll techniques such as slot coating, and then further heat treated to decompose them to form CZTS films. Choice of the carbamate ligand is important. For example, tin dimethyldithiocarbamate is different from the three diethyldithiocarbamates because it does not melt before decomposition. Figure 5.1 shows that tin dimethyldithiocarbamate has a broad decomposition peak at ~ 300 °C. When using a mix of copper diethyldithiocarbamate, zinc diethyldithiocarbamate, and tin dimethyldithiocarbamate for thin film deposition, tin dimethyldithiocarbamate particles can act as stress relief and crack deflection centers in a melt of copper and zinc diethyldithiocarbamates.[19] In addition, as the solid and liquid media are in close contact with each other, there will be a rapid reaction between the two leading to the formation of a single phase of CZTS. As can be seen from the TGA plot for a stoichiometric mix of copper diethyldithiocarbamate, zinc diethyldithiocarbamate,

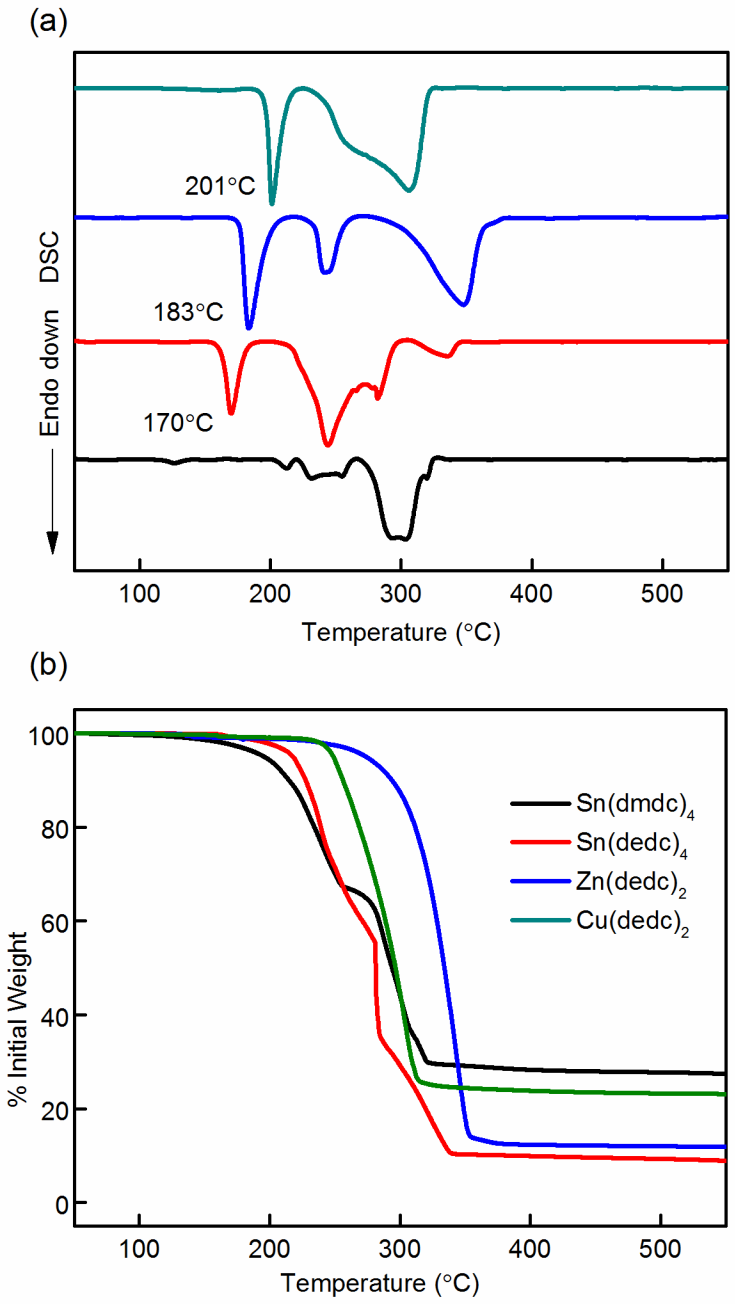

Figure 5.1 (a) DSC and (b) TGA curves for copper, zinc, and tin diethyl, and tin dimethyl dithiocarbamate complexes. The TGA and DSC data were acquired simultaneously by heating ~20 mg of the corresponding complex at 10 °C/min in nitrogen atmosphere. The endothermic processes give a downward peak in DSC.

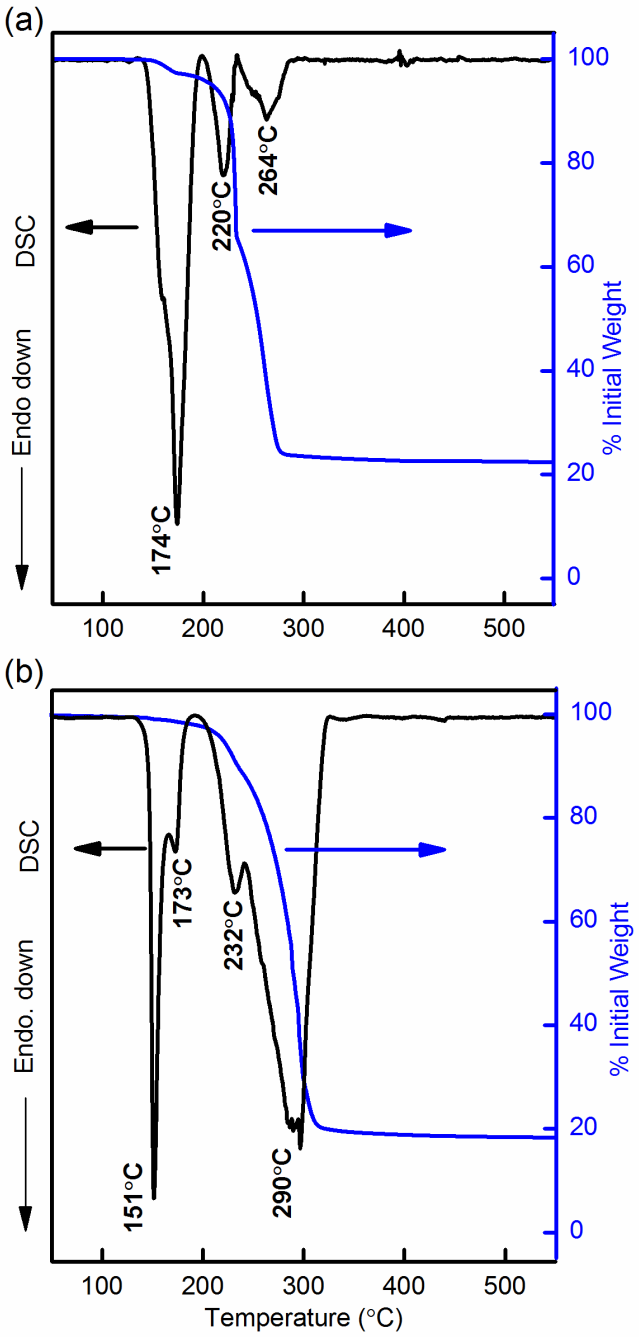

Figure 5.2 TGA and DSC curves for (a) stoichiometric mix of copper diethyldithiocarbamate, zinc diethyldithiocarbamate, and tin dimethyldithiocarbamate, and (b) copper-zinc-tin diethyldithiocarbamate. The TGA and DSC data were acquired simultaneously by heating ~20 mg of the corresponding complex at 10 °C/min in nitrogen atmosphere. The endothermic processes give a downward peak in DSC.

and tin dimethyldithiocarbamate [Figure 5.2 (a)], the reaction between the three complexes is completed at a temperature of ~270 °C after which the weight of the complex becomes constant.

To assess the possibility of depositing CZTS thin films directly from a mixture of copper diethyldithiocarbamate, zinc diethyldithiocarbamate, and tin dimethyldithiocarbamate complexes, a thin film cast from a stoichiometric (Cu:Zn:Sn= 2:1:1) mixture of these three complexes on Mo-coated fused silica substrate was heated *in situ* in an X-ray diffractometer in flowing nitrogen. At room temperature (RT), the XRD from the film of dried precursor complexes exhibits sharp diffraction peaks between 10° and 30° (Figure 5.3). These peaks are characteristic of dithiocarbamate complexes which crystallize upon drying. When this film was heated to 220° C, above the melting temperature (174^{o}C) of the complexes, the diffraction peaks between 10° and 30° disappeared and very faint and broad CZTS diffraction peaks begun to appear. As this film was heated further to 375 °C, the diffraction peaks for CZTS became more intense and sharper. However, SnS diffraction peak at 2θ~30° also appeared in the XRD pattern at 375 °C. Annealing this film at 375 °C for an additional 1.5 hour led to the disappearance of the SnS peak. After annealing, the intensity of all the CZTS XRD peaks decreased by ~15% which may be a consequence of sulfur loss from the film. Annealing the film at 375 °C for an additional hour did not change the XRD pattern significantly except for a further reduction in the intensity of the CZTS diffraction peaks by ~5%. The grain size calculated using the most intense CZTS diffraction peak at 2θ=28.5° was found to be 7 nm and did not change during annealing.

In the absence of excess sulfur, CZTS has been found to lose Sn in the form of SnS.[22] The phase separated SnS gets lost as vapors, thus leading to disappearance of the SnS XRD peak.[22] The appearance of SnS peak in the XRD on annealing the thin film at 375 °C and then its complete absence after annealing the film for an hour may indicative of the loss of Sn in the form of SnS vapors. However, Sn loss from CZTS has been found

to be most important at temperatures above 550 °C and may not be significant at such low temperatures.[22]

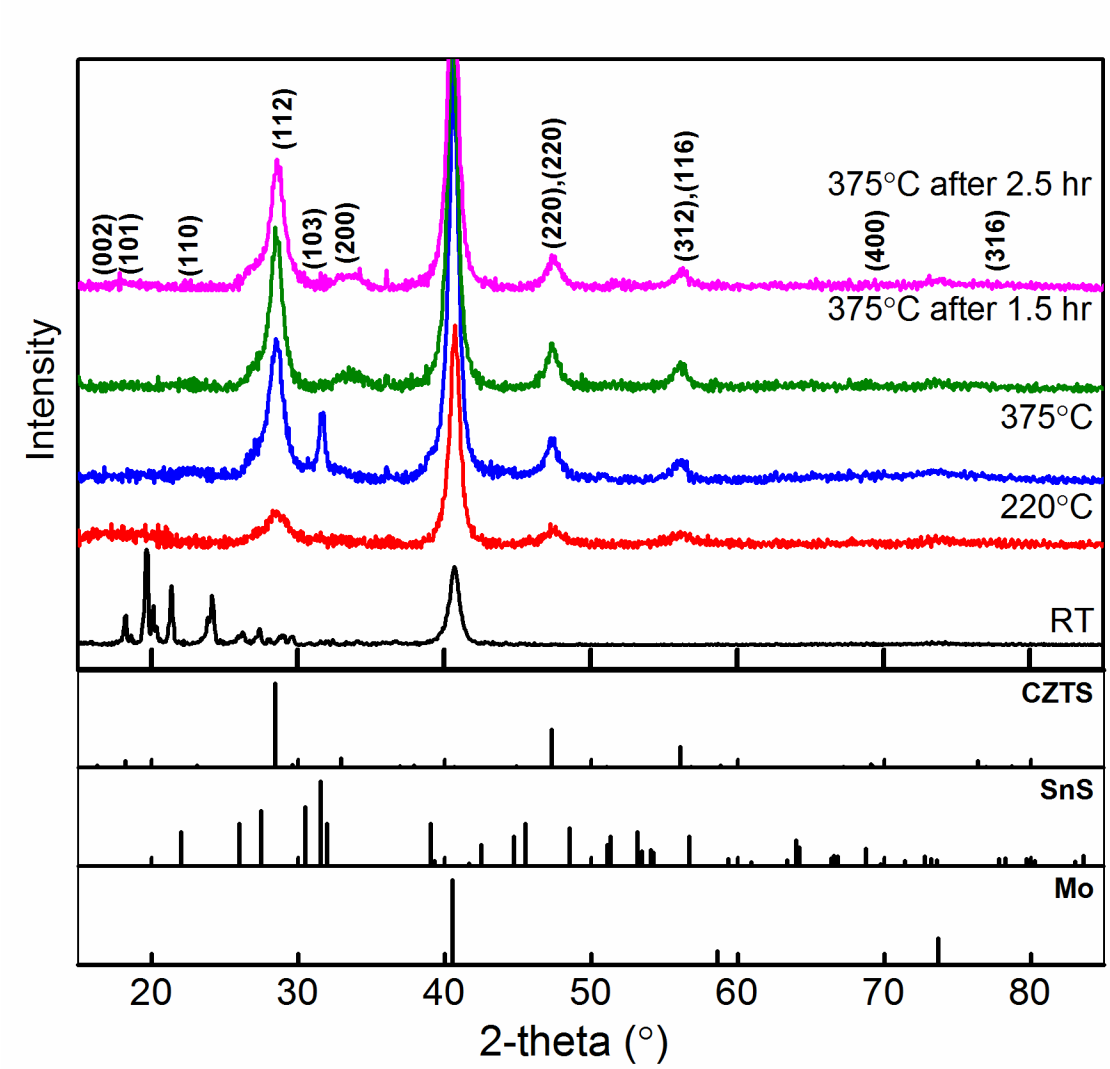

Figure 5.3 A study of the evolution of the XRD pattern as a stoichiometric mix of copper diethyldithiocarbamate, zinc diethyldithiocarbamate, and tin dimethyldithiocarbamate is heated in nitrogen. The room temperature XRD pattern has been scaled down by a factor of four for clarity.

Figure 5.4 shows SEM images of the thin film heated *in situ* in XRD before and after heating. The as-synthesized film from the complexes had a rough morphology showing crystalline faces. However, the film became smooth after heating due to melting

of the complexes. The annealed film is slightly cracked and looks porous with spheres of diameter ~100-250 nm making up the film (Figure 5.4(c)).

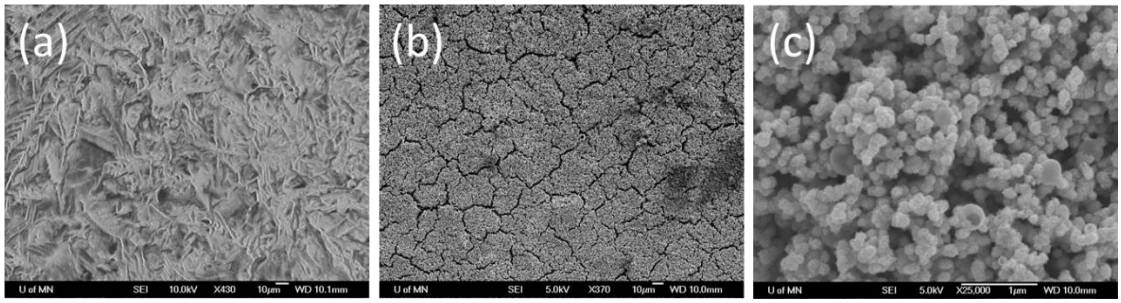

Figure 5.4 SEM images of a thin film from a stoichiometric mix of copper diethyldithiocarbamate, zinc diethyldithiocarbamate, and tin dimethyldithiocarbamate before (a) and after (b, c) annealing at 375 °C for 2.5 hr. The thin film is continuous, but microporous.

When the complexes are heated above their melting point, they all form a homogenous melt in which CZTS nuclei form by the decomposition of the dithiocarbamate complexes. Heating the complexes further would lead to growth of the nuclei and formation of the microspheres. The microspheres do not grow further on annealing as the amorphous carbon within the film from the decomposition of the dithiocarbamate complexes may be acting as pinning site to the growth CZTS grains. The weight of a stoichiometric mix of copper diethyldithiocarbamate, zinc diethyldithiocarbamate, and tin dimethyldithiocarbamate is 1682 g/mol which reduces to 439 g/mol upon conversion to CZTS. Taking the density of the dithiocarbamates to be 1.46 g/cm^3 and that of CZTS to be 4.55 g/cm^3, the volume of the film is reduced to about 8.5% of the initial volume upon the decomposition of the dithiocarbamates to CZTS. This huge loss in volume by the complex upon decomposition to CZTS might be contributing towards crack formation in the annealed film.

The thin film heating rate in the temperature range 150-270 °C (the precursor complexes decompose to give CZTS in this range) had an effect on the phase of the final film. The XRD pattern of the thin film heated at a rate of 0.5 °C/min from 150-270 °C (Figure 5.5) contains diffraction peaks for SnS_2 and Sn along with CZTS. The XRD pattern of the thin film heated at a rate of 5 °C/min does not show the diffraction peaks for Sn but only for SnS_2. Thin film heated at 30 °C/min over the same temperature range contained only phase-pure CZTS. In addition to getting a phase pure CZTS, the final grain size increased with the heating rate. The thin film heated at 0.5, 5, and 30 °C/min gave the final CZTS grain size of 5, 8.5, and 9.5 nm, respectively. The thin film heated *in situ* in XRD was heated at 12°C/min over the same temperature range; this XRD pattern for this film, too, did not show any additional peaks from phases apart from CZTS. Raman spectroscopy has been shown to be able to differentiate between CZTS, ZnS, and Cu_2SnS_3, which have a similar XRD patterns.[20] Raman spectrum from the thin film heated at 5 °C/min contained the scattering peaks for SnS_2 at 313 cm^{-1} and Cu_2S at 480 cm^{-1} (Figure 5.6), whereas the Raman spectrum from the thin film heated at a rate of 30 °C/min gave only the CZTS Raman scattering peak at ~331cm^{-1} with no peaks for ZnS or CTS.

The phase separation observed on heating the thin film slowly may be a consequence of the difference in the decomposition and melting temperatures of copper diethyldithiocarbamate, zinc diethyldithiocarbamate, and tin dimethyldithiocarbamate complexes. The three complexes do not decompose into sulfides at the same temperature as can be seen from their TGA and DSC plots. If the precursor films are heated at a slow rate, tin dimethyldithiocarbamate would begin to decompose first at lower temperatures giving rise to a SnS_2 phase. The formation of the CZTS phase would begin only after the temperature became high enough for the decomposition of copper diethyldithiocarbamate and zinc diethyldithiocarbamate. When the thin films are heated at high ramp rates, the substrate would very quickly reach a temperature that is high enough for the decomposition of all the three complexes, thus forming only a single phase of CZTS with no other impurity phases.

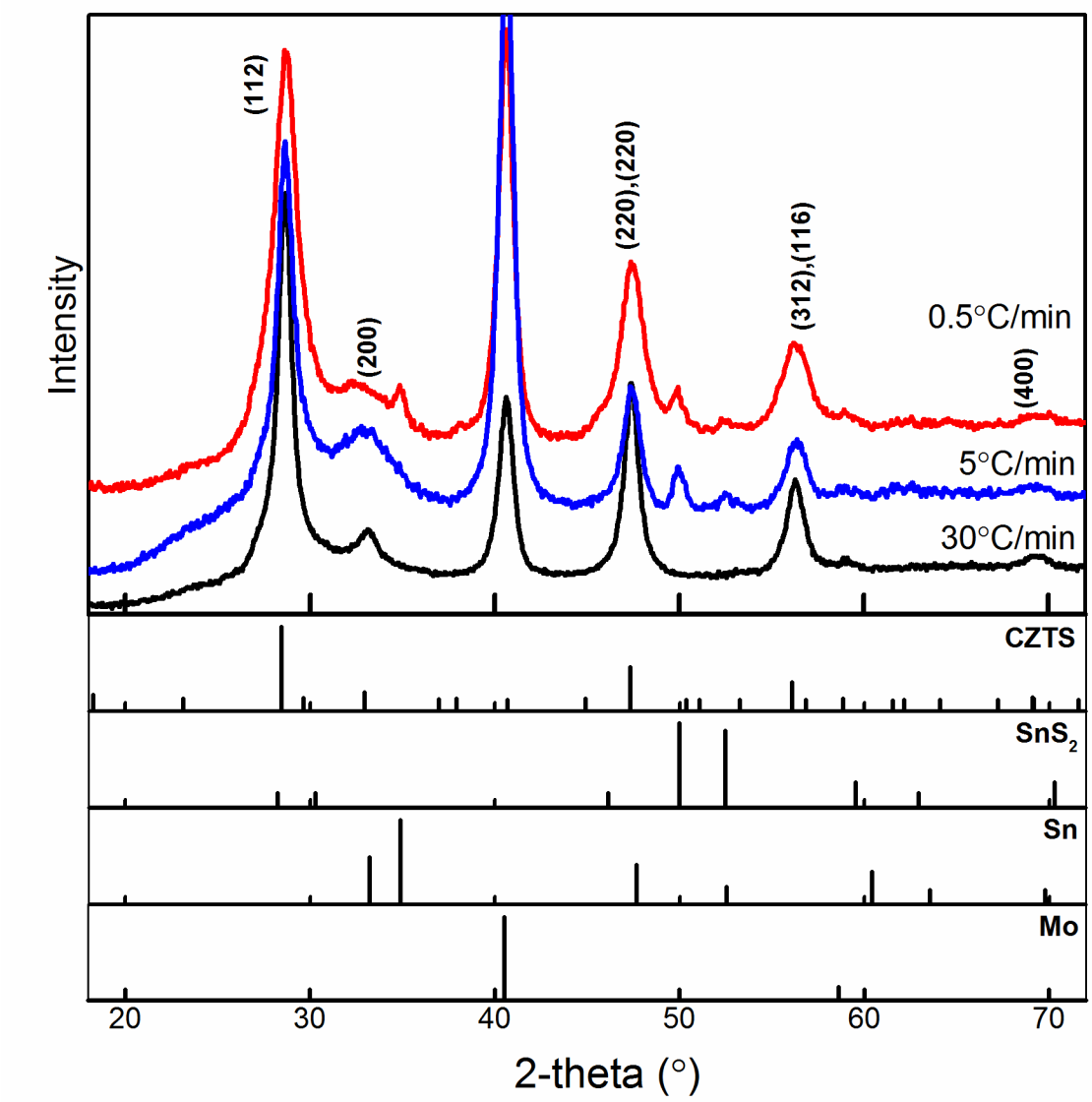

Figure 5.5 Effect of heating rate variation while heating films from a stoichiometric mix of copper diethyldithiocarbamate, zinc diethyldithiocarbamate, and tin dimethyldithiocarbamate complexes between 150 - 275 °C. A slow heating rate (0.5 °C/min) gave multiple phases, whereas a fast heating rate (30 °C/min) gave phase pure CZTS.

Oleylamine (OM) has been shown to be important in lowering the thermal decomposition temperature of dithiocarbamate complexes.[21] In order to study the effect of the addition of OM to CZTS thin film formation from dithiocarbamate complexes, a thin film from a mix of copper diethyldithiocarbamate, zinc diethyldithiocarbamate, and

tin dimethyldithiocarbamate complexes was heated *in situ* in XRD as before with the exception of adding OM to the precursor solution used for depositing the films. A ratio of OM:CZTS=10:1 was used (Figure 5.6). Addition of OM causes the CZTS grains to grow intensely with grain size reaching >60 nm at 375 °C as compared to the 7 nm grain size obtained for the thin film heated without OM. The annealed film also contains trace impurity of SnS as evidenced by the XRD pattern. On annealing the thin film at 375 °C for 1.5 hr., the intensity of the CZTS XRD peaks decreases by about 5%. Further annealing for an hour at 375 °C did not change either the diffraction peak intensity or the grain size.

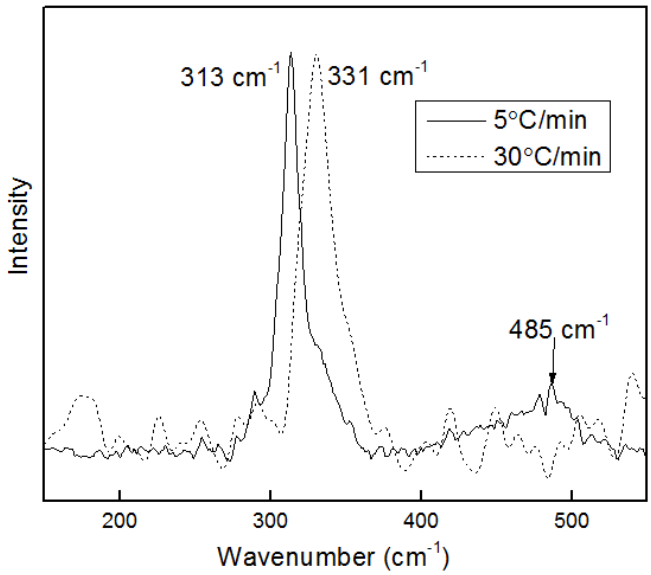

Figure 5.6 Raman spectra of thin films from a stoichiometric mix of copper diethyldithiocarbamate, zinc diethyldithiocarbamate, and tin dimethyldithiocarbamate heated at a ramp rate of 5 °C/min and 30 °C/min. The Raman spectrum for the thin film heated at the rate of 30 °C/min has been smoothened with an FFT filter to reduce the noise in the data.

In order to further understand the effect of OM addition, three different films with OM:CZTS=1:1, 5:1, and 10:1 were annealed at 375 °C with a heating rate of 1°C/min. The diffraction patterns obtained from the three different films are plotted in Figure 5.8. The addition of OM in the ratio OM:CZTS=1:1, 5:1, and 10:1 gave a CZTS grain size of

23 nm, 33 nm, and 17 nm, respectively. The OM addition to the precursor solution helps in increasing the grain size up to a ratio of OM:CZTS=5:1. This may be due to a reduction in the decomposition temperature of the complexes leading to a rapid growth of CZTS grains. A further increase in the amount of OM led to a decrease in the grain size, which may be due to the presence of excess carbon (due to OM decomposition) around the CZTS grains, hindering their growth. The addition of OM also increases the intensity of the secondary SnS phase formed along with CZTS. The XRD peaks for SnS phase are very weak in the case of OM:CZTS=1:1, but become quite intense for the case of OM:CZTS=10:1.

Figure 5.9 compares the XRD patterns for films with OM:CZTS=1:1 and 5:1 heated at two different heating rates of 1 and 30 °C/min. The CZTS grain size for OM:CZTS=1:1 and 5:1 at the heating rate of 30 °C/min are 9 and 67 nm, respectively, as opposed to 23 and 33 nm obtained using the heating rate of 1°C/min. The addition of only a little OM (OM:CZTS=1:1) did not change the XRD pattern for the thin film annealed at 30 °C/min. However, the thin film containing more OM (OM:CZTS=5:1) showed much greater grain growth. Change in grain size with the heating rate may be due to the interplay between nucleation and growth of CZTS which changes upon changing the way the thin film is heated through the region in which the complexes decompose.

Although OM was found to assist in the growth of CZTS grains, this came at the loss of microporosity and increased film cracking (Figure 5.10). This seems to suggest that adding OM may not be very advisable for synthesis of microporous films from CZTS. Table 5.1 gives a comparison of the stoichiometry of the various CZTS thin films heated at different ramp rates, with and without the addition of OM. Thin films deposited from complexes without the use of OM are generally Sn-rich and Zn-deficient. Copper diethyldithiocarbamate and zinc diethyldithiocarbamate melt before they decompose due to which they possess a high vapor pressure at elevated temperatures. In general, the greater the difference between the melting point and the decomposition temperature, the

more likely it is for the complex to evaporate before decomposition. This difference is 167°C and 104°C for zinc diethyldithiocarbamate and copper diethyldithiocarbamate,

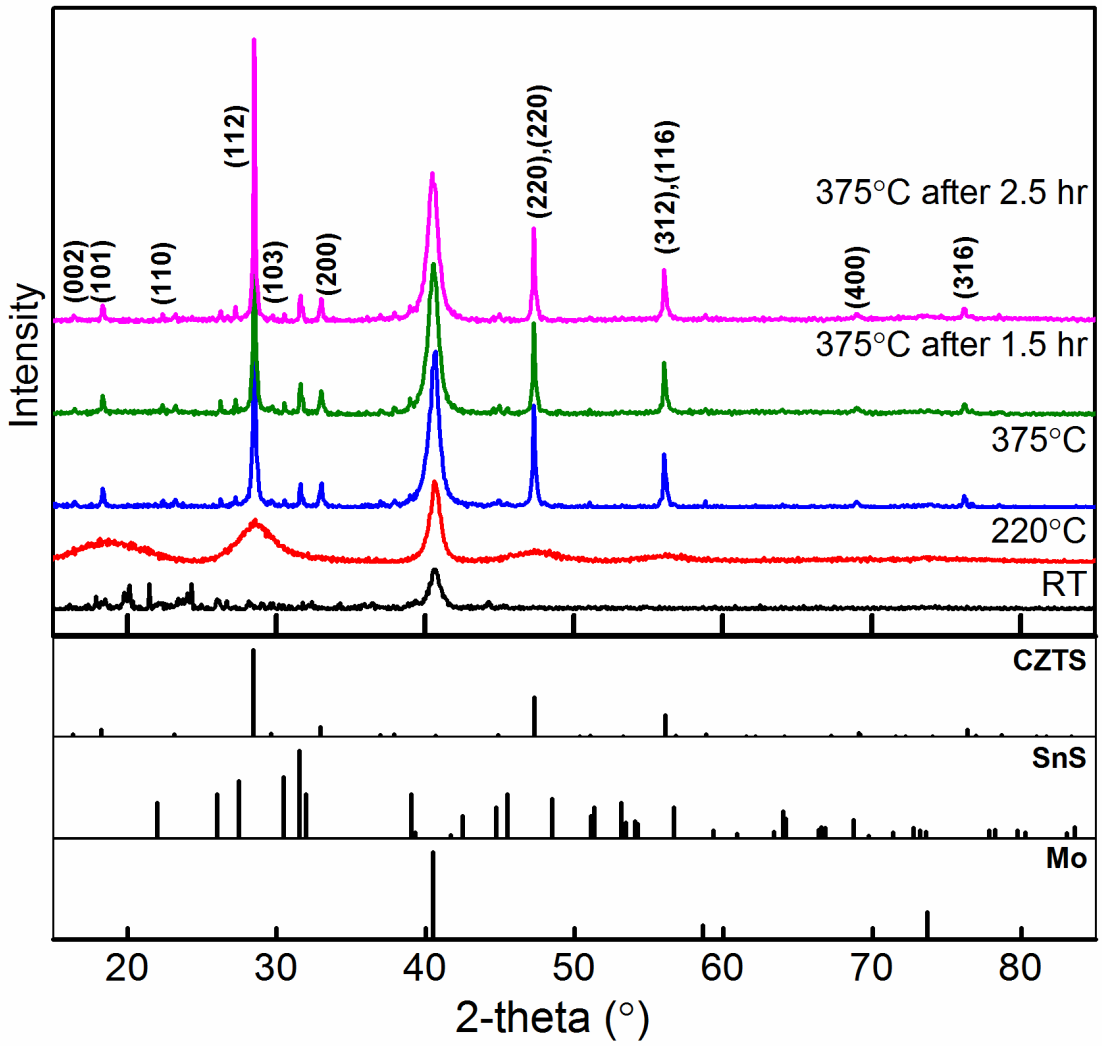

Figure 5.7 A study of the evolution of the XRD patterns as a stoichiometric mix of copper diethyldithiocarbamate, zinc diethyldithiocarbamate, and tin dimethyldithiocarbamate along with OM in the ratio OM:CZTS=10:1 is heated in nitrogen.

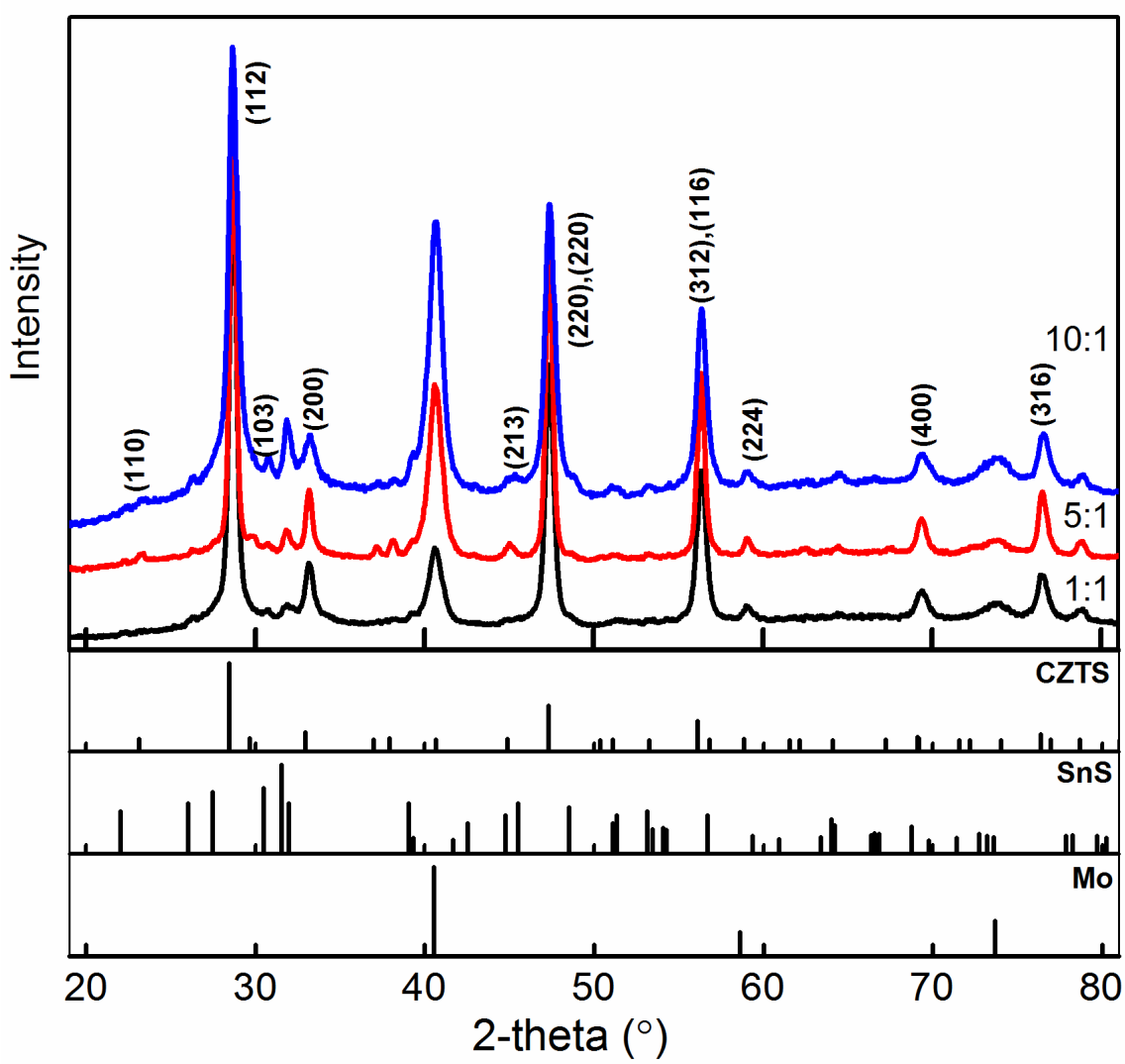

Figure 5.8 XRD patterns for thin films from a stoichiometric mix of copper diethyldithiocarbamate, zinc diethyldithiocarbamate, and tin dimethyldithiocarbamate with OM added in the ratio OM:CZTS as indicated on the individual diffraction patterns. The thin films were heated at a rate 1°C/min between 150 - 275 °C.

respectively, thereby indicating that zinc diethyldithiocarbamate will evaporate more than copper diethyldithiocarbamate. As tin dimethyldithiocarbamate does not melt before decomposition, it has a very low vapor pressure at elevated temperatures, thereby preventing its loss due to evaporation and leading to an excess Sn in the final film. Films

synthesized using OM with OM:CZTS=5:1 are closer to stoichiometric CZTS as compared to the other films; the presence of OM makes the complexes decompose at much lower temperatures, thereby minimizing their loss through evaporation. It is not possible to comment anything related to the amount of S in the annealed films, as the K_α peak for S overlaps with the L_α peak for Mo.

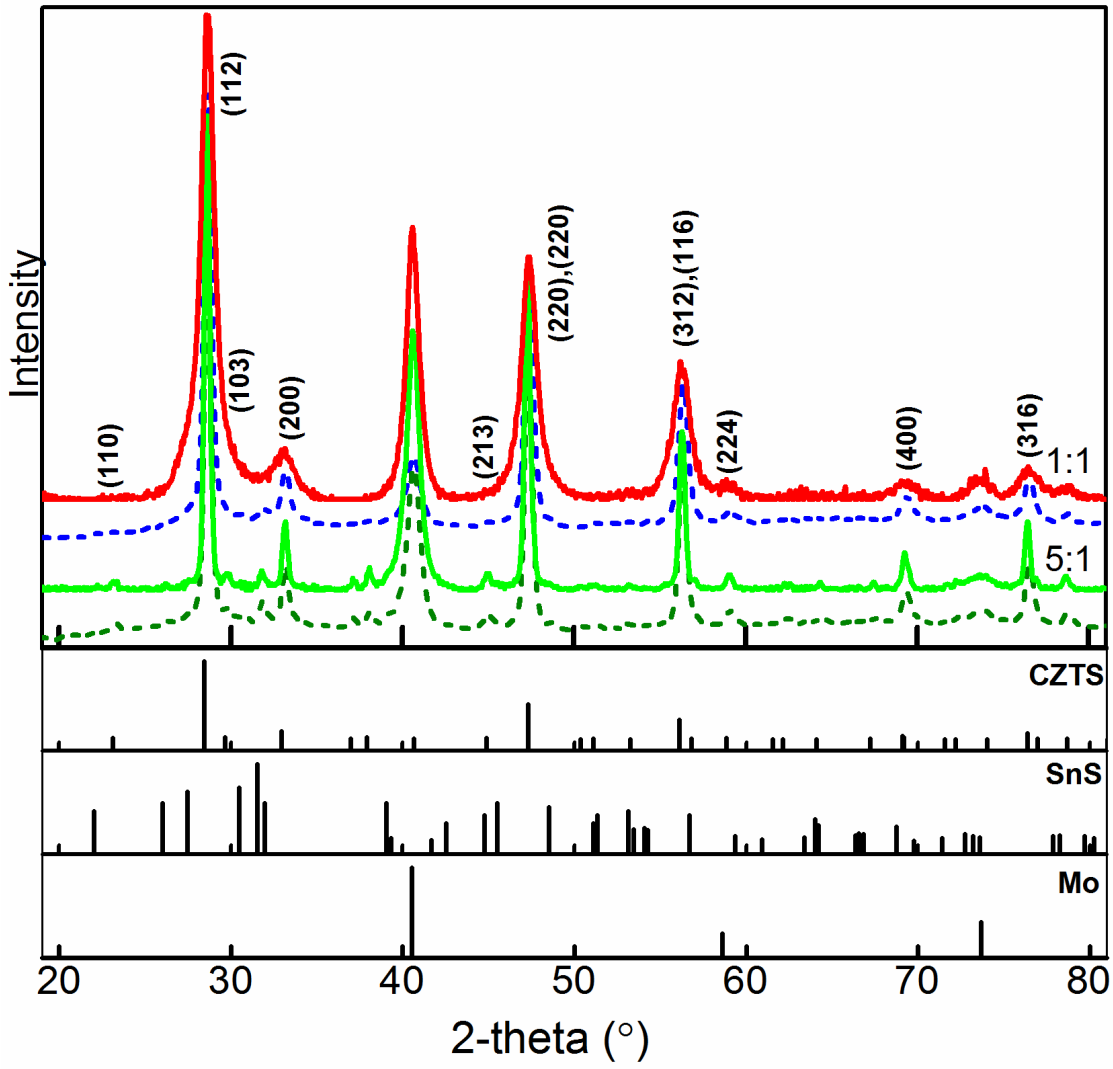

Figure 5.9 A comparison of the effect of heating rate variation on thin films from a stoichiometric mix of copper diethyldithiocarbamate, zinc diethyldithiocarbamate, and tin dimethyldithiocarbamate with OM:CZTS=1:1 and 5:1. Thin film with XRD patterns plotted using solid lines were heated at a rate of 30 °C/min, whereas those with XRD patterns plotted using dashed curves were heated at a rate of 1°C/min.

Table 5.1 Stoichiometry of CZTS thin films deposited from a mix of copper diethyldithiocarbamate, zinc diethyldithiocarbamate, and tin dimethyldithiocarbamate heated to 375 °C using various ramp rates as indicated. The stoichiometry, determined using EDX, is reported in atomic %.

Element	Original complex	OM 5:1 1°C/min	Plain 30 °C/min	Plain 12°C/min	Plain 1°C/min
Cu	8.07	32.51	21.96	29.63	29.39
Zn	6.45	10.82	2.63	8.88	8.72
Sn	5.95	14.32	23.93	25.97	26.09
S	79.53	42.35	51.48	35.53	35.80

In order to better control the stoichiometry of the annealed films, thin films were deposited from copper-zinc-tin diethyldithiocarbamate. Here, it may be easier to control the stoichiometry as all the three diethyldithiocarbamates melt before decomposition. For exploring the effect of the heating rate on the morphology and stoichiometry of the annealed films, films from copper-zinc-tin diethyldithiocarbamate were heated to a temperature of 550 °C at ramp rates of 10, 40, and 80 °C/min and annealed at that temperature for 15 minutes. The XRD patterns for all the thin films are plotted in Figure 5.11. All the different annealed films were predominately CZTS and exhibit intense grain growth due to the use of higher annealing temperature.

There are several similarities between the films from tin dimethyldithiocarbamate and tin diethyldithiocarbamate. First, thin films from thermal decomposition of copper-zinc-tin diethyldithiocarbamate, except for the one heated at 10 °C/min, also have a minor phase of SnS. The thin film heated at 10 °C/min only had SnO_2, but no SnS. The second similarity is in the increase in grain size with the heating rate. The thin film heated at a rate of 10 °C/min had a grain size of 35 nm. The thin films heated with a higher heating rate had a grain size greater than 60 nm which could not be resolved with the instrument. Another similarity is that the diffraction peaks for the impurity phase (SnS) became more intense with a faster heating rate.

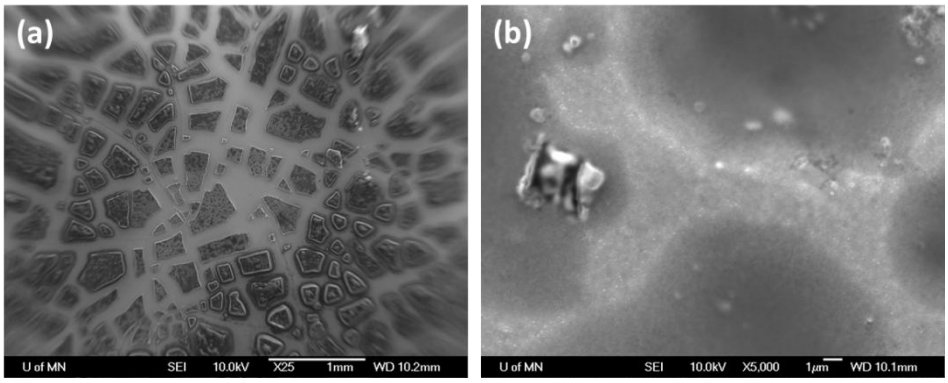

Figure 5.10 SEM images of thin films from a stoichiometric mix of copper diethyldithiocarbamate, zinc diethyldithiocarbamate, and tin dimethyldithiocarbamate containing OM:CZTS=5:1 heated at 1°C/min.

Figure 5.12 shows the SEM images for the thin films heated at different ramp rates. All the thin films have a microporous structure, with a sphere size of about 1μm. However, the thin films heated with a ramp rate of 40 and 80 °C/min had small grains ~100 nm in diameter decorating the microspheres. XRD results tend to indicate that these grains may be SnS.

Figure 5.13 shows a generic Raman spectrum from films annealed at 550 °C. All the annealed films had their most intense Raman scattering peak between 334-338 cm^{-1} which is close to that accepted for phase-pure CZTS. Table 5.2 gives a compilation of the stoichiometry of the annealed films obtained using EDX. Annealed films were predominately copper-rich and zinc-poor. The amount of copper in the film increases with the heating rate. Thin films heated with a ramp rate of 10 °C/min would lose Cu and Zn by evaporation of the complexes at low temperatures before the corresponding complexes decomposed, and lose Sn and Zn at elevated temperatures due to the relatively high vapor pressure of SnS and Zn at elevated temperatures.[22,23] For thin films annealed at higher ramp rates, Zn and Sn would continue to be lost at elevated temperatures but Cu-loss would be minimized, thereby giving Cu rich films.

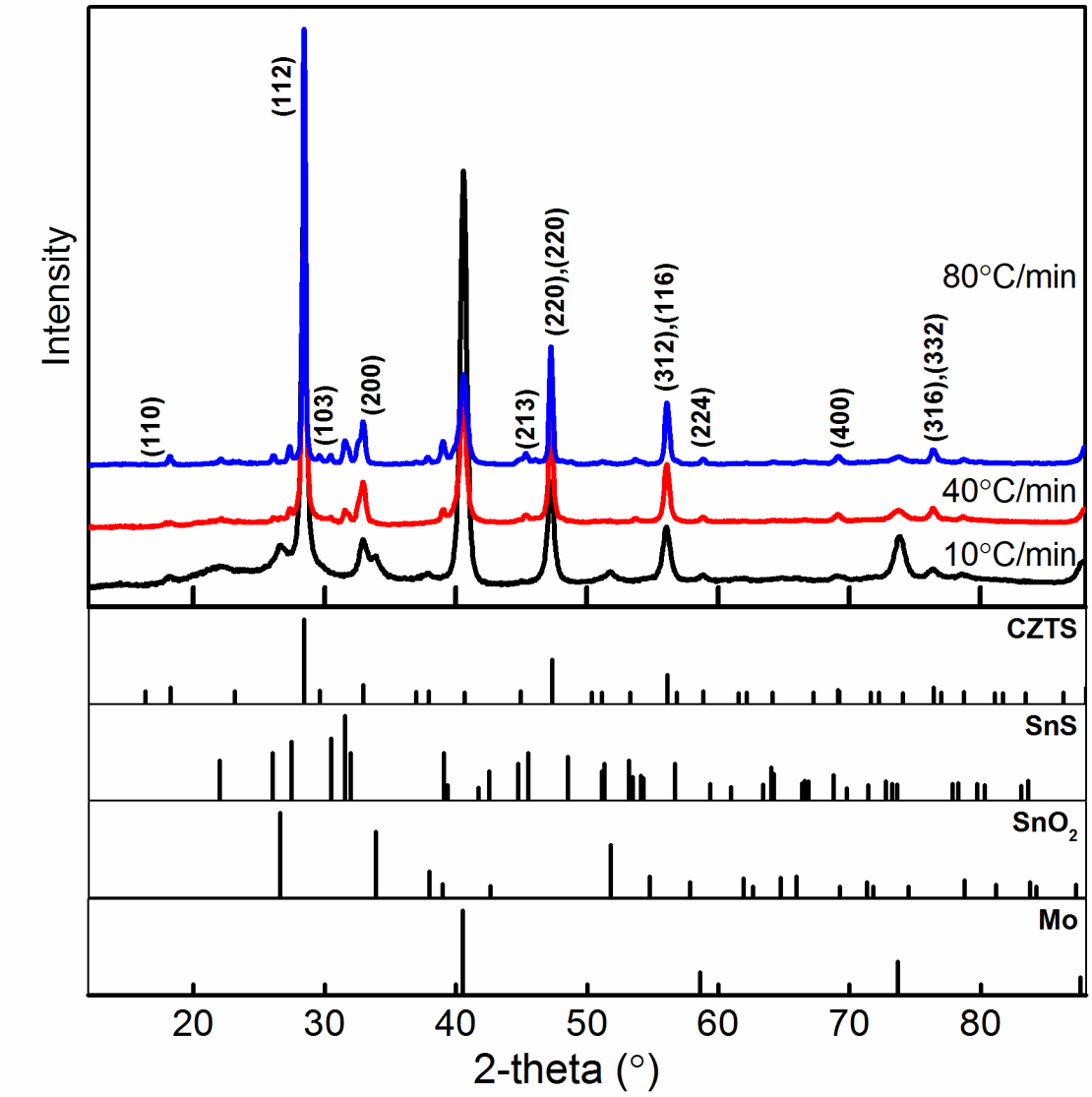

Figure 5.11 XRD patterns for thin films from the copper-zinc-tin diethyldithiocarbamate complex heated to 550 °C using different ramp rates as indicated.

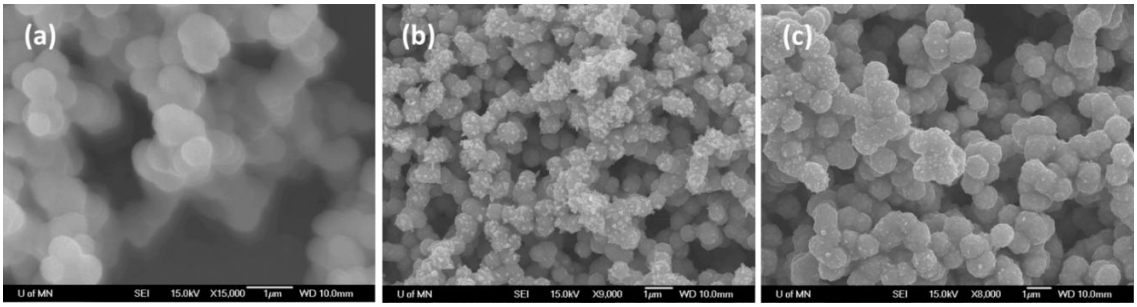

Figure 5.12 SEM images of CZTS thin films from the copper-zinc-tin diethyldithiocarbamate complex heated to 550 °C using ramp rates of (a) 10 °C/min, (b) 40 °C/min, and (c) 80 °C/min.

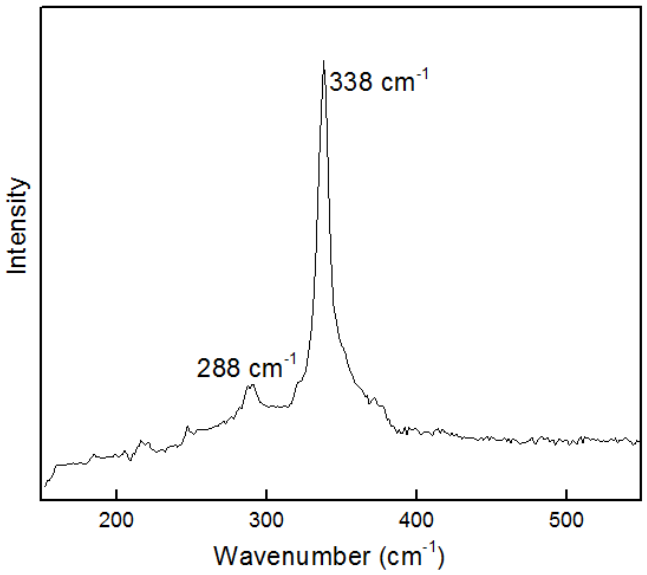

Figure 5.13 Representative Raman spectra of CZTS thin films from the copper-zinc-tin diethyldithiocarbamate complex.

Table 5.2 Stoichiometry of CZTS thin films obtained from the copper-zinc-tin diethyldithiocarbamate complex heated to 550 °C using various ramp rates as indicated. The stoichiometry, determined using EDX, is reported in atomic %.

Element	Precursor	10 °C/min	40 °C/min	80 °C/min
Cu	9.48	20.84	31.89	38.07
Zn	5.86	6.78	5.18	9.54
Sn	3.56	15.65	15.12	11.91
S	81.10	56.73	47.82	40.49

5.4 Conclusion

In conclusion, we present a facile synthesis of CZTS microporous films from thermal decomposition of metal dithiocarbamate complexes. Films from decomposition of metal dithiocarbamate complexes were found to be predominately CZTS with trace impurities of SnS or SnO_2. These films were found to be smooth and composed of microspheres, with the diameter of the microspheres increasing from ~100-250 nm for films annealed at 375 °C to ~1μm for 550 °C annealed films. The Raman spectra for the annealed films matched CZTS. The influence of a variation in heating rate and addition of OM to the morphology and stoichiometry of the final film was studied. OM addition was found to increase the grain size significantly due to lowering of the decomposition temperature of the complexes. The increase in grain size achieved by OM addition was, however, detrimental to the microporosity of the synthesized film. The rate of heating the complexes was found to influence the grain size and the stoichiometry of the final film.

5.5 References

1 C. A. Wolden, J. Kurtin, J. B. Baxter, I. Repins, S. E. Shaheen, J. T. Torvik, A. A. Rockett, V. M. Fthenakis, and E. S. Aydil, J. Vac. Sci. Technol. A **29**, 030801 (2011).

2 D. B. Mitzi, O. Gunawan, T. K. Todorov, K. Wang, and S. Guha, Sol. Energy Mater. Sol. Cells **95**, 1421 (2011).
3 H. Katagiri, K. Jimbo, W. S. Maw, K. Oishi, M. Yamazaki, H. Araki, and A. Takeuchi, Thin Solid Films **517**, 2455 (2009).
4 W. Shockley, and H. J. Queisser, J. Appl. Phys. **32**, 510 (1961).
5 D. A. R. Barkhouse, O. Gunawan, T. Gokmen, T. K. Todorov, and D. B. Mitzi, Prog. Photovolt: Res. Appl. **20**, 6 (2012).
6 G. Ma, T. Minegishi, D. Yokoyama, J. Kubota, and K. Domen, Chem. Phys. Lett. **501**, 619 (2011).
7 K. Wang, O. Gunawan, T. Todorov, B. Shin, S. J. Chey, N. A. Bojarczuk, D. Mitzi, and S. Guha, Appl. Phys. Lett. **97**, 143508 (2010).
8 K. Jimbo, R. Kimura, T. Kamimura, S. Yamada, W. S. Maw, H. Araki, K. Oishi, and H. Katagiri, Thin Solid Films **515**, 5997 (2007).
9 H. Araki, A. Mikaduki, Y. Kubo, T. Sato, K. Jimbo, W. S. Maw, H. Katagiri, M. Yamazaki, K. Oishi, and A. Takeuchi, Thin Solid Films **517**, 1457 (2008).
10 K. Ramasamy, M. A. Malik, and P. O'Brien, Chem. Sci. **2**, (2011).
11 K. Moriya, K. Tanaka, and H. Uchiki, Jpn. J. Appl. Phys. **46**, 5780 (2007).
12 Y. Wang, and H. Gong, J. Electrochem. Soc. **158**, H800 (2011).
13 A. Ennaoui, M. Lux-Steiner, A. Weber, D. Abou-Ras, I. Kötschau, H. Schock, R. Schurr, A. Hölzing, S. Jost, R. Hock, T. Voß, J. Schulze, and A. Kirbs, Thin Solid Films **517**, 2511 (2009).
14 W. Ki, and H. W. Hillhouse, Adv. Energy Mater. **1**, 732 (2011).
15 Q. Guo, H. W. Hillhouse, and R. Agrawal, J. Am. Chem. Soc. **131**, 11672 (2009).
16 Q. Guo, G. M. Ford, W. Yang, B. C. Walker, E. A. Stach, H. W. Hillhouse, and R. Agrawal, J. Am. Chem. Soc. **132**, 17384 (2010).
17 C. Steinhagen, M. G. Panthani, V. Akhavan, B. Goodfellow, B. Koo, and B. A. Korgel, J. Am. Chem. Soc. **131**, 12554 (2009).
18 A. Khare, A. W. Wills, L. M. Ammerman, D. J. Norris, and E. S. Aydil, Chem. Commun. **47**, 11721 (2011).
19 T. K. Todorov, K. B. Reuter, and D. B. Mitzi, Adv. Mater. **22**, E156 (2010).
20 A. J. Cheng, M. Manno, A. Khare, C. Leighton, S. A. Campbell, and E. S. Aydil, J. Vac. Sci. Technol. A **29**, 051203 (2011).
21 Y. K. Jung, J. I. Kim, and J. K. Lee, J. Am. Chem. Soc. **132**, 178 (2010).
22 A. Weber, R. Mainz, and H. W. Schock, J. Appl. Phys. **107**, 013516 (2010).
23 A. Weber, H. Krauth, S. Perlt, B. Schubert, I. Koetschau, S. Schorr, and H. W. Schock, Thin Solid Films **517**, 2524 (2009).

Chapter 6

Calculation of The Lattice Dynamics And Raman Spectra of Copper Zinc Tin Chalcogenides And Comparison to Experiments

In this chapter, the electronic structure, lattice dynamics, and Raman spectra of the kesterite, stannite, and pre-mixed Cu-Au structures (PMCA) of Cu_2ZnSnS_4 (CZTS) and $Cu_2ZnSnSe_4$ (CZTSe) were calculated using density functional theory. Differences in longitudinal and transverse optical (LO-TO) splitting in kesterite, stannite, and PMCA structures can be used to differentiate them. The Γ-point phonon frequencies, which give rise to Raman scattering, exhibit small but measurable shifts, for these three structures. Experimentally measured Raman scattering from CZTS and CZTSe thin films were examined in light of DFT calculations and deconvoluted to explain subtle shifts and asymmetric line shapes often observed in CZTS and CZTSe Raman spectra. Raman spectroscopy in conjunction with *ab initio* calculations can be used to differentiate between kesterite, stannite, and PMCA structures of CZTS and CZTSe.

6.1 Introduction

Copper zinc tin sulfide (Cu_2ZnSnS_4, CZTS), copper zinc tin selenide ($Cu_2ZnSnSe_4$, CZTSe), and their alloys ($Cu_2ZnSnS_{4(1-x)}Se_{4x}$ where $0 \leq x \leq 1$, CZTSSe), are emerging as important light absorbers for next-generation thin-film solar cells[1-4] because they are made of abundant and nontoxic elements. CZTS and CZTSe band gaps are 1.45 and 1 eV, respectively, and their alloys cover the optimal energy range for solar energy conversion.[5] Both CZTS and CZTSe have high absorption coefficients ($>10^4$ cm^{-1})[3,6,7,8] in the visible range of the electromagnetic spectrum and only a few micron thick films can absorb all the radiation above the band gap. CZTS thin films have been synthesized using

co-evaporation,[9] co-sputtering,[10] chemical bath deposition,[11] electrodeposition,[12] spray pyrolysis,[13] sulfidation of copper-zinc-tin film stacks,[14] pulsed-laser deposition,[15] spin coating from precursor solutions,[16] and casting from nanocrystal dispersions.[7,17,18] Recently, CZTSSe solar cells have been shown to achieve a power conversion efficiency of 10.1%.[19]

CZTS and CZTSe can crystallize in kesterite (KS; space group $I\bar{4}$; no. 82), stannite (ST; space group $I\bar{4}2m$; no. 121), or primitive mixed Cu-Au (PMCA; space group $P\bar{4}2m$; no. 111) crystal structures (Figure 6.1).[20] KS and ST structures are body-centered tetragonal with c ≈ 2a (*e.g.*, pseudocubic) and may be thought of as two sulfur face-centered cubic (FCC) lattices stacked on top of each other with Cu, Zn, and Sn occupying half the tetrahedral voids within this FCC lattice. The PMCA structure is primitive tetragonal with c≈a; two unit cells are shown in Figure 6.1 for comparison with the KS and ST structures. The differences in the arrangement and stacking of the metal cations within the tetrahedral voids gives rise to these three different structures. Specifically, the KS structure consists of two alternating cation layers each containing Cu and Zn or Cu and Sn, whereas in the ST and PMCA structures a layer of Cu alternates with a layer of Zn and Sn. In the ST structure, the Zn and Sn atoms on the same layer switch their positions every other layer. This location swapping between Zn and Sn, every other layer, is absent in PMCA, which makes it primitive tetragonal and distinguishes it from the ST structure. Moreover, zinc blende ZnS or ZnSe and Cu_3SnS_4 (CTS) or Cu_3SnS_4 (CTSe) result when only Zn or only Cu and Sn atoms are used in filling half of the tetrahedral voids. In all these structures, the sulfur (or selenium) FCC sublattice determines the unit cell dimensions and the X-ray diffraction is not sensitive to the metal cation arrangement. As a result, within experimental broadening of the diffraction peaks, it is a challenge to differentiate between KS, ST, and PMCA structures using X-ray diffraction. Similarly, it is difficult to distinguish between CZTS, ZnS, and CTS (or CZTSe, ZnSe, and CTSe).

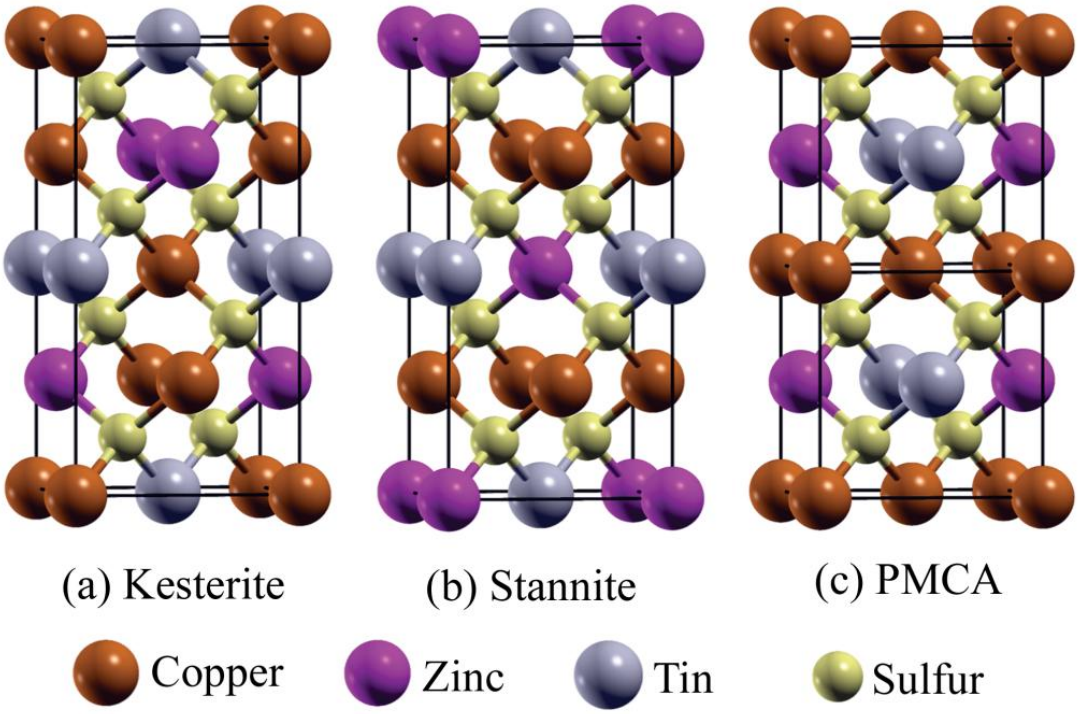

Figure 6.1 Kesterite, stannite, and PMCA structures for CZTS. CZTSe structures are obtained by replacing S with Se atoms.

Density functional theory (DFT) calculations (using the relativistic FPLAPW method and the generalized gradient approximation for the exchange-correlation functional) on CZTS and CZTSe indicate that the band gaps and electron affinities of the KS, ST, and PMCA structures can differ by as much as 0.15 eV.[21] As a result, the power conversion efficiency of a solar cell made from a CZTS or a CZTSe film containing a mixture of these three crystal structures may be limited because of charge-carrier trapping in domains where the electron or hole energies are lowest. These calculations suggest that a high-efficiency solar cell should contain only a single CZTS (or CZTSe) phase. Unfortunately, the similarity of the crystal structures and constituent elements (*e.g.*, Cu and Zn) makes identification of the phases present in CZTS or CZTSe films difficult. Although neutron diffraction can be used to differentiate between the three CZTS

structures,[22] a more accessible technique would be preferable. Raman spectroscopy has been shown to be an effective tool to distinguish CZTS, Cu_3SnS_4 (CTS), and ZnS.[23, 24] However, to date no such easily accessible experimental characterization tool exists to differentiate between KS, ST, and PMCA structures.

Recently, several electronic structure calculations for CZTS and CZTSe have been published.[20,21,25-29] The stability of the three crystal structures and the energetics of defect formation have also been studied through density functional theory (DFT).[25,27,30] Amiri *et al.* and Gurel *et al.* discussed the lattice dynamics in CZTS and CZTSe.[28,31] However, they did not address the possibility of differentiating between the KS, ST, and PMCA structures based on their results. Phonon dispersion in solids is sensitive to the coupling between the atoms within the lattice. Thus, variations in phonon dispersion in KS, ST, and PMCA structures may help distinguish these structures. To measure this dispersion, either neutron diffraction or Raman spectroscopy can be utilized. Specifically, Raman scattering is observed at frequencies corresponding to the phonon modes at the Γ point. Moreover, Raman spectroscopy is a convenient and widely available technique. Herein, we calculate the Raman spectra of KS, ST, and PMCA structures of CZTS and CZTSe using *ab initio* methods and examine Raman spectra collected from CZTS and CZTSe films in light of these calculations.

6.2 Computational Details

The lattice dynamics of KS, ST, and PMCA structures of CZTS and CZTSe were calculated using DFT[32,33,34] within the plane-wave - pseudopotential implementation of the PWscf code contained in the QUANTUM ESPRESSO (QE) package.[35] The Perdew-Burke-Ernzerhof (PBE) flavor[36] of the generalized gradient approximation (GGA) was used to model the exchange-correlation functional. Ultrasoft Vanderbilt pseudopotentials were employed to model the interaction of electrons with ionic cores. The electronic wave functions and charge density were expanded on plane-wave basis sets up to kinetic

energy cutoffs of 60 and 600 Ry, respectively. Brillouin-zone integration was performed using a Γ-point-centered 6×6×3 Monkhorst-Pack[37] k-point mesh. With this choice of computational parameters the error on total energies and atomic forces is estimated to be less than 10^{-4} Ry/atom and 10^{-5} Ry/bohr, respectively. Prior to phonon dispersion calculations, both the unit cell and the atomic positions were relaxed to obtain the equilibrium of each crystal structure. The structural optimizations were considered converged when total energy decreased by less than 10^{-5} Ry/unit cell and atomic forces were smaller than 10^{-4} Ry/au. The vibrational frequencies and modes of the considered crystals were calculated using density functional perturbation theory (DFPT) as implemented in the PHONON code of the QE package. In the calculation of phonon dispersions, a 4×4×4 grid was used to integrate over the vibrational Brillouin zone. The results presented in this chapter were tested (and found robust) against finer k-point grids. The integration over the Brillouin zone for the phonon degrees of freedom was needed to obtain the vibrational density of states.

6.3 Experimental Details

Thin CZTS films (~1.5 μm) were formed by melting nanocrystal films that were drop casted from colloidal dispersions of CZTS nanocrystals (3 mg/ml) on molybdenum-coated glass substrates. The CZTS nanocrystals were 2 nm in diameter and were prepared as described in Ref. 38. As-synthesized nanocrystals are surrounded by oleic acid and oleylamine ligands that stabilize the nanocrystal dispersions in organic solvents such as toluene. These ligands were removed from the films before the thermal treatment that formed the final CZTS films. Specifically, after drop casting, the dried films were treated with pyridine for 60 seconds to exchange the oleic acid and oleylamine ligands. The pyridine ligands were then desorbed from the nanocrystal surfaces by heating the substrate to 200 °C for 1 min in air. The substrate was then annealed at 550 °C in an air-free Ar atmosphere for approximately 5 minutes for grain growth.

Thin CZTSe films (300 nm) were prepared by reactive co-evaporation from Cu, Zn, Sn, and Se in a high vacuum molecular beam epitaxy system onto molybdenum-coated glass substrates at 400 °C. The stoichiometry of these films was measured by energy dispersive X-ray spectroscopy and was consistent with CZTS and CZTSe films, respectively. X-ray diffraction (XRD) from these films was also consistent with CZTS and CZTSe and did not show any other impurity phases (*e.g.*, CuS, Cu_2S, SnS_2, Cu_3SnS_4, $Cu_2Sn_3S_7$, *etc.*, and their Se analogs). However, it is well known that XRD cannot rule out the presence of cubic ZnS and pseudocubic Cu_2SnS_3 (ZnSe and pseudocubic Cu_2SnSe_3), which have unit-cell dimensions virtually identical to CZTS (CZTSe).[23,24] However, any significant presence of these phases in our films is ruled out based on their Raman spectra. Raman spectra were collected using a Witec alpha300 R confocal Raman microscope equipped with an Argon ion laser (514.5 nm), UHTS300 spectrometer, DV401 CCD detector, and a monochromator with an 1800 lines/mm grating.

6.4 Results and Discussion

Table 6.1 summarizes the calculated lattice parameters for the three CZTS and CZTSe crystal structures and compares them to experimentally determined parameters from the literature. The relaxed lattice parameters are within 1% of experiment with c/a nearly 2. A comparison of the total energy of the three structures indicates that the KS structure is the most stable amongst the three followed by ST and PMCA, in agreement with previous calculations.[20,21] Based on these results, it is usually presumed that the CZTS films made in the laboratory are in the KS structure. However, the energy difference between the KS and ST structures is 5 meV/atom and it is more reasonable to presume that KS and ST structures will coexist in any polycrystalline film that is synthesized or annealed at elevated temperatures. Simulated XRD patterns for the three structures of CZTS and CZTSe using relaxed lattice parameters are shown in Figures 6.2 and 6.3, respectively. The XRD patterns were obtained using CrystalMaker® software.

The XRD simulations reiterate that it is extremely difficult to differentiate between the three structures of CZTS and CZTSe simply based on XRD patterns.

Figure 6.4 shows the atom-resolved density of states (DOS) for CZTS and CZTSe for the three different crystal structures while Table 6.1 summarizes their calculated band gaps. As expected, the DFT calculations underestimate the absolute values of the band gap energies by 0.3-0.4 eV[39] but the trends in changes with Se substitution and crystal structure are similar to the previous computational studies.[20,21] Although the electronic properties for the KS and ST structures of CZTS and CZTSe have already been studied in detail, the PMCA structure has been neglected. In all of the structures, for both CZTS and CZTSe, the valence band DOS is composed of hybridized Cu-d and anion-p states along with contributions from Zn-s, Zn-p, Sn-p, and Cu-s between -2 to -6 eV. The conduction band consists primarily of Sn-s, Zn-s, and anion-p states near the band edge along with contributions from the other metal cations at higher energy states.

Figure 6.5 shows the phonon dispersions for CZTS KS, ST, and PMCA structures through the high symmetry points (Z-Γ-X-P-Γ-N). The LO-TO splitting, due to the ionic character of the considered crystals, is accounted for by the precise evaluation of the dielectric constant and of the Born effective charges that allow for the calculation of the non-analytical part of the dynamical matrix.[40] At first glance, the phonon dispersion curves for KS, ST, and PMCA CZTS look qualitatively similar. However, on close examination, one can find distinguishing features that can help differentiate between the three structures based on the phonon dispersion curves. For example, the PMCA structure can be distinguished from the KS and ST structures based on certain distinguishing features near the Γ point. Specifically, the phonon dispersion curves at about 365 cm^{-1} along the Z-Γ-X line for both KS and ST show a discontinuity, which is absent for PMCA. This discontinuity is due to a difference in the magnitude of LO-TO splitting along the Z-Γ and Γ-X directions for KS and ST, causing the phonon branches in the two directions to be separated in energy. The phonon dispersion curve for PMCA does not exhibit this discontinuity as the phonon branches in these two directions for PMCA have

the same energy. Furthermore, to distinguish KS from ST, one can probe the phonon dispersion along the Z-Γ-X line at frequencies corresponding to 165 and 150 cm^{-1}. The ST phonon dispersion curve crossing the Γ point at 165 cm^{-1} splits into two branches as one moves along the Γ-Z direction. This splitting is absent for the phonon dispersion curve crossing the Γ point at 148 cm^{-1}. This situation is reversed in the case of KS. The KS phonon branch crossing the Γ point at 145 cm^{-1} will split as one moves away from the Γ point but this splitting is absent for the phonon dispersion curve crossing the Γ point at 165 cm^{-1}. These differences may help identify the crystal structure of CZTS prepared using different methods and under different synthesis conditions.

Table 6.1 Calculated equilibrium lattice parameters for CZTS and CZTSe KS, ST, and PMCA structures. E_{diff} is the energy difference (meV/atom) between the given structure and the KS structure of the corresponding material. E_g is the band gap of the material.

Material	a (Å)	c (Å)	c/a	E_g (eV)	E_{diff} (meV/atom)
CZTS Kesterite (sim)	5.443	10.786	1.982	0.87	0.000
CZTS Stannite (sim)	5.403	10.932	2.023	0.68	4.625
CZTS PMCA (sim)	5.400	10.942	2.026	0.65	8.320
CZTS Kesterite (exp)	5.432[a]	10.840[a]	1.996[a]	1.5[b]	-
CZTS Stannite (exp)	5.426[c]	10.81[c]	1.992[c]	1.45[c]	-
CZTSe Kesterite (sim)	5.717	11.378	1.990	0.55	0.000
CZTSe Stannite (sim)	5.696	11.455	2.011	0.35	4.920
CZTSe PMCA (sim)	5.692	11.463	2.014	0.27	9.007
CZTSe Kesterite (exp)	5.680[d]	11.360[d]	2.000[d]	1.0[e]	-
CZTSe Stannite (exp)	5.684[f], 5.688[g]	11.353[f], 11.338[g]	1.997[f], 1.993[g]	0.9[f]	-

a Reference 6; b Reference 50; c Reference 51; d Reference 52; e Reference 47; f Reference 53; g Reference 54

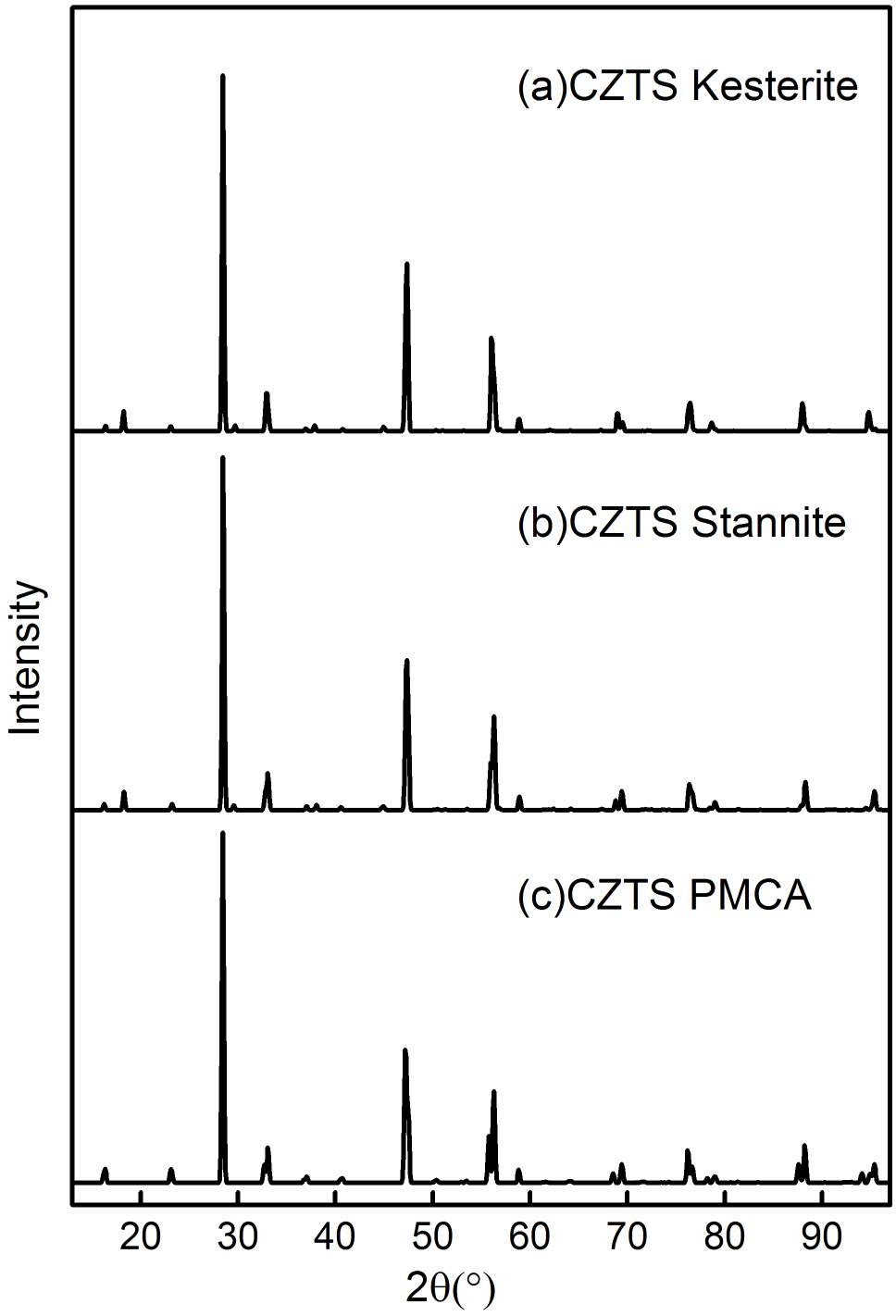

Figure 6.2 Simulated X-ray diffraction patterns for the three CZTS structures using the relaxed lattice parameters.

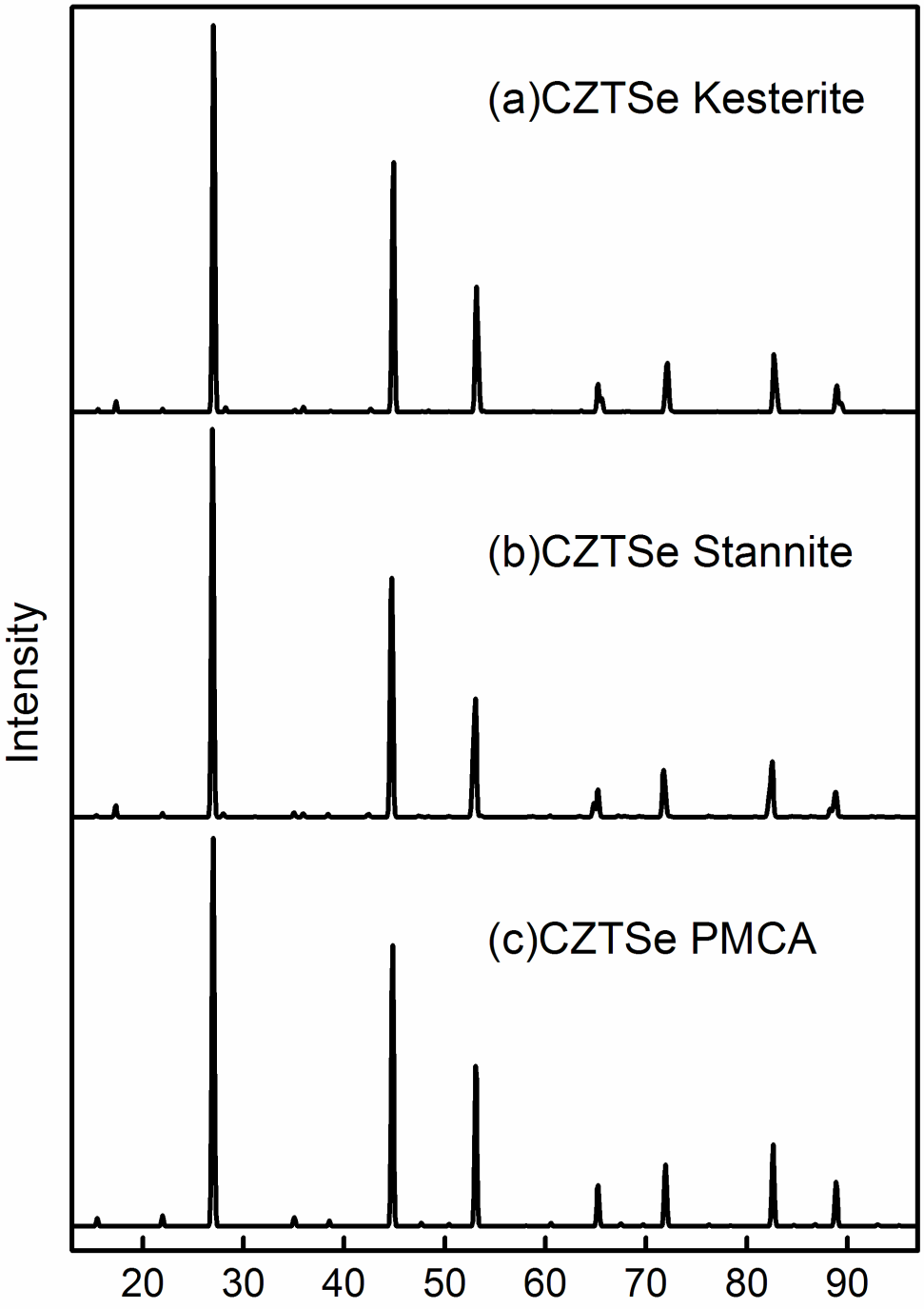

Figure 6.3 Simulated X-ray diffraction patterns for the three CZTSe structures using the relaxed lattice parameters.

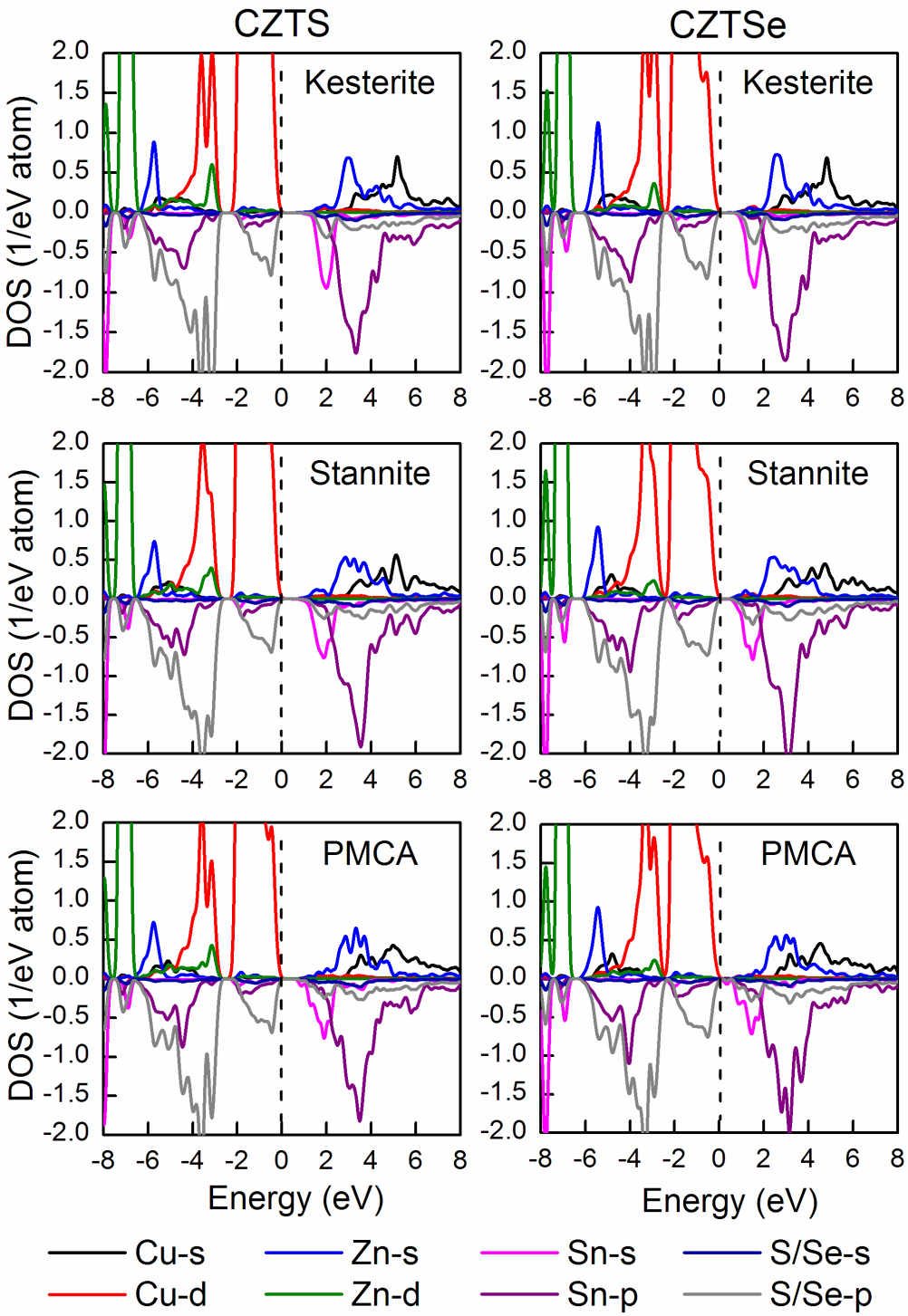

Figure 6.4 Atom-resolved electronic density of states (DOS) for the KS, ST, and PMCA structures of CZTS and CZTSe, presented with a 0.01 Ry Gaussian broadening.

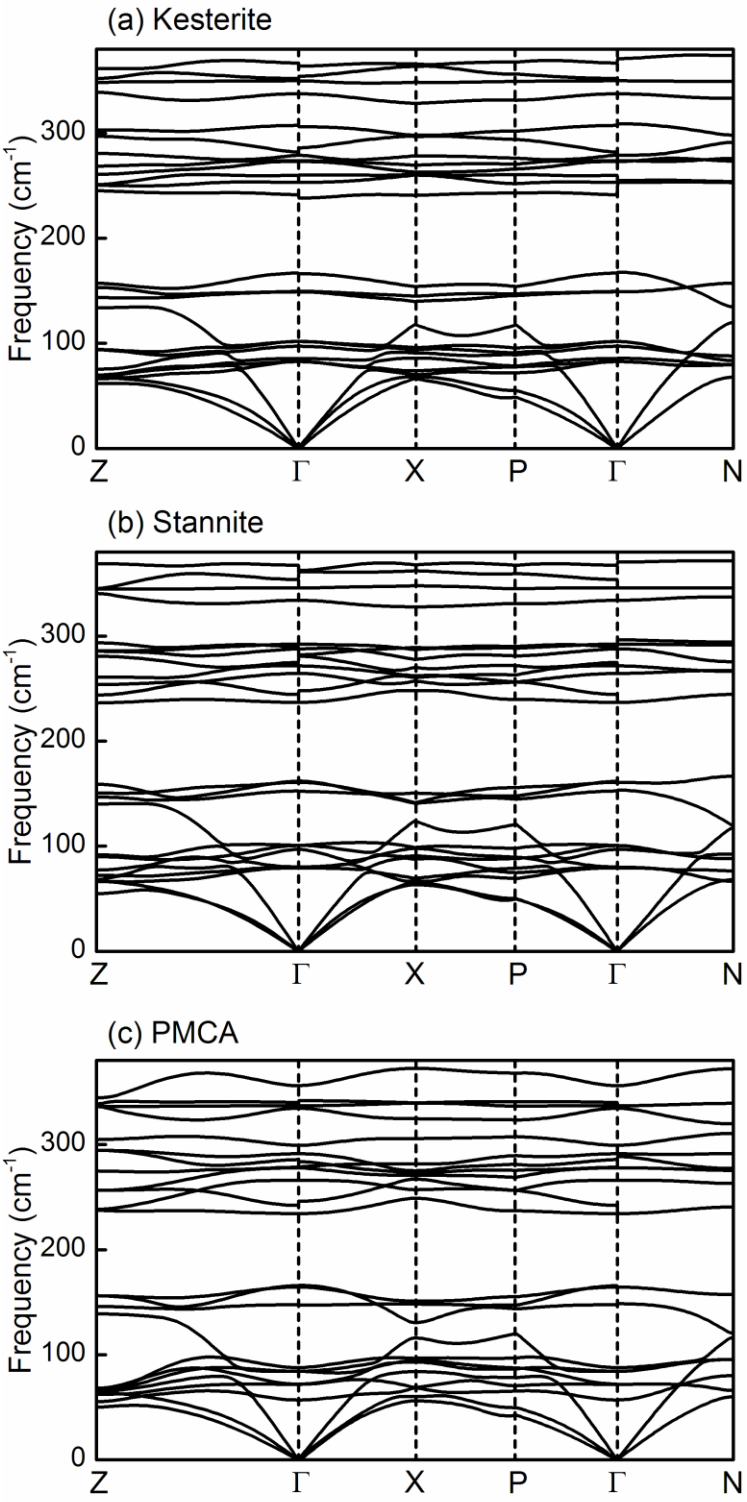

Figure 6.5 Phonon dispersion curves for CZTS (a) KS, (b) ST, and (c) PMCA structures.

Figure 6.6 shows the partial and total phonon density of states (PDOS) for the KS, ST, and PMCA structures. These figures show common characteristics. The phonon states around 50-160 cm^{-1} are mainly comprised of vibrations of the three metal cations with some contribution from the sulfur anions. The phonon states around 250 – 300 cm^{-1} are mainly composed of vibrations of the Zn cations and S anions with some contribution from the Cu cations. The phonon states from 310-340 cm^{-1} are mainly a result of vibrations of S anions, whereas those from 340-370 cm^{-1} are composed of the vibrations of Sn cations and S anions. These results further support the similarity in the phonon modes of the three CZTS structures and indicate that for a given frequency, the phonon vibrations involve the vibrations of the same atoms of the three CZTS structures.

Raman scattering probes the optical phonon modes at the Γ-point (k=0) and has been shown to be a sensitive technique to distinguish CZTS from other potential impurity phases such as ZnS and CTS.[23,24] The optical modes of a crystal structure at k=0 can be enumerated using the crystal's symmetry and a group theory analysis, which for the KS structure, gives[41,42] using Mulliken notation, $\Gamma=3A+6B+6E^1+6E^2$. Amongst these modes, 15 A, B, E^1, and E^2 modes are Raman active and 12 B, E^1, and E^2 modes are IR active. For the ST structure,[43] $\Gamma=2A_1+A_2+2B_1+4B_2+6E$, and amongst these modes, 14 A_1, B_1, B_2, and E vibrational modes are Raman active and 10 B_2 and E modes are IR active. Group analysis of the PMCA structure using the Bilbao crystallographic server[41] gives $\Gamma=2A_1+2A_2+B_1+4B_2+6E$. Amongst these modes, 13 A_1, B_1, B_2, and E modes are Raman active whereas 10 B_2 and E modes are IR active. The A_1 and A_2 modes for ST and PMCA and the A mode for KS result from symmetric vibrations of only the anion lattice and do not involve any cation motion. According to Himmrich *et al.*,[43] these modes are responsible for the strongest lines observed in the experimental Raman spectra for CZTS and they are not expected to shift significantly if the metal cations are replaced with metals other than Cu, Zn, and Sn. In other words, these modes are independent of the cation mass.

The phonon frequencies of the three CZTS structures at the Γ- point are listed in Table 6.2. The most intense experimentally observed Raman peaks from CZTS single-crystals are at 338 cm^{-1} and 287 cm^{-1}.[44] Comparisons of these values to the calculated Raman mode frequencies in Table 6.2 show that the most intense Raman peak at 338 cm^{-1} can be assigned to (i) the A mode of KS (340.04 cm^{-1}), (ii) the A_1 mode of ST (334.08 cm^{-1}), or (iii) the A_1 mode of PMCA (334.42 cm^{-1}). In fact, the most intense Raman peak from CZTS films has been observed between 331-338 cm^{-1} and varies with the synthesis method[9,11,23,24,42,43,45] though reports of 337-338 cm^{-1} are the most common. The most frequently observed 338 cm^{-1} peak is closest to the calculated A mode of the CZTS KS structure. The KS structure is also the most stable amongst the three structures, albeit by only 5 meV/atom. The A_1 peak for the ST and PMCA structures are shifted by 4 cm^{-1}, within the broadening of the KS peak. The second most intense Raman peak at 287 cm^{-1} can be assigned to (i) the A mode of KS (284.30 cm^{-1}), (ii) the A_1 mode of ST (277.12 cm^{-1}) or (iii) the A_1 mode of PMCA (299.25 cm^{-1}) structures. Although the calculated A mode of CZTS KS is the closest match to the experimentally observed peak, the presence of the A_1 mode of ST which is shifted from the A mode of KS by about 8 cm^{-1} cannot be ruled out due to peak broadening. The A_1 mode of PMCA, however, is shifted from the A mode of KS by about 15 cm^{-1}. If we assume that the three structures have similar Raman cross sections, a significant presence of the PMCA structure within a given sample may lead to a Raman scattering peak shifted significantly (15 cm^{-1}) from the 287 cm^{-1} KS peak. An absence of such a peak indicates absence of a significant amount of PMCA phase within a given sample.

A cursory comparison of the experimentally observed peak locations with those in Table 6.2 and the discussion above suggests that the KS structure is the dominant phase in most of the reported CZTS thin films. However, the observed variations in peak shape and locations in both CZTS and CZTSe thin films and nanocrystals synthesized using different methods prompted us to examine the Raman spectra of CZTS and CZTSe in more detail. Figure 6.7 (a) shows the Raman spectrum of a polycrystalline CZTS film made by annealing a film cast from colloidal dispersion of CZTS nanocrystals. To

illustrate that the most intense Raman scattering from CZTS films may have contributions from more than a single structure, we deconvoluted the experimental Raman spectrum in two ways. First, we assumed that each of the two most intense Raman scattering peaks at 338 cm^{-1} and 287 cm^{-1} is due to a single scattering peak (*i.e.*, we assumed that the film contains only the KS CZTS structure). The deconvolution, using Gaussian line shapes, is shown in Figure 6.7 (a). Second, we assumed that each of the most intense peaks consists of two closely spaced but different scattering peaks (*i.e.*, we assumed that the film contains both KS and ST phases.) The peak positions were not fixed *a priori*, but were allowed to vary to get the best fit to the experimental spectra. In the first deconvolution approach, the sum of all the peaks [green curve in Figure 6.7 (a)] matches the experimental CZTS Raman spectrum [solid triangles in Figure 6.7 (a)] everywhere except near the low wavenumber shoulder of the 337 cm^{-1} peak. Figure 6.7 (c) quantifies this poor matching and shows the residual difference (red dashed line) between the experimental data [solid triangles in Figure 6.7 (a)] and the sum of the deconvoluted peaks [blue curve in Figure 6.7 (a)]. Significant deviations exist between the deconvoluted curve and the experimental data.

The deconvolution improves significantly when we assume that the 337 cm^{-1} peak consists of two peaks, one at 335 cm^{-1} and another at 338 cm^{-1} [Figure 6.7 (b)]. The corresponding residual is shown in Figure 6.7 (c). These peak positions at 335 cm^{-1} and 338 cm^{-1} match closely to the calculated A mode of the KS and A_1 mode of the ST structures, respectively. A significant presence of the PMCA structure within the sample can be ruled out based on the absence of a secondary Raman scattering peak, separated from the 284 cm^{-1} peak of the A mode of KS. Using Lorentzian line shapes resulted in poor fits to the experimental data regardless of the number of peaks used to represent the experimental spectra. The broadening in the Raman spectrum from polycrystalline thin film samples is due to inhomogeneous broadening and the frequency distribution in inhomogeneous broadening is best described by a Gaussian line shape rather than a Lorentzian line shape. Infrared absorption cross-sections were calculated to be similar for the same modes in different structures. Assuming that the KS and ST structures have

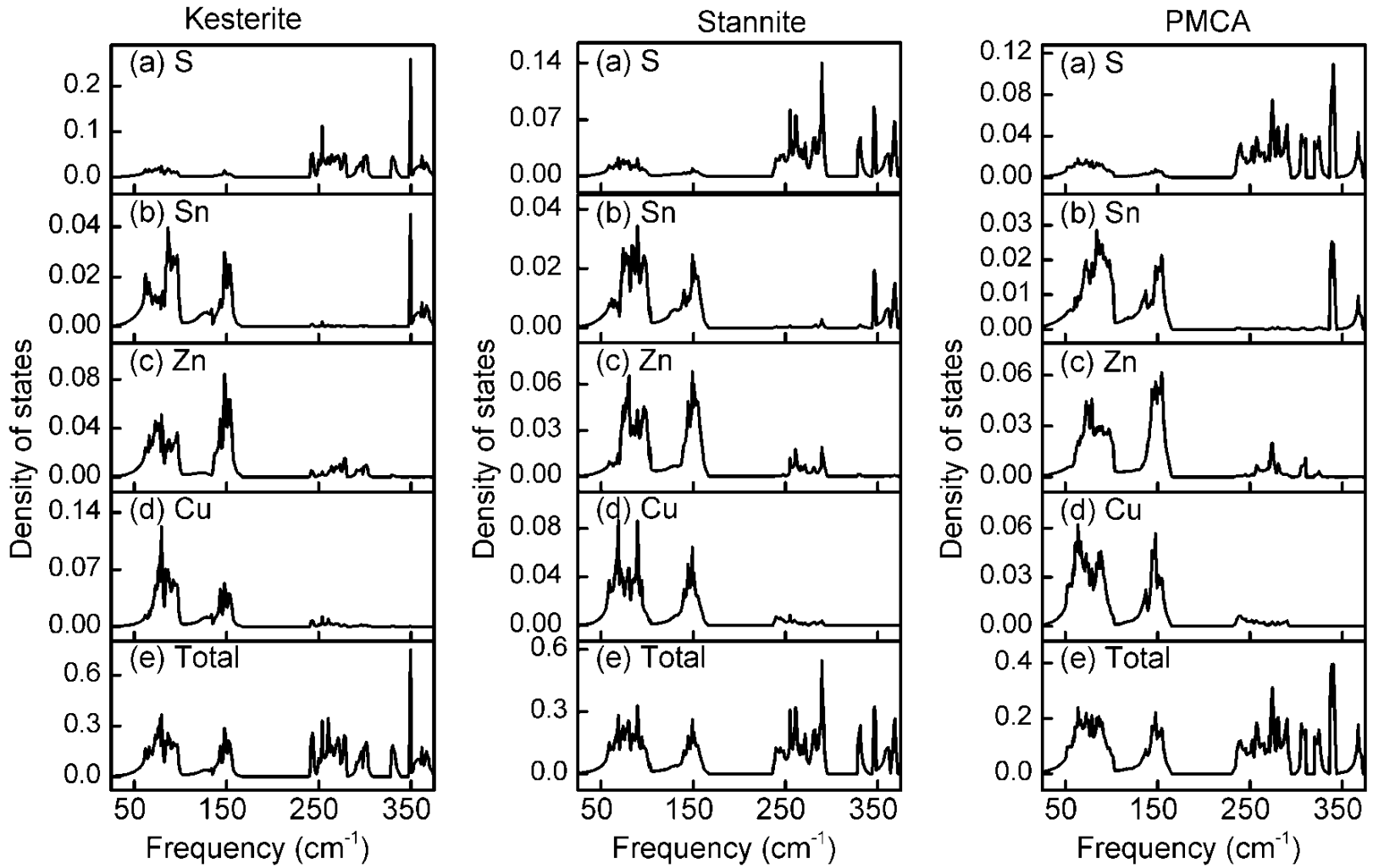

Figure 6.6 Phonon density of states for CZTS (a) KS, (b) ST, and (c) PMCA structures.

Table 6.2 . Calculated Γ-point phonon frequencies (in cm^{-1}) of the CZTS KS, ST, and PMCA structures. The experimental Raman (from Ref. 44) and IR (from Ref. 43) frequencies are also shown for comparison.

Kesterite			Stannite			PMCA			Exp. data	
Symmetry	This work		Symmetry	This work		Symmetry	This work		Raman	IR
A	340.04		A_1	334.08		A_1	334.42		338.00	
	284.30			277.12			299.25		287.00	
	272.82		A_2	263.11		A_2	266.13			
B (TO LO)	355.80	374.05	B_1	291.12			61.17		368.00	
	309.56	313.19		74.17		B_1	291.18			316.00
	238.48	254.73	B_2 (TO LO)	360.12	370.63	B_2 (TO LO)	341.77	356.57		
	166.65	168.21		277.08	291.82		278.85	288.88		168.00
	98.82	98.83		149.69	150.91		148.63	149.90		
	86.70	87.51		95.85	95.86		87.21	87.26		86.00
E (TO LO)	351.55	366.35	E (TO LO)	346.01	364.87	E (TO LO)	336.98	357.95	351.00	351.00
	281.07	293.44		264.37	275.52		277.85	284.12		293.00
	250.26	257.85		235.41	246.58		234.77	247.02	252.00	255.00
	150.53	151.05		161.68	162.63		164.81	166.56		143.00
	105.93	106.00		97.34	97.38		86.29	86.32		
	83.64	83.65		78.39	78.73		73.26	73.86		68.00

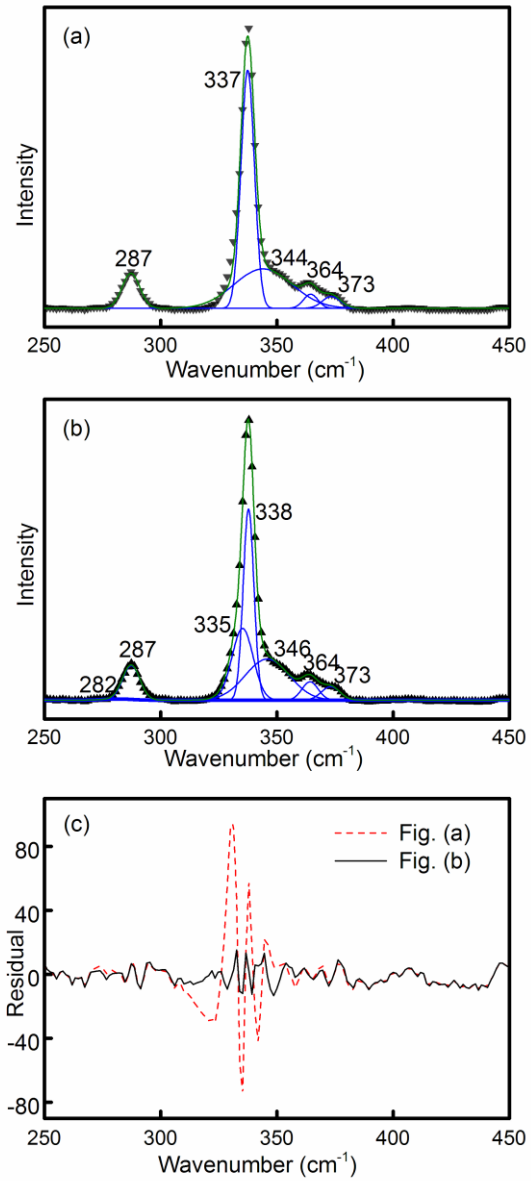

Figure 6.7 Raman spectrum (filled triangles) of a CZTS thin film. The green line is the sum of the peaks (blue) used to deconvolute the experimental spectrum. In (a), each of the two most intense Raman scattering peaks at 338 cm^{-1} and 287 cm^{-1} is assumed to be due to scattering from KS CZTS only. In (b) the same peaks are assumed to consist of two closely spaced scattering peaks from KS (287 cm^{-1} and 338 cm^{-1}) and ST phases (282 cm^{-1} and 335 cm^{-1}). (c) The residual difference between the experimental Raman spectrum (solid triangles) and the sum of the scattering peaks used to deconvolute the experimental spectrum (green line).

similar Raman cross-sections, and using the ratio of the area under the 338 cm^{-1} peak (KS) to that under the 335 cm^{-1} peak (ST), we estimate that this particular CZTS thin film is a mixture of 60 % KS and 40 % ST.

The Raman scattering peak at 287 cm^{-1} in the experimental CZTS Raman spectrum can be attributed to either the A mode of KS at 284.30 cm^{-1} or the A_1 mode of ST at 277.12 cm^{-1}; the peak at 346 cm^{-1} can be attributed to either the E (TO) mode of KS at 351.55 cm^{-1} or the E (TO) mode of ST at 346.01 cm^{-1}; the peak at 364 cm^{-1} can be attributed to either the E (LO) mode of KS at 366.35 cm^{-1} or the E (LO) mode of ST at 364.87 cm^{-1}; and the peak at 373 cm^{-1} can be attributed to either the B (LO) mode of KS at 374.05 cm^{-1} or the B_2 (LO) mode of ST at 370.63 cm^{-1}, respectively.

The phonon frequencies of the three CZTSe structures at the Γ-point are listed in Table 6.3. The most intense experimentally observed Raman peaks for CZTSe single-crystals are at 196 cm^{-1} and 173 cm^{-1}.[44] Comparisons of these values to the calculated Raman frequencies in Table 6.3 shows that the most intense Raman peak at 196 cm^{-1} can be assigned to (i) the A mode of KS (193.01 cm^{-1}), (ii) the A_1 mode of ST (184.50 cm^{-1}), (iii) the E mode of ST (198.97 cm^{-1}), (iv) the A_1 mode of PMCA (185.44 cm^{-1}), or (v) the E mode of PMCA (193.93 cm^{-1}). The E mode of the ST and PMCA structures involves both cation and anion vibrations and consequently exhibits LO-TO splitting. If the experimentally observed peak at 196 cm^{-1} is an E mode it would be expected to shift within a polycrystalline sample depending on the local sample orientation and be sensitive to the sample stoichiometry. The most intense Raman peak from CZTSe films has been observed between 195-198 cm^{-1}, very close to the single-crystal Raman scattering peak at 196 cm^{-1}.[46-48] This shift is small compared to the shift (7 cm^{-1}) that would be expected based on LO-TO splitting and no sensitivity to orientation or sample stoichiometry has been reported. Moreover, the similarity between CZTS and CZTSe suggests that the A_1 mode of ST is responsible for the most intense peak in CZTSe. A recent report on the vibrational properties of CZTS and CZTSe computed using Fritz-Haber-Institut (FHI) type norm-conserving Trouiller-Martins pseudopotentials predicts

that the most intense CZTSe Raman peak is due to either the A mode of KS (196.2 cm^{-1}) or the A_1 mode of ST (194.6 cm^{-1}).[31] Unfortunately, the report does not contain a calculation of the vibrational properties of PMCA.

Similar to CZTS, to illustrate that the most intense Raman scattering from CZTSe films may have contributions from more than one structure, we deconvoluted an experimental Raman spectrum in two ways. First, we assumed that the most intense Raman scattering peak at 198 cm^{-1} is due to a single scattering peak (*i.e.*, we assumed that the film contains only the KS CZTSe structure). Second, we assumed that each of the most intense peaks consists of two closely spaced but different scattering peaks (*i.e.*, we assumed that the film contains both KS and ST phases.) In the first deconvolution approach, the sum of all the peaks [green curve in Figure 6.8 (a)] matches the experimental CZTSe Raman spectrum [solid triangles in Figure 6.8 (a)] everywhere except near the low wavenumber shoulder of the 198 cm^{-1} peak. Figure 6.8 (c) quantifies this poor matching and shows the residual difference (red dashed line) between the experimental data [solid triangles in Figure 6.8 (a)] and the sum of the deconvoluted peaks [blue curve in Figure 6.8 (a)]. The deconvolution improves significantly when we assume that the 198 cm^{-1} peak consists of two peaks, one at 198 cm^{-1} and another at 195 cm^{-1} [Figure 6.8 (b)]. The corresponding residual is shown in Figure 6.8 (c). These peak positions at 198 cm^{-1} and 195 cm^{-1} match closely to the calculated A mode of KS (196.2 cm^{-1}) and the A_1 mode of ST (194.6 cm^{-1}), respectively.[31] Assuming that the KS and ST structures have similar Raman cross-sections, and using the ratio of the area under the 198 cm^{-1} peak (KS) to that under the 195 cm^{-1} peak (ST), we estimate that this particular CZTS thin film may be a mixture of 65 % KS and 35 % ST phases. Again, using Lorentzian lineshapes gives poor representation of the experimental data regardless of the number of peaks used for the deconvolution.

The Raman scattering peak at 165 cm^{-1} in the experimental CZTSe Raman spectrum can be attributed to either the E mode of KS at 159.0 cm^{-1}, B_2 mode of ST at 162.5 cm^{-1}, or the E mode of ST at 163.1 cm^{-1}; the peak at 174 cm^{-1} can be attributed to

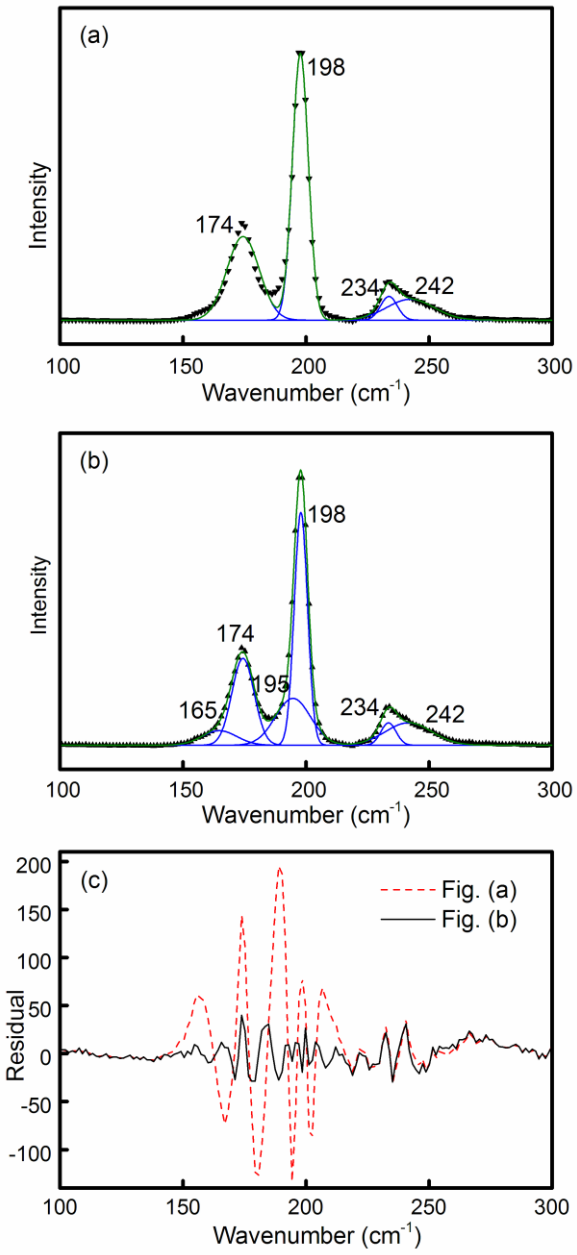

Figure 6.8 Raman spectrum (filled triangles) of a CZTSe thin film. The green line is a sum of the peaks (blue) used to deconvolute the experimental spectrum. In (a), the most intense Raman scattering peak at 198 cm^{-1} is assumed to be due to scattering from KS CZTSe only. In (b) this peak is assumed to consist of two closely spaced scattering peaks from KS (198 cm^{-1}) and ST phases (195 cm^{-1}). (c) The residual difference between the experimental Raman spectrum (solid triangles) and the sum of the scattering peaks used to deconvolute the experimental spectrum (green line).

Table 6.3 Γ-point phonon frequencies (in cm^{-1}) of the CZTSe KS, ST, and PMCA structures. The experimental Raman frequencies (from Ref. 44) are also shown for comparison.

Kesterite			Stannite			PMCA			Exp. data
Symmetry	This work		Symmetry	This work		Symmetry	This work		Raman
A	213.05		A_1	213.83		A_1	208.85		231.00
	193.01			184.50			185.44		196.00
	188.10		A_2	175.40		A_2	182.40		173.00
B (TO LO)	236.30	246.97	B_1	205.44		B_1	171.64		
	226.81	229.55		73.60		B_2 (TO LO)	237.85	247.09	
	193.22	199.29	B_2 (TO LO)	248.01	255.37		204.80	205.65	
	157.98	159.24		213.89	217.95		148.68	150.13	
	93.33	93.55		151.09	152.34		81.31	81.35	
	85.42	85.87		94.28	94.28		38.12	38.12	
E (TO LO)	233.02	242.85	E (TO LO)	237.09	245.23	E (TO LO)	230.59	236.93	
	221.50	226.37		198.97	205.22		193.93	199.14	
	194.47	198.01		185.50	190.62		176.84	179.19	
	147.82	148.34		155.35	155.77		158.10	159.43	
	101.58	101.71		100.41	100.43		85.32	85.32	
	80.70	80.75		80.77	80.90		60.03	60.11	

the B mode of KS at 171.5 cm^{-1}; and the one at 234 cm^{-1} can be attributed to the B (LO) mode of KS at 236.0 cm^{-1} or the B_2 (TO) mode of ST at 233.0 cm^{-1}.[31] The Raman scattering peak at 242 cm^{-1} is due to scattering from $MoSe_2$ that forms at the CZTSe-Mo junction due to the selenization of the underlying Mo.[49]

6.5 Summary

Lattice dynamics and electronic properties of kesterite, stannite, and PMCA structures of CZTS and CZTSe were studied through DFT. The equilibrium lattice parameters are in excellent agreement with the experimental data. The phonon dispersion curves for the three structures of CZTS (CZTSe), calculated using density functional perturbation theory, although similar, show unique features that can be used to differentiate them. The phonon vibration frequencies for CZTS at the Γ-point agree well with the experimentally observed Raman and IR peaks. Careful examination and deconvolution of the CZTS and CZTSe Raman spectra suggest that the most intense Raman scattering peaks consist of two modes, which are slightly shifted from each other. Comparison of the locations of these peaks with those calculated from DFT suggests that they may be attributed to Raman scattering from the KS and ST structures of CZTS and CZTSe that co-exist within a polycrystalline thin-film sample.

6.6 References

1 C. A. Wolden, J. Kurtin, J. B. Baxter, I. Repins, S. E. Shaheen, J. T. Torvik, A. A. Rockett, V. M. Fthenakis, and E. S. Aydil, J. Vac. Sci. Technol. A **29**, 030801 (2011).
2 D. B. Mitzi, O. Gunawan, T. K. Todorov, K. Wang, and S. Guha, Sol. Energy Mater. Sol. Cells **95**, 1421 (2011).
3 H. Katagiri, K. Jimbo, W. S. Maw, K. Oishi, M. Yamazaki, H. Araki, and A. Takeuchi, Thin Solid Films **517**, 2455 (2009).
4 H. Wang, Int. J. Photoenergy **2011**, 801292 (2011).
5 W. Shockley, and H. J. Queisser, J. Appl. Phys. **32**, 510 (1961).

6 T. K. Todorov, K. B. Reuter, and D. B. Mitzi, Adv. Mater. **22**, E156 (2010).
7 Q. Guo, G. M. Ford, W. Yang, B. C. Walker, E. A. Stach, H. W. Hillhouse, and R. Agrawal, J. Am. Chem. Soc. **132**, 17384 (2010).
8 O. Gunawan, T. K. Todorov, and D. B. Mitzi, Appl. Phys. Lett. **97**, 233506 (2010).
9 K. Wang, O. Gunawan, T. Todorov, B. Shin, S. J. Chey, N. A. Bojarczuk, D. Mitzi, and S. Guha, Appl. Phys. Lett. **97**, 143508 (2010).
10 K. Jimbo, R. Kimura, T. Kamimura, S. Yamada, W. S. Maw, H. Araki, K. Oishi, and H. Katagiri, Thin Solid Films **515**, 5997 (2007).
11 Y. Wang, and H. Gong, J. Electrochem. Soc. **158**, H800 (2011).
12 A. Ennaoui, M. Lux-Steiner, A. Weber, D. Abou-Ras, I. Kötschau, H. Schock, R. Schurr, A. Hölzing, S. Jost, R. Hock, T. Voß, J. Schulze, and A. Kirbs, Thin Solid Films **517**, 2511 (2009).
13 V. G. Rajeshmon, C. S. Kartha, K. P. Vijayakumar, C. Sanjeeviraja, T. Abe, and Y. Kashiwaba, Solar Energy **85**, 249 (2011).
14 H. Araki, A. Mikaduki, Y. Kubo, T. Sato, K. Jimbo, W. S. Maw, H. Katagiri, M. Yamazaki, K. Oishi, and A. Takeuchi, Thin Solid Films **517**, 1457 (2008).
15 K. Moriya, K. Tanaka, and H. Uchiki, Jpn. J. Appl. Phys. **46**, 5780 (2007).
16 W. Ki, and H. W. Hillhouse, Adv. Energy Mater. **1**, 732 (2011).
17 Q. Guo, H. W. Hillhouse, and R. Agrawal, J. Am. Chem. Soc. **131**, 11672 (2009).
18 C. Steinhagen, M. G. Panthani, V. Akhavan, B. Goodfellow, B. Koo, and B. A. Korgel, J. Am. Chem. Soc. **131**, 12554 (2009).
19 D. A. R. Barkhouse, O. Gunawan, T. Gokmen, T. K. Todorov, and D. B. Mitzi, Prog. Photovolt: Res. Appl. **20**, 6 (2012).
20 S. Chen, X. G. Gong, A. Walsh, and S. Wei, Appl. Phys. Lett. **94**, 041903 (2009).
21 C. Persson, J. Appl. Phys. **107**, 053710 (2010).
22 S. Schorr, H. Hoebler, and M. Tovar, Eur. J. Mineral. **19**, 65 (2007).
23 P. A. Fernandes, P. M. P. Salome, and A. F. da Cunha, Thin Solid Films **517**, 2519 (2009).
24 A. J. Cheng, M. Manno, A. Khare, C. Leighton, S. A. Campbell, and E. S. Aydil, J. Vac. Sci. Technol. A **29**, 051203 (2011).
25 S. Chen, J. Yang, X. G. Gong, A. Walsh, and S. Wei, Phys. Rev. B **81**, 245204 (2010).
26 J. Paier, R. Asahi, A. Nagoya, and G. Kresse, Phys. Rev. B **79**, 115126 (2009).
27 A. Nagoya, R. Asahi, R. Wahl, and G. Kresse, Phys. Rev. B **81**, 113202 (2010).
28 N. B. Mortazavi Amiri, and A. Postnikov, Phys. Rev. B **82**, 205204 (2010).
29 S. Chen, A. Walsh, J. Yang, X. G. Gong, L. Sun, P. Yang, J. Chu, and S. Wei, Phys. Rev. B **83**, 125201 (2011).
30 T. Maeda, S. Nakamura, and T. Wada, Jpn. J. Appl. Phys. **50**, 04DP07 (2011).
31 T. Gurel, C. Sevik, and T. Cagin, Phys. Rev. B **84**, 205201 (2011).
32 P. Hohenberg, and W. Kohn, Phys. Rev. **136**, B864 (1964).
33 W. Kohn, and L. J. Sham, Phys. Rev. **140**, A1133 (1965).
34 D. Vanderbilt, Phys. Rev. B **41**, 7892 (1990).
35 P. Giannozzi, S. Baroni, N. Bonini, M. Calandra, R. Car, C. Cavazzoni, D. Ceresoli, G. L. Chiarotti, M. Cococcioni, I. Dabo, A. D. Corso, S. d. Gironcoli, S. Fabris, G.

Fratesi, R. Gebauer, U. Gerstmann, C. Gougoussis, A. Kokalj, M. Lazzeri, L. Martin-Samos, N. Marzari, F. Mauri, R. Mazzarello, S. Paolini, A. Pasquarello, L. Paulatto, C. Sbraccia, S. Scandolo, G. Sclauzero, A. P. Seitsonen, A. Smogunov, P. Umari, and R. M. Wentzcovitch, J. Phys. : Condens. Matter **21**, 395502 (2009).
36 J. P. Perdew, K. Burke, and M. Ernzerhof, Phys. Rev. Lett. **77**, 3865 (1996).
37 H. J. Monkhorst, and J. D. Pack, Phys. Rev. B **13**, 5188 (1976).
38 A. Khare, A. W. Wills, L. M. Ammerman, D. J. Norris, and E. S. Aydil, Chem. Commun. **47**, 11721 (2011).
39 A. Seidl, A. Gorling, P. Vogl, J. A. Majewski, and M. Levy, Phys. Rev. B **53**, 3764 (1996).
40 S. Baroni, S. de Gironcoli, A. Dal Corso, and P. Giannozzi, Rev. Mod. Phys. **73**, 515 (2001).
41 M. I. Aroyo, J. Perez-Mato, C. Capillas, E. Kroumova, S. Ivantchev, G. Madariaga, A. Kirov, and H. Wondratschek, Z. Kristallogr. **221**, 15 (2006).
42 P. K. Sarswat, M. L. Free, and A. Tiwari, Phys. Status Solidi (b) **248**, 2170 (2011).
43 M. Himmrich, and H. Haeuseler, Spectrochim. Acta Part A: Mol. Spectrosc. **47**, 933 (1991).
44 M. Altosaar, J. Raudoja, K. Timmo, M. Danilson, M. Grossberg, J. Krustok, and E. Mellikov, Phys. Status Solidi (a) **205**, 167 (2008).
45 D. B. Mitzi, T. K. Todorov, O. Gunawan, Min Yuan, Qing Cao, Wei Liu, K. B. Reuter, M. Kuwahara, K. Misumi, A. J. Kellock, S. J. Chey, T. G. de Monsabert, A. Prabhakar, V. Deline, and K. E. Fogel, in *Proceedings of the 35th IEEE Photovoltaic Specialists Conference* (IEEE, 2010), pp. 640–645.
46 P. M. P. Salomé, P. A. Fernandes, and A. F. d. Cunha, Phys. Status Solidi (c) **7**, 913 (2010).
47 S. Ahn, S. Jung, J. Gwak, A. Cho, K. Shin, K. Yoon, D. Park, H. Cheong, and J. H. Yun, Appl. Phys. Lett. **97**, 021905 (2010).
48 P. M. P. Salomé, P. A. Fernandes, A. F. da Cunha, J. P. Leitão, J. Malaquias, A. Weber, J. C. González, and M. I. N. da Silva, Sol. Energy Mater. Sol. Cells **94**, 2176 (2010).
49 T. Sekine, M. Izumi, T. Nakashizu, K. Uchinokura, and E. Matsuura, J. Phys. Soc. Jpn. **49**, 1069 (1980).
50 N. Kamoun, H. Bouzouita, and B. Rezig, Thin Solid Films **515**, 5949 (2007).
51 H. Katagiri, N. Sasaguchi, S. Hando, S. Hoshino, J. Ohashi, and T. Yokota, Sol. Energy Mater. Sol. Cells **49**, 407 (1997).
52 G. S. Babu, Y. B. K. Kumar, P. U. Bhaskar, and V. S. Raja, Semicond. Sci. Technol. **23**, 085023 (2008).
53 G. Zoppi, I. Forbes, R. W. Miles, P. J. Dale, J. J. Scragg, and L. M. Peter, Prog. Photovolt: Res. Appl. **17**, 315 (2009).
54 I. D. Olekseyuk, L. D. Gulay, I. V. Dydchak, L. V. Piskach, O. V. Parasyuk, and O. V. Marchuk, J. Alloys Comp. **340**, 141 (2002).

Chapter 7

First Principles Calculation of The Electronic Properties And Lattice Dynamics of $Cu_2ZnSn(S_{1-x}Se_x)_4$

In this chapter, using density functional theory, we calculated the electronic structure, the lattice dynamics, and the Raman spectra of $Cu_2ZnSn(S_{1-x}Se_x)_4$, (CZTSSe) an emerging photovoltaic material for thin-film solar cells. In particular, we investigated the effects of the local arrangement of S and Se within the unit cell on the electronic properties of these materials. We find that the S-to-Se ratio (*e.g.*, x) and the spatial distribution of the anions in the unit cell can significantly alter the band structure. In particular, the S-to-Se ratio and anion distribution determines the energy splitting between the electronic states at the top of the valence band and the hole mobility in CZTSSe alloys and solar cells. Moreover, we find that X-ray diffraction patterns and phonon dispersion curves are sensitive to the local anion ordering. The predicted Raman scattering frequencies and their variation with x agree with experimentally determined values and trends.

7.1 Introduction

Copper zinc tin sulfide (Cu_2ZnSnS_4 or CZTS), copper zinc tin selenide ($Cu_2ZnSnSe_4$ or CZTSe), and their alloys ($Cu_2ZnSn[S_{1-x}Se_x]_4$ with $0 \leq x \leq 1$ or CZTSSe) are emerging as important light absorbing materials for thin film solar cells.[1-3] CZTS and CZTSe have band gaps of 1.45 and 1.0 eV, respectively, and their alloy, CZTSSe, covers the optimal energy range for converting solar radiation to electrical current.[4] CZTSSe, like CZTS and CZTSe, has a high absorption coefficient ($>10^4$ cm^{-1})[3,5,6] in the visible range of the electromagnetic spectrum and only a few micron thick films can absorb all the incoming radiation above the band gap. CZTS thin films have been synthesized using

chemical bath deposition,[7] pulsed laser deposition,[8] co-sputtering,[9] co-evaporation,[10] sulfidation of copper-zinc-tin stacks,[11] casting from nanocrystal dispersions,[6,12-14] spray pyrolysis,[15] spin coating from precursor solutions,[16] and electrodeposition.[17] Recently, CZTSSe solar cells have been shown to achieve a power conversion efficiency of ~10.1%.[18]

CZTS (CZTSe) crystallizes in a tetragonal structure with c≈2a. The structure is pseudo-cubic and may be thought of as two zinc blende lattices stacked on top of each other with Cu, Zn, and Sn occupying half of the tetrahedral positions within the S (Se) face-centered-cubic sublattice. Depending on the relative arrangement of Cu, Zn, and Sn within the S (Se) sublattice, CZTS (CZTSe) can crystallize in three different crystal structures – kesterite, stannite, and pre-mixed Cu-Au (PMCA) structures. These structures are very close in energy to each other and may coexist at room temperature.[19-21] In addition, due to the similarity between their crystal structures, the electronic and the vibrational properties of the three phases are also very similar.[19-21] The structure of CZTS (CZTSe) is similar to that of ZnS (ZnSe) and Cu_2SnS_3 (Cu_2SnSe_3). In all these structures, the S (Se) sublattice determines the dimensions of the unit cell and different combinations and proportions of Zn, Cu, and Sn cations occupy the tetrahedral voids between S (Se) anions. Because, S (Se) determines the unit cell dimensions and because all metal ions have similar electron densities, X-ray diffraction is insensitive to the cation arrangement and XRD patterns from CZTS, ZnS, Cu_2SnS_3 (CZTSe, ZnSe, Cu_2SnSe_3) are virtually indistinguishable within the experimental broadening of the diffraction peaks. Raman spectroscopy has been shown to be an effective characterization method for differentiating between CZTS (CZTSe), ZnS (ZnSe), and Cu_2SnS_3 (Cu_2SnSe_3).[22,23]

Recently, several groups reported calculations of the electronic, structural, and/or vibrational properties of CZTS and/or CZTSe.[19,21,24-29] However, the electronic and structural properties of CZTS-CZTSe alloys have not received equal attention[28] even though the most efficient solar cells have been obtained with CZTSSe alloys rather than phase-pure CZTS or CZTSe. Understanding how the anion arrangement affects the properties of CZTSSe alloys is important for improving solar cells based on these

materials. To fill this knowledge gap, we used *ab initio* computational methods to calculate the electronic, structural, and vibrational properties of a series of CZTS-CZTSe alloys.

7.2 Computational Details

The electronic properties and lattice dynamics of CZTSSe alloys were calculated using density functional theory (DFT)[30-32] within the plane-wave-pseudopotential implementation of the PWscf code contained in the QUANTUM ESPRESSO (QE) package.[33] The Perdew-Burke-Ernzerhof (PBE) flavor[34] of the generalized gradient approximation (GGA) was used to model the exchange-correlation functional. The interaction between the valence electrons and the ionic cores was modeled using ultrasoft pseudopotentials.[32] The electronic wave functions and charge density were expanded on plane-wave basis sets up to kinetic energy cutoffs of 30 and 800 Ry, respectively. Brillouin-zone integration used a Γ-point-centered 6×6×3 Monkhorst-Pack[35] k-point mesh. With this choice of computational parameters, the errors on total energies and atomic forces are estimated to be less than 10^{-4} Ry/atom and 10^{-5} Ry/Bohr, respectively. Prior to the phonon dispersion calculations, both the unit cell and the atomic positions were optimized to obtain the equilibrium crystal structure for each material. The structural optimizations were considered converged when the total energy decreased by less than 10^{-5} Ry /unit cell and the atomic forces were smaller than 10^{-4} Ry/au. The vibrational frequencies and modes for each material were calculated using density functional perturbation theory (DFPT) as implemented in the PHONON code of the QE package.[36] Brillouin zone integration over the vibrational wave vectors (q-points) was done using 2×2×2 grids. The results presented in this paper were tested using finer k-point grids and found to be robust. Although we are mostly interested in the zone-center Raman-active modes, the vibrational spectrum was computed over the entire Brillouin zone to evaluate the phonon density of states.

7.3 Results and Discussion

Figure 7.1 shows the conventional unit cells of the CZTSSe alloys considered in this study. Only the kesterite structure is considered. We compare $Cu_2ZnSn[S_{1-x}Se_x]_4$ where x=0, 0.25, 0.5, 0.75, and 1, corresponding to 0, 1, 2, 3, or 4 Se atoms per primitive

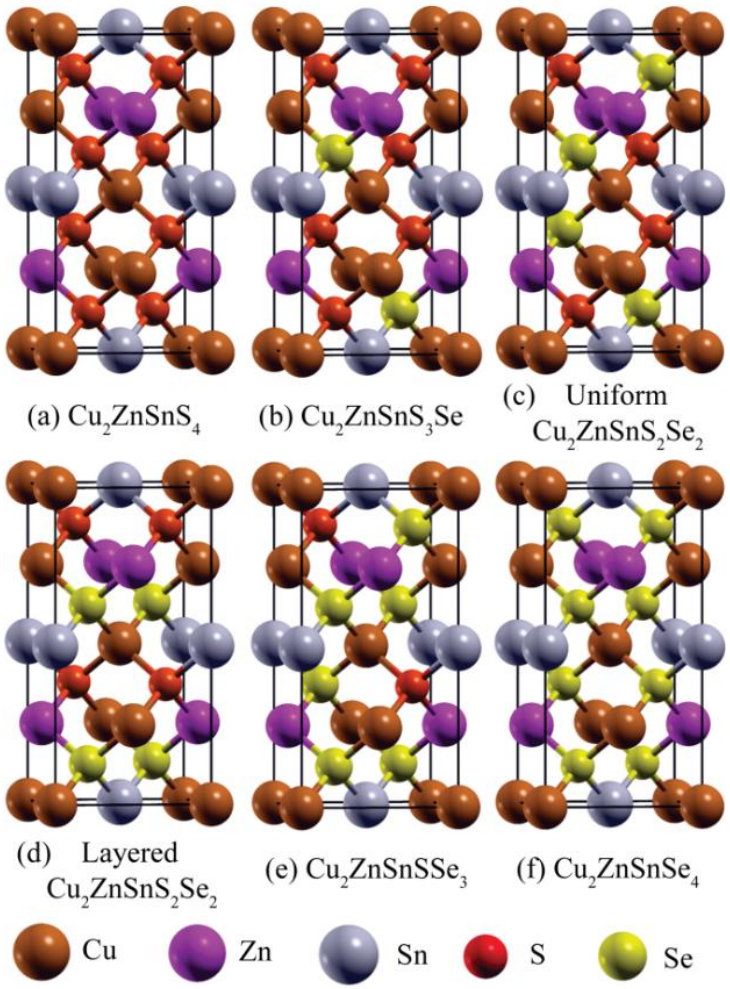

Figure 7.1 Conventional unit cells for the kesterite structure of the CZTSSe alloys having four copper (brown), two zinc (purple), two tin (grey) and eight sulfur (red) /selenium (yellow) atoms per unit cell: (a) Cu_2ZnSnS_4, (b) Cu_2ZnSnS_3Se, (c) Uniform $Cu_2ZnSnS_2Se_2$, (d) Layered $Cu_2ZnSnS_2Se_2$, (e) $Cu_2ZnSnSSe_3$, and (f) $Cu_2ZnSnSe_4$.

unit cell, respectively. For x=0.25 or 0.75, the spatial arrangement of S and Se atoms within the primitive unit cell is unique. However, when x=0.5, there are two possible ways of arranging the S and Se atoms within the primitive unit cell. In one configuration, the S and Se atoms are distributed uniformly within each layer while in a second configuration, a layer of S alternates with a layer of Se. We call these structures uniform-$Cu_2ZnSnS_2Se_2$ and layered-$Cu_2ZnSnS_2Se_2$, respectively.

Relaxed lattice parameters for the CZTSSe alloys are listed in Table 7.1. The unit cell expands when S is replaced with Se because the radius of a selenium atom is larger than the radius of a sulfur atom. The relaxed CZTS (x=0) and CZTSe (x=1) unit cells have tetragonal symmetry but the alloy unit cells lose symmetry and become triclinic. The only exception is the layered-$Cu_2ZnSnS_2Se_2$ structure, which retains its rotational symmetry along c and becomes monoclinic.

Table 7.1 Lattice parameters for the relaxed kesterite structures of CZTSSe alloys. The parameters a, b, c, α, β, and γ refer to a primitive unit cell consisting of two copper, one zinc, one tin, and four sulfur/selenium atoms. E_g is the calculated band gap for the structure.

Material	**a (Å)**	**b (Å)**	**c (Å)**	**α (°)**	**β (°)**	**γ (°)**	**E_g (eV)**
Cu_2ZnSnS_4	6.634	6.634	6.634	70.85	48.40	48.40	0.87
Cu_2ZnSnS_3Se	6.751	6.776	6.742	71.04	48.34	48.54	0.72
Uniform $Cu_2ZnSnS_2Se_2$	6.832	6.869	6.825	70.99	48.47	48.62	0.57
Layered $Cu_2ZnSnS_2Se_2$	6.846	6.865	6.865	71.02	48.27	48.45	0.58
$Cu_2ZnSnSSe_3$	6.921	6.957	6.945	71.03	48.46	48.58	0.42
$Cu_2ZnSnSe_4$	7.020	7.020	7.020	70.86	48.40	48.40	0.27

Figure 7.2 shows the X-ray diffraction (XRD) patterns for the CZTSSe alloys simulated using CrystalMaker® software with the relaxed lattice parameters and assuming a crystallite size of 50 nm. The simulated XRD patterns match the experimental XRD patterns shown in Ref. 37. The diffraction peaks for CZTSSe shift towards lower 2θ as S is replaced with Se and x increases. This shift is due to the expansion of the unit cell

upon replacement of S with Se. Two factors determine the intensities of the diffraction peaks, the atomic scattering factors of the elements and the symmetry of the structure. For the most part, the XRD intensity increases with x because the atomic scattering factor for Se is higher than that for S. However, there are exceptions. For example, the (112) diffraction intensity increases monotonically for x>0.25 but it is higher for Cu_2ZnSnS_4 (x=0) than for Cu_2ZnSnS_3Se (x=0.25) due to loss of tetragonal symmetry in Cu_2ZnSnS_3Se. In tetragonal Cu_2ZnSnS_4, the (112) diffraction is due to the contribution of eight equivalent planes in the {112} family. Upon loss of symmetry, the equivalence between these eight planes disappears and the intensity of the (112) peak decreases. In addition, intensities of some diffractions, such as the (020) and (224) peaks decrease as x increases and finally disappear for $Cu_2ZnSnSe_4$. The (220) diffraction from layered $Cu_2ZnSnS_2Se_2$ is more intense than that from uniform $Cu_2ZnSnS_2Se_2$; the two structures differ only in the arrangement of S and Se within the unit cell. In fact, the ratio of the (112) diffraction intensity to the (220) diffraction intensity increases from 1.5 for the uniform $Cu_2ZnSnS_2Se_2$ to 2.5 for the layered $Cu_2ZnSnS_2Se_2$. The latter is comprised of alternating S and Se layers and has an additional rotational symmetry as compared to the former. This additional symmetry increases the multiplicity, and hence the intensity, of the (220) diffraction peak. The ratio of the (112) diffraction intensity to the (220) diffraction intensity in the experimental XRD pattern for $Cu_2ZnSnS_2Se_2$ from Ref. 37 is 1.5 indicating that this particular material has a uniform distribution of S and Se atoms within the unit cell. From our calculations, the uniform $Cu_2ZnSnS_2Se_2$ is more stable than the layered $Cu_2ZnSnS_2Se_2$ by about 3.5 meV/atom. This small energy difference indicates that both the anion arrangements can co-exist at room temperature within a given experimental sample. Chemical potential would, however, favor the formation of uniform $Cu_2ZnSnS_2Se_2$, as layered $Cu_2ZnSnS_2Se_2$ has lower entropy as compared to uniform $Cu_2ZnSnS_2Se_2$.

Table 7.1 shows the calculated bandgaps for the CZTSSe alloys. As expected for GGA exchange-correlation functionals, the bandgaps for CZTS and CZTSe are underestimated by 0.5 – 0.7 eV with respect to their experimental values (1.45 eV and 1.0

eV, respectively).[38] The bandgaps for the alloys fall between those for CZTS and CZTSe and decrease monotonically with increasing Se concentration. The calculated bandgaps for $Cu_2ZnSn(S_{1-x}Se_x)_4$ alloys are plotted in Figure 7.3 and show close adherence to Vegard's law,[39]

$$E_g^{CZTSSe} = (1-x)E_g^{CZTS} + xE_g^{CZTSe} + bx(1-x)$$

where b is the bowing constant and E_g^j is the band gap of material j. Fitting a parabola through the calculated bandgap values gives b=0.03 eV, denoting a nearly linear dependence of the bandgap on the composition. This is consistent with experimental data, which also shows a nearly linear dependence of E_g on x with b=0.08 eV.[37]

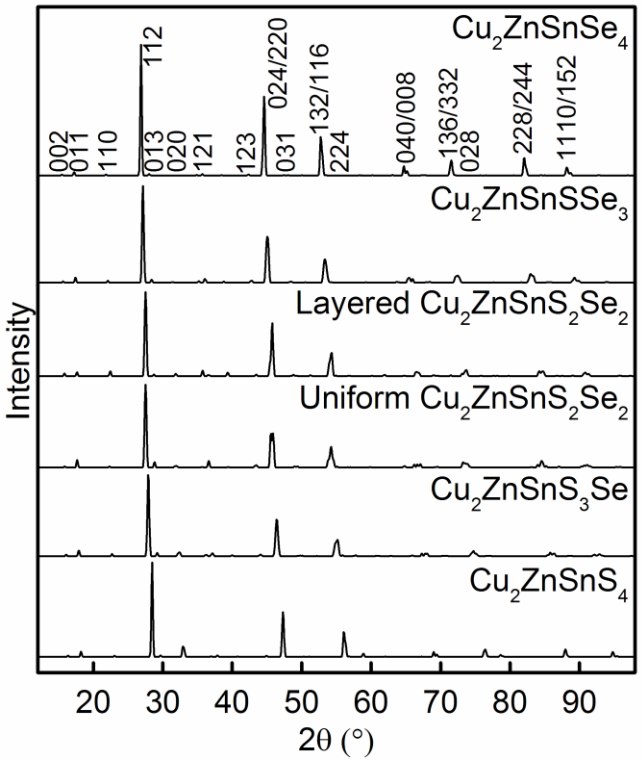

Figure 7.2 X-ray diffraction patterns of CZTSSe alloys simulated using CrystalMaker® with the lattice parameters obtained from the DFT calculations (Table 7.1). A crystallite size of 50 nm was used for the simulations. The individual diffraction patterns have been offset for clarity.

The electronic band structure of CZTSSe alloys is sensitive to the S-to-Se ratio and the disposition of the S and Se atoms (Figure 7.4). While all the alloys show a direct bandgap at the Γ-point, the structure changes subtly depending on x. In CZTS, CZTSe, and all the alloys, the top of the valence band (VB) is split by the crystal field into three branches: V_1, V_2 and V_3. The relative energies of the three branches are listed in Table 7.2. In CZTS and CZTSe, two of the three VBs are degenerate because of the kesterite structure's symmetry. In both CZTS and CZTSe, the doubly degenerate bands (V_2 and V_3) have a slightly lower energy than V_1. The energy difference between these split levels is larger in CZTS than in CZTSe, in agreement with previous calculations.[19,21] The degeneracy disappears in the case of CZTSSe and all valence bands lie at different energy levels (Table 7.2). In the uniform $Cu_2ZnSnS_2Se_2$ structure, the energy gap between V_1 and V_2 is >120 meV but decreases to 37 meV for the layered $Cu_2ZnSnS_2Se_2$ structure. Table 7.2 also lists the effective electron and hole masses for the different CZTSSe alloys. The effective hole mass along the transverse direction is higher for a layered $Cu_2ZnSnS_2Se_2$ as compared to uniform $Cu_2ZnSnS_2Se_2$. Thus, the ordering of the anions in CZTSSe affects the valence band splitting and the effective hole masses of the material. However, it may be a challenge to experimentally control or manipulate the anion ordering, especially given the fact that CZTSSe solar cells are typically fabricated using techniques such as sputtering, evaporation, or solution-based processing which do not permit control over cation or anion ordering.

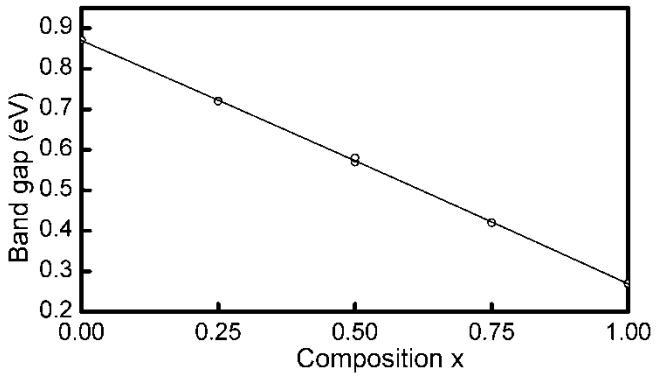

Figure 7.3 Calculated bandgap of $Cu_2ZnSn(S_{1-x}Se_x)_4$ as a function of x.

Figure 7.5 shows the atom-resolved density of states (DOS) for CZTSSe alloys. In all alloys, the valence band is mainly made up of the hybridization of the Cu-d states with the S-p and the Se-p states, with contributions from the Sn-p and the Zn-d states at lower energies. The conduction band is made up of the hybridization of the Sn-s with the S-p and Se-p states, with contributions from the Sn-p, the S-s, and the Cu-s states at higher energies. The projections of the S-p and Se-p states nearly overlap each other for all the CZTSSe alloys and the S and Se anions have very similar contributions to the electronic structure of the crystal. The layering of S and Se within the unit cell does not significantly alter the DOS because the atom-resolved DOS for the uniform and the layered $Cu_2ZnSnS_2Se_2$ structures appear very similar.

Table 7.2 Energy difference between the three valence band branches in CZTSSe alloys. Δ_{ij} is the energy difference between the branches V_i and V_j. m^t and m^l give the Γ-point effective electron (m_e) and hole (m_h) masses. The hole mass is determined using the topmost valence band (V_1). The transverse masses (m^t) are determined using the energy dispersions in both the (010) and (110) directions, and the longitudinal masses (m^l) are determined using the energy dispersion in the (001) direction.

Material	Δ_{12} (meV)	Δ_{23} (meV)	Δ_{13} (meV)	m_h^t	m_h^l	m_e^t	m_e^l
Cu_2ZnSnS_4	94.8	0	94.8	0.25	0.042	0.032	0.03
Cu_2ZnSnS_3Se	89.5	51.4	140.9	0.185	0.036	0.027	0.025
Uniform $Cu_2ZnSnS_2Se_2$	120.4	23.9	144.3	0.128	0.03	0.023	0.021
Layered $Cu_2ZnSnS_2Se_2$	37	92.3	129.3	0.211	0.023	0.021	0.021
$Cu_2ZnSnSSe_3$	88.2	42.0	130.2	0.137	0.02	0.017	0.015
$Cu_2ZnSnSe_4$	80.7	0	80.7	0.18	0.012	0.012	0.012

Figure 7.6 shows the phonon dispersion for the CZTSSe alloys along the high symmetry points (Z-Γ-N-X'-Γ-X). Qualitatively, the phonon modes in the 50 – 150 cm^{-1} wavenumber range are similar for all the alloys. However, the phonon modes above 150 cm^{-1} shift to higher frequencies as Se atoms are replaced with lighter S atoms within the

unit cell. The phonon dispersions, in general, exhibit different LO-TO splitting along different directions making some of the phonon modes discontinuous at the zone center. The phonon dispersions for the uniform and the layered $Cu_2ZnSnS_2Se_2$ structures are similar. However, a close examination reveals subtle differences. In particular, the layered $Cu_2ZnSnS_2Se_2$ has two phonon modes in the 300 – 350 cm^{-1} range that are nearly degenerate along the X'-Γ direction (inclusive of the Γ-point), while they are split by 12 cm^{-1} in the case of the uniform $Cu_2ZnSnS_2Se_2$ structure. Measuring the phonon dispersions in this energy range could distinguish between the uniform and the layered $Cu_2ZnSnS_2Se_2$ structures if they can ever be made and isolated.

Figure 7.7 shows the partial and total phonon DOS for CZTSSe alloys. The phonon states in the 50-150 cm^{-1} range are mainly comprised of the vibrations of the Cu, Zn, and Sn cations along with minor contributions from the S and Se anions. This is the underlying reason behind the similarities in the phonon dispersions in the 50-150 cm^{-1} range for all the CZTSSe alloys considered in this study. The Se anions contribute to the phonon states in the 170 – 250 cm^{-1} range whereas S anions dominate the phonon DOS in the 230 – 370 cm^{-1} range. The phonon DOS for Se in Cu_2ZnSnS_3Se consists of a series of sharp intense peaks at 173, 203, and 229 cm^{-1} which also involve vibrations of the Cu, Zn, and Sn cations, respectively. Similar intense peaks are also observed in the phonon DOS of the other CZTSSe structures. These peaks have been marked in the phonon dispersion for Cu_2ZnSnS_3Se and $Cu_2ZnSnSSe_3$ structures with C, Z, and T, respectively. These peak frequencies change only by a few wavenumbers as Se content increases from Cu_2ZnSnS_3Se to $Cu_2ZnSnSe_4$. The atomic mass of Se (79 amu) is close to those of Cu (63.5 amu), Zn (65.5 amu), and Sn (118.7 amu). For this reason all four ions vibrate in a similar energy range and their motions couple to each other leading to phonons at specific frequencies. S-based modes do not show any significant coupling with the cation modes because S (32.0 amu) is significantly lighter than all the other ions: the vibrational modes of S are at higher frequencies and do not involve any significant contribution from the heavier ions. The total phonon density of states for the uniform and layered $Cu_2ZnSnS_2Se_2$ are similar for frequencies below 200 cm^{-1} but differ in the 200-300 cm^{-1}

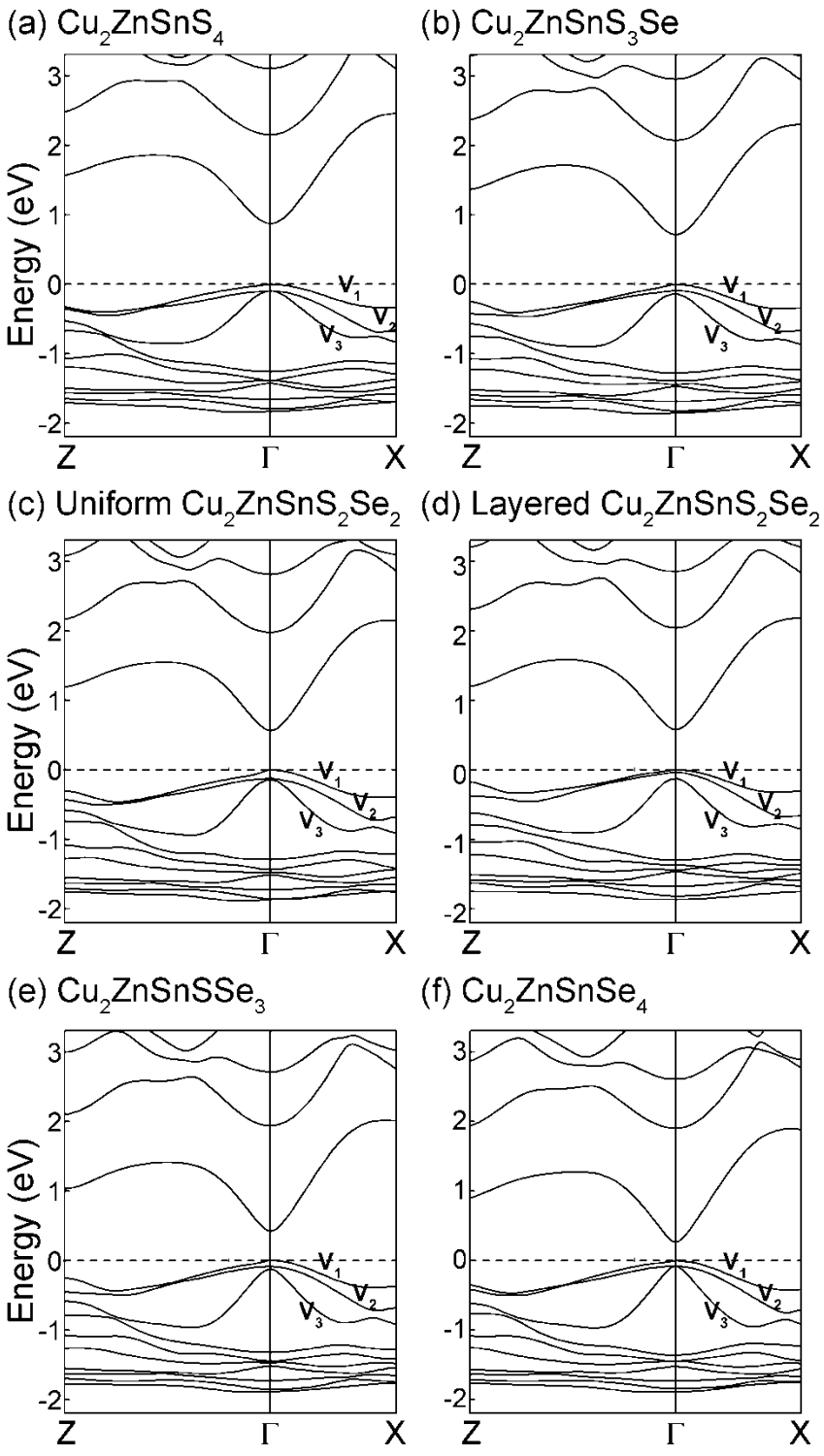

Figure 7.4 Electronic band structure of CZTSSe alloys presented with a 0.004 Ry Gaussian broadening. The energy reference is set to the VB maximum. All the structures show direct bandgaps.

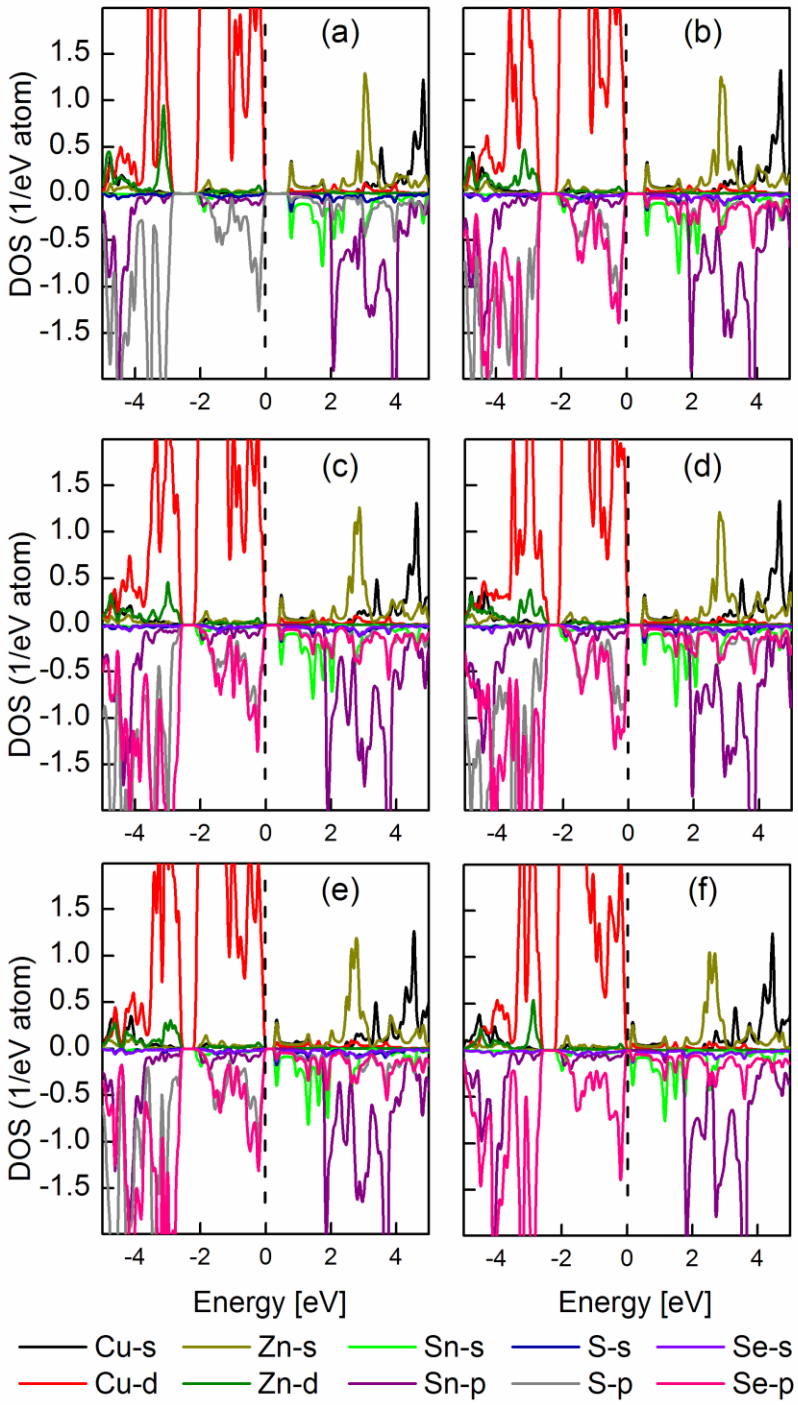

Figure 7.5 Atom-resolved electronic DOS of (a) Cu_2ZnSnS_4, (b) Cu_2ZnSnS_3Se, (c) Uniform $Cu_2ZnSnS_2Se_2$, (d) Layered $Cu_2ZnSnS_2Se_2$, (e) $Cu_2ZnSnSSe_3$, and (f) $Cu_2ZnSnSe_4$. The energy reference is set to the VB maximum (dashed vertical line).

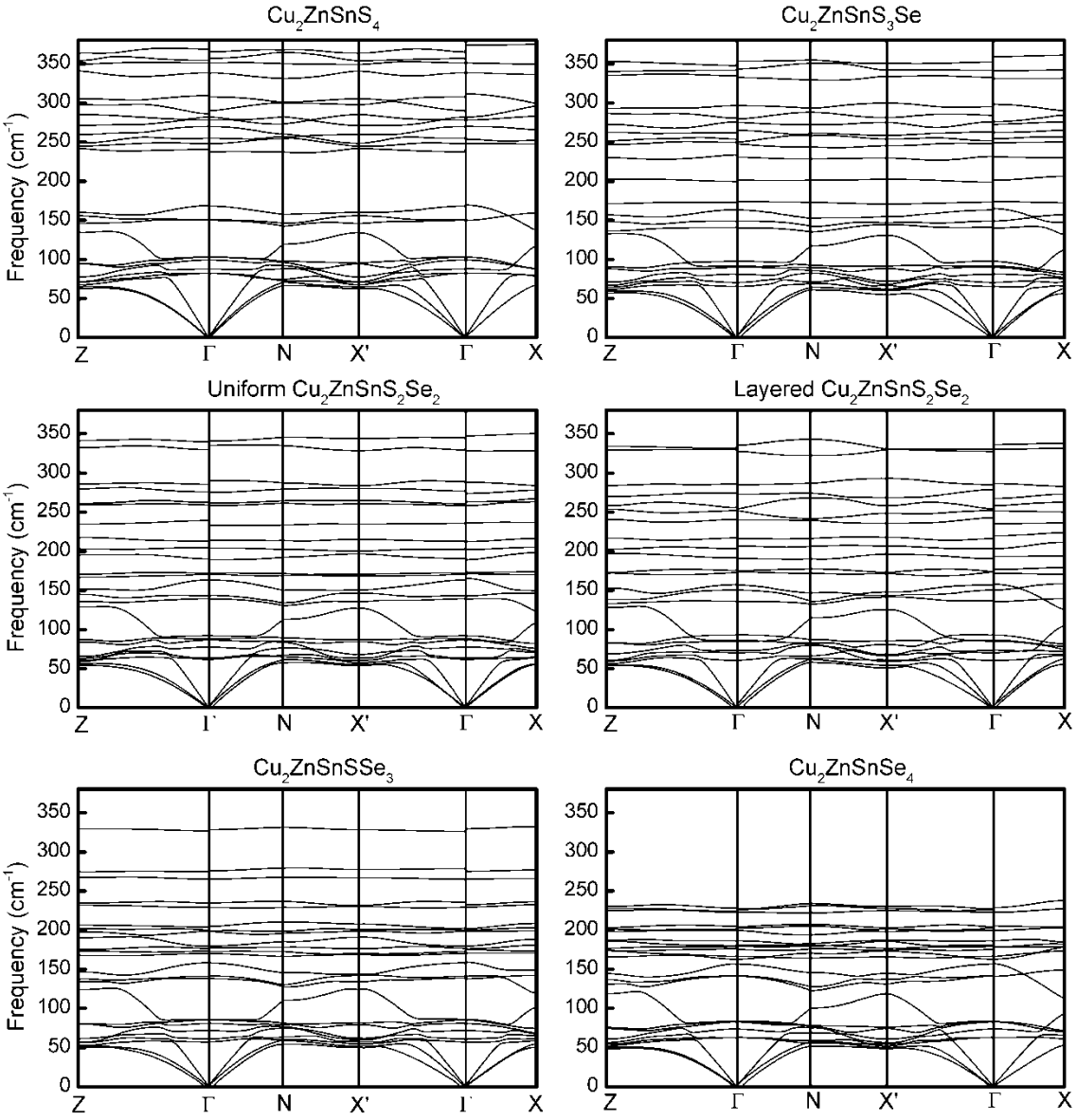

Figure 7.6 Phonon dispersion curves of CZTSSe alloys along the high symmetry points Z(0.5,0.5,0.5) - Γ(0,0,0) - N(0.5,0,0) - X'(0.5, 0.5,0) – Γ(0,0,0) – X(0,0,0.5).

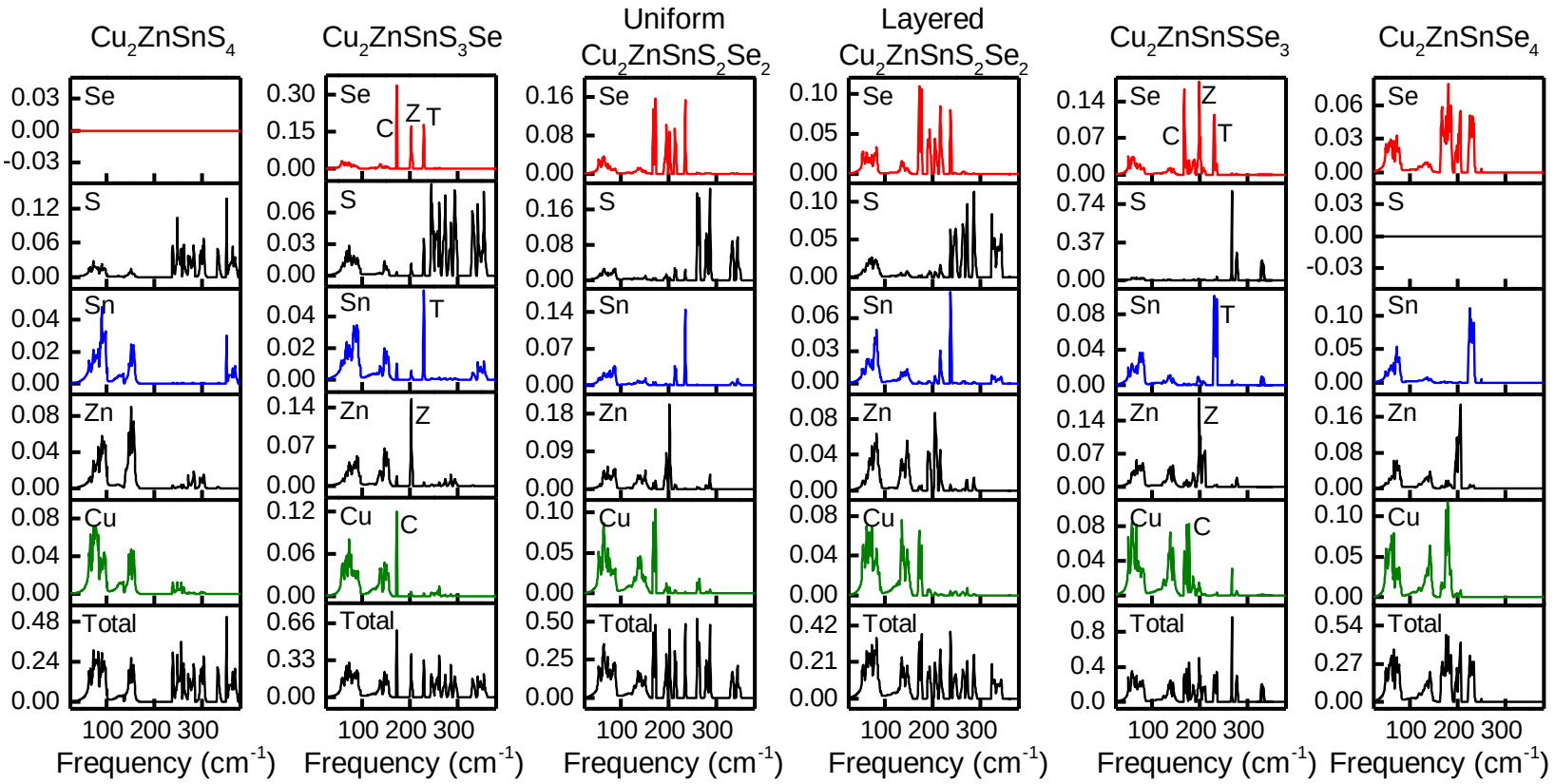

Figure 7.7 Atom-resolved phonon density of states of CZTSSe alloys.

range. Specifically, the sharp peaks corresponding to the S anion vibration in the uniform $Cu_2ZnSnS_2Se_2$ structure broaden in the layered $Cu_2ZnSnS_2Se_2$ structure because of the difference in the anion arrangement.

Raman spectroscopy probes the optical phonon modes at the zone centre and has been shown to be a valuable tool for detecting impurity phases within CZTS and CZTSe thin films.[22,23] The optical modes at the Γ point can be calculated using group theory and the crystal's symmetry, which for kesterite structure gives,[40,41] using Mulliken notation, $\Gamma=3A+6B+6E^1+6E^2$. Amongst these modes, 12 B, E^1, and E^2 modes are infrared active and 15 A, B, E^1, and E^2 modes are Raman active. For the layered $Cu_2ZnSnS_2Se_2$ structure (space group P2), $\Gamma=9A+12B$. All these 21 modes are both infrared and Raman active. The A modes in kesterite CZTS and CZTSe involve only the anion vibrations and they have been assigned to the most intense lines observed in the experimental Raman spectra of these materials.[20,29,42] The Raman spectra of CZTSSe alloys are complicated and change with composition.[2,37,43]

To gain a better understanding of the Raman spectra for CZTSSe alloys, we examined the sensitivity of the Raman scattering peak position on x and the dispositions of the anions within the unit cell. Table 7.3 shows a compilation of the Γ-point phonon frequencies for CZTSSe alloys. The CZTSSe alloys have eight atoms per primitive unit cell which results in 24 vibrational modes, 3 acoustic and 21 optical. All phonon modes in CZTSSe alloy structures involve vibrations of both the cations and the anions, and therefore, exhibit LO-TO splitting which is responsible for the discontinuities in the frequency of the optical modes at the Γ-point. The most intense Raman scattering peaks in the experimental Raman spectrum of CZTS and CZTSe are at 338 cm^{-1} and 196 cm^{-1}, respectively, and are attributed to the A mode vibrations of the anions. The experimentally measured CZTSSe Raman spectrum has two intense scattering peaks, one close to the 338 cm^{-1} mode of CZTS and another close to the 196 cm^{-1} mode of CZTSe.[2,37,43] These peaks have been attributed by He *et al.* to the scattering from vibrations involving the S and Se anions, respectively.[37] He *et al.* observed two intense peaks at 328 and 212 cm^{-1} in $Cu_2ZnSnS_{0.92}Se_{3.08}$ (x= 0.77) which, hereafter, are referred to as the high and low frequency peaks, respectively. The low frequency peak shifted

towards higher frequencies as x decreased, eventually reaching to 234 cm^{-1}, for $Cu_2ZnSnS_{2.76}Se_{1.24}$ (x=0.31).[37] In contrast the high frequency peak barely shifted and was observed at 330 cm^{-1} for $Cu_2ZnSnS_{2.76}Se_{1.24}$ (x=0.31). Because the tetragonal symmetry of CZTS and CZTSe is lost in CZTSSe alloys, it is not possible to attribute the CZTSSe Raman scattering peaks to the mode symmetries of the tetragonal structures (*e.g.*, A mode peak in the case of CZTS or CZTSe). However, a comparison of the frequencies of the Γ-point phonons for CZTSSe (Table 7.3) with the experimental Raman spectra reported in References 2, 37, and 43 reveals that some of the predicted phonon modes are very close to the experimentally observed intense CZTSSe Raman scattering peaks. The CZTSSe Γ-point phonon modes with frequencies close to the experimentally observed low and high frequency Raman scattering peaks have been marked in Table 7.3 with # and *, respectively. These peaks show shifts similar to those observed experimentally. The low frequency Raman scattering peak (marked with # in Table 7.3), shifts from 200 cm^{-1} for x=0.75 to 230 cm^{-1} for x=0.25. This is similar to the shifts observed by He *et al.* where the low frequency mode shifted from 212 cm^{-1} to 234 cm^{-1}. Vibrations associated with these peaks involve mainly the motions of S and Se with major contribution from Sn for x=0.25 and x=0.50 and Zn for x=0.75. Consistent with the experimental Raman spectra, the high frequency Raman scattering peak (marked with * in Table 7.3) barely shifts and is observed between 326 cm^{-1} and 335 cm^{-1} for $0.25 \leq x \leq 0.75$. This high frequency mode mainly involves the vibrations of Sn and S (minor components from other cations are always present). This explains the insensitivity of this mode to x. In contrast, the lower frequency Raman scattering peak position depends on x because this mode involves both S and Se vibrations. All the Raman scattering peaks have a major contribution from at least one of the cations and, for this reason, their frequencies are expected to be sensitive to cation stoichiometry.

The Raman scattering peaks in CZTSSe alloys exhibit LO-TO splitting. Considering the magnitudes of the LO-TO splitting (up to ~7 cm^{-1}) shown in Table 7.3, Raman scattering from a polycrystalline sample may be broadened. One would, therefore, expect the Raman scattering peaks for CZTSSe to be broader than CZTS or CZTSe due to variations in cation-anion disorder, crystallite orientation, and sample stoichiometry.

Table 7.3 Γ-point phonon frequencies (in cm^{-1}) for the kesterite structures of CZTSSe alloys. Sym refers to the symmetry mode of the particular vibration. The phonon frequencies matching the experimental Raman scattering peaks have been made bold and marked with # (closer to A mode of CZTSe) and * (closer to A mode of CZTS).

Cu_2ZnSnS_4			Cu_2ZnSnS_3Se		Uniform $Cu_2ZnSnS_2Se_2$		Layered $Cu_2ZnSnS_2Se_2$			$Cu_2ZnSnSSe_3$		$Cu_2ZnSnSe_4$		
TO	**LO**	**Sym**	**TO**	**LO**	**TO**	**LO**	**TO**	**LO**	**Sym**	**TO**	**LO**	**TO**	**LO**	**Sym**
82.2	82.2	E	65.4 70.5	65.4 70.5	61.7 63.4	61.7 63.4	60.5 70.4	60.7 70.4	B A	57.1 60.8	57.2 60.9	62.6	62.7	E
87.8	88.2	B	81.0	81.4	77.3	77.6	73.6	73.8	B	71.6	71.7	73.6	73.8	B
99.3	99.3	B	89.9	89.9	86.4	86.5	85.0	85.0	B	80.7	80.8	82.8	82.9	B
102.9	103.0	E	91.6 97.5	91.6 97.6	87.9 92.2	87.9 92.2	86.4 93.1	86.4 93.3	A B	85.4 85.6	85.5 85.6	83.0	83.5	E
150.0	150.5	E	140.1 149.1	140.4 149.2	139.0 142.6	139.0 143.4	135.5 150.3	135.6 150.3	B B	137.8 141.3	137.9 141.6	141.1	141.8	E
168.2	169.5	B	163.1	165.0	162.8	165.4	156.8	157.9	A	158.1	159.2	156.7	157.3	B
237.9	253.7	B	172.6	174.1	170.4	171.2	172.0	173.9	A	170.1	170.8	162.8		A
247.8	254.8	E	198.7 228.3#	201.1 230.8#	171.7 189.0	173.1 189.1	173.9 190.3	176.8 193.4	B A	172.8 175.3	175.3 177.9	166.5 175.3	178.7	A B
270.0		A	247.3	249.3	199.3	203.9	203.3	206.7	B	179.3	179.7	179.0	180.5	E
278.0	290.3	E	249.7 260.7	254.0 265.0	212.3# 233.0	214.3# 236.2	215.8# 235.1	219.9# 239.8	A B	198.4 199.1	199.1 200.1	186.3#		A
281.7		A	272.7	275.1	257.6	258.3	251.6	251.9	B	200.8#	204.8#	199.8	202.8	E
307.6	311.4	B	275.8	279.4	260.8	263.3	254.3	258.3	A	228.9	229.6			
338.5*		A	295.1	298.2	273.6	275.2	267.3	272.7	B	229.8	234.8	204.2	205.4	B
351.1	365.3	E	330.1* 341.2	332.3* 343.6	285.3 328.0*	290.3 335.3*	285.0 327.7*	286.5 330.2*	A A	264.9 273.8	265.5 275.9	222.8	226.2	E
357.0	373.6	B	347.5	359.1	339.8	347.4	330.2	336.3	B	326.2*	329.6*	227.1	228.8	B

All these factors will contribute to broadening of the Raman peaks. In fact, experimentally observed CZTSSe Raman scattering peaks are significantly broader than the corresponding peaks for CZTS or CZTSe.[2,37,43]

7.4 Summary and Conclusions

We studied the structural, electronic, and vibrational properties of $Cu_2ZnSn(S_{1-x}Se_x)_4$ alloys as a function of x using *ab initio* calculations. All of the alloys have a direct bandgap at the center of the Brillouin zone whose size decreases with x following Vegard's law. In $Cu_2ZnSn(S_{1-x}Se_x)_4$ alloys, the top of the valence band is split into three non-degenerate levels. The energy differences between the split levels and hole masses vary with x and anion disposition. $Cu_2ZnSnS_2Se_2$ has two different arrangements of the S and Se atoms: in one structure the S and Se atoms are layered while in another they are homogeneously distributed. XRD can be used to distinguish between these two different arrangements of S and Se within the unit cell by comparing the relative intensities of the (220) and (112) diffraction peaks. The predicted Raman scattering frequencies and their behavior with x agree with experimentally determined values and trends. In CZTSSe alloys, the low frequency Raman scattering peak shifts from ~200 cm^{-1} for x=0.75 to 230 cm^{-1} for x=0.25 because this vibration involves the metal atoms, S, and Se. In contrast, the high frequency peak at ~330 cm^{-1} is insensitive to x because it involves only the S and Sn atoms. The most intense scattering peaks in CZTSSe Raman spectrum involve the vibrations of all the atoms in the crystal (cations and anions) and exhibit LO-TO splitting. This is in contrast with CZTS and CZTSe where the most intense Raman peak is entirely due to the vibration of the anions. The LO-TO splitting, due to the simultaneous involvement of cations and anions, makes the Raman peak position sensitive to the cation stoichiometry, cation-anion disorder, and orientation of crystalline planes. In a polycrystalline sample, these differences lead to the broadening of the Raman peaks.

7.5 References

1 C. A. Wolden, J. Kurtin, J. B. Baxter, I. Repins, S. E. Shaheen, J. T. Torvik, A. A. Rockett, V. M. Fthenakis, and E. S. Aydil, J. Vac. Sci. Technol. A **29**, 030801 (2011).
2 D. B. Mitzi, O. Gunawan, T. K. Todorov, K. Wang, and S. Guha, Sol. Energy Mater. Sol. Cells **95**, 1421 (2011).
3 H. Katagiri, K. Jimbo, W. S. Maw, K. Oishi, M. Yamazaki, H. Araki, and A. Takeuchi, Thin Solid Films **517**, 2455 (2009).
4 W. Shockley, and H. J. Queisser, J. Appl. Phys. **32**, 510 (1961).
5 T. K. Todorov, K. B. Reuter, and D. B. Mitzi, Adv. Mater. **22**, E156 (2010).
6 Q. Guo, G. M. Ford, W. Yang, B. C. Walker, E. A. Stach, H. W. Hillhouse, and R. Agrawal, J. Am. Chem. Soc. **132**, 17384 (2010).
7 Y. Wang, and H. Gong, J. Electrochem. Soc. **158**, H800 (2011).
8 K. Moriya, K. Tanaka, and H. Uchiki, Jpn. J. Appl. Phys. **46**, 5780 (2007).
9 K. Jimbo, R. Kimura, T. Kamimura, S. Yamada, W. S. Maw, H. Araki, K. Oishi, and H. Katagiri, Thin Solid Films **515**, 5997 (2007).
10 K. Wang, O. Gunawan, T. Todorov, B. Shin, S. J. Chey, N. A. Bojarczuk, D. Mitzi, and S. Guha, Appl. Phys. Lett. **97**, 143508 (2010).
11 H. Araki, A. Mikaduki, Y. Kubo, T. Sato, K. Jimbo, W. S. Maw, H. Katagiri, M. Yamazaki, K. Oishi, and A. Takeuchi, Thin Solid Films **517**, 1457 (2008).
12 Q. Guo, H. W. Hillhouse, and R. Agrawal, J. Am. Chem. Soc. **131**, 11672 (2009).
13 C. Steinhagen, M. G. Panthani, V. Akhavan, B. Goodfellow, B. Koo, and B. A. Korgel, J. Am. Chem. Soc. **131**, 12554 (2009).
14 A. Khare, A. W. Wills, L. M. Ammerman, D. J. Norris, and E. S. Aydil, Chem. Commun. **47**, 11721 (2011).
15 V. G. Rajeshmon, C. S. Kartha, K. P. Vijayakumar, C. Sanjeeviraja, T. Abe, and Y. Kashiwaba, Sol. Energy **85**, 249 (2011).
16 W. Ki, and H. W. Hillhouse, Adv. Energy Mater. **1**, 732 (2011).
17 A. Ennaoui, M. Lux-Steiner, A. Weber, D. Abou-Ras, I. Kötschau, H. -. Schock, R. Schurr, A. Hölzing, S. Jost, R. Hock, T. Voß, J. Schulze, and A. Kirbs, Thin Solid Films **517**, 2511 (2009).
18 D. A. R. Barkhouse, O. Gunawan, T. Gokmen, T. K. Todorov, and D. B. Mitzi, Prog. Photovolt: Res. Appl. **20**, 6 (2012).
19 S. Chen, X. G. Gong, A. Walsh, and S. Wei, Appl. Phys. Lett. **94**, 041903 (2009).
20 A. Khare, B. Himmetoglu, M. Johnson, D. J. Norris, M. Cococcioni, and E. S. Aydil, J. Appl. Phys. **111**, 083707 (2012).
21 C. Persson, J. Appl. Phys. **107**, 053710 (2010).
22 A. J. Cheng, M. Manno, A. Khare, C. Leighton, S. A. Campbell, and E. S. Aydil, J. Vac. Sci. Technol. A **29**, 051203 (2011).
23 P. A. Fernandes, P. M. P. Salome, and A. F. da Cunha, Thin Solid Films **517**, 2519 (2009).
24 S. Chen, J. Yang, X. G. Gong, A. Walsh, and S. Wei, Phys. Rev. B **81**, 245204 (2010).

25 J. Paier, R. Asahi, A. Nagoya, and G. Kresse, Phys. Rev. B **79**, 115126 (2009).
26 A. Nagoya, R. Asahi, R. Wahl, and G. Kresse, Phys. Rev. B **81**, 113202 (2010).
27 N. B. Mortazavi Amiri, and A. Postnikov, Phys. Rev. B **82**, 205204 (2010).
28 S. Chen, A. Walsh, J. Yang, X. G. Gong, L. Sun, P. Yang, J. Chu, and S. Wei, Phys. Rev. B **83**, 125201 (2011).
29 T. Gurel, C. Sevik, and T. Cagin, Phys. Rev. B **84**, 205201 (2011).
30 P. Hohenberg, and W. Kohn, Phys. Rev. **136**, B864 (1964).
31 W. Kohn, and L. J. Sham, Phys. Rev. **140**, A1133 (1965).
32 D. Vanderbilt, Phys. Rev. B **41**, 7892 (1990).
33 P. Giannozzi, S. Baroni, N. Bonini, M. Calandra, R. Car, C. Cavazzoni, D. Ceresoli, G. L. Chiarotti, M. Cococcioni, I. Dabo, A. D. Corso, S. d. Gironcoli, S. Fabris, G. Fratesi, R. Gebauer, U. Gerstmann, C. Gougoussis, A. Kokalj, M. Lazzeri, L. Martin-Samos, N. Marzari, F. Mauri, R. Mazzarello, S. Paolini, A. Pasquarello, L. Paulatto, C. Sbraccia, S. Scandolo, G. Sclauzero, A. P. Seitsonen, A. Smogunov, P. Umari, and R. M. Wentzcovitch, J. Phys. : Condens. Matter **21**, 395502 (2009).
34 J. P. Perdew, K. Burke, and M. Ernzerhof, Phys. Rev. Lett. **77**, 3865 (1996).
35 H. J. Monkhorst, and J. D. Pack, Phys. Rev. B **13**, 5188 (1976).
36 S. Baroni, S. de Gironcoli, A. Dal Corso, and P. Giannozzi, Rev. Mod. Phys. **73**, 515 (2001).
37 J. He, L. Sun, S. Chen, Y. Chen, P. Yang, and J. Chu, J. Alloys Compd. **511**, 129 (2012).
38 A. Seidl, A. Gorling, P. Vogl, J. A. Majewski, and M. Levy, Phys. Rev. B **53**, 3764 (1996).
39 L. Vegard, Zeitschrift Für Physik A Hadrons and Nuclei **5**, 17 (1921).
40 M. I. Aroyo, J. Perez-Mato, C. Capillas, E. Kroumova, S. Ivantchev, G. Madariaga, A. Kirov, and H. Wondratschek, Z. Kristallogr. **221**, 15 (2006).
41 P. K. Sarswat, M. L. Free, and A. Tiwari, Phys. Status Solidi (b) **248**, 2170 (2011).
42 M. Himmrich, and H. Haeuseler, Spectrochim. Acta Part A: Mol. Spectrosc. **47**, 933 (1991).
43 M. Grossberg, J. Krustok, J. Raudoja, K. Timmo, M. Altosaar, and T. Raadik, Thin Solid Films **519**, 7403 (2011).

Bibliography

A. Ennaoui, M. Lux-Steiner, A. Weber, D. Abou-Ras, I. Kötschau, H. Schock, R. Schurr, A. Hölzing, S. Jost, R. Hock, T. Voß, J. Schulze, and A. Kirbs, Thin Solid Films **517**, 2511 (2009).

A. J. Cheng, M. Manno, A. Khare, C. Leighton, S. A. Campbell, and E. S. Aydil, J. Vac. Sci. Technol. A **29**, 051203 (2011).

A. Khare, A. W. Wills, L. M. Ammerman, D. J. Norris, and E. S. Aydil, Chem. Commun. **47**, 11721 (2011).

A. Khare, B. Himmetoglu, M. Johnson, D. J. Norris, M. Cococcioni, and E. S. Aydil, J. Appl. Phys. **111**, 083707 (2012).

A. Kongkanand, K. Tvrdy, K. Takechi, M. Kuno, and P. V. Kamat, J. Am. Chem. Soc. **130**, 4007 (2008).

A. L. Efros, and A. L. Efros, Sov. Phys. Semicond. **16**, 772 (1982).

A. Moholkar, S. S. Shinde, A. R. Babar, K. Sim, H. K. Lee, K. Y. Rajpure, P. S. Patil, C. H. Bhosale, and J. H. Kim, J. Alloys Compd. **509**, 7439 (2011).

A. Nagoya, R. Asahi, R. Wahl, and G. Kresse, Phys. Rev. B **81**, 113202 (2010).

A. Nozik, Physica E **14**, 115 (2002).

A. Pattantyus-Abraham, I. J. Kramer, A. R. Barkhouse, X. Wang, G. Konstantatos, R. Debnath, L. Levina, I. Raabe, M. K. Nazeeruddin, M. Grätzel, and E. H. Sargent, ACS Nano **4**, 3374 (2010).

A. Seidl, A. Gorling, P. Vogl, J. A. Majewski, and M. Levy, Phys. Rev. B **53**, 3764 (1996).

A. Singh, H. Geaney, F. Laffir, and K. M. Ryan, J. Am. Chem. Soc. **134**, 2910 (2012).

A. Weber, H. Krauth, S. Perlt, B. Schubert, I. Koetschau, S. Schorr, and H. W. Schock, Thin Solid Films **517**, 2524 (2009).

A. Weber, R. Mainz, and H. W. Schock, J. Appl. Phys. **107**, 013516 (2010).

B. Schubert, B. Marsen, S. Cinque, T. Unold, R. Klenk, S. Schorr, and H. Schock, Prog. Photovolt: Res. Appl. **19**, 93 (2011).

C. A. Wolden, J. Kurtin, J. B. Baxter, I. Repins, S. E. Shaheen, J. T. Torvik, A. A. Rockett, V. M. Fthenakis, and E. S. Aydil, J. Vac. Sci. Technol. A **29**, 030801 (2011).

C. Persson, J. Appl. Phys. **107**, 053710 (2010).

C. Platzer-Björkman, J. Scragg, H. Flammersberger, T. Kubart, and M. Edoff, Sol. Energy Mater. Sol. Cells **98**, 110 (2012).

C. Steinhagen, M. G. Panthani, V. Akhavan, B. Goodfellow, B. Koo, and B. A. Korgel, J. Am. Chem. Soc. **131**, 12554 (2009).

C. Wadia, A. P. Alivisatos, and D. M. Kammen, Environ. Sci. Technol. **43**, 2072 (2009).

D. A. R. Barkhouse, O. Gunawan, T. Gokmen, T. K. Todorov, and D. B. Mitzi, Prog. Photovolt: Res. Appl. **20**, 6 (2012).

D. B. Mitzi, O. Gunawan, T. K. Todorov, K. Wang, and S. Guha, Sol. Energy Mater. Sol. Cells **95**, 1421 (2011).

D. B. Mitzi, T. K. Todorov, O. Gunawan, Min Yuan, Qing Cao, Wei Liu, K. B. Reuter, M. Kuwahara, K. Misumi, A. J. Kellock, S. J. Chey, T. G. de Monsabert, A. Prabhakar, V. Deline, and K. E. Fogel, in *Proceedings of the 35th IEEE Photovoltaic Specialists Conference* (IEEE, 2010), pp. 640–645.

D. Bersani, P. P. Lottici, and X. Z. Ding, Appl. Phys. Lett. **72**, 73 (1998).

D. Pan, X. Wang, H. Zhou, W. Chen, C. Xu, and Y. Lu, Chemistry of Materials **21**, 2489 (2009).

D. Vanderbilt, Phys. Rev. B **41**, 7892 (1990).

G. Ma, T. Minegishi, D. Yokoyama, J. Kubota, and K. Domen, Chem. Phys. Lett. **501**, 619 (2011).

G. S. Babu, Y. B. K. Kumar, P. U. Bhaskar, and V. S. Raja, Semicond. Sci. Technol. **23**, 085023 (2008).

G. Zoppi, I. Forbes, R. W. Miles, P. J. Dale, J. J. Scragg, and L. M. Peter, Prog. Photovolt: Res. Appl. **17**, 315 (2009).

H. Araki, Y. Kubo, K. Jimbo, W. S. Maw, H. Katagiri, M. Yamazaki, K. Oishi, and A. Takeuchi, Phys. Status Solidi C **6**, 1266 (2009).

H. J. Monkhorst, and J. D. Pack, Phys. Rev. B **13**, 5188 (1976).

H. Katagiri, K. Jimbo, K. Moriya, and K. Tsuchida, Osaka, Japan (2003), pp. 2874.

H. Katagiri, K. Jimbo, M. Tahara, H. Araki, and K. Oishi, in *Mater. Res. Soc. Symp. Proc. 1165* (2009), pp. 1165-M04-01.

H. Katagiri, K. Jimbo, S. Yamada, T. Kamimura, W. S. Maw, T. Fukano, T. Ito, and T. Motohiro, Appl. Phys. Express **1**, 041201/1 (2008).

H. Katagiri, K. Jimbo, W. S. Maw, K. Oishi, M. Yamazaki, H. Araki, and A. Takeuchi, Thin Solid Films **517**, 2455 (2009).

H. Katagiri, K. Saitoh, T. Washio, H. Shinohara, T. Kurumadani, and S. Miyajima, Sapporo, Japan (1999) pp. 647.

H. Katagiri, K. Saitoh, T. Washio, H. Shinohara, T. Kurumadani, and S. Miyajima, Sol. Energy Mater. Sol. Cells **65**, 141 (2001).

H. Katagiri, N. Ishigaki, T. Ishida, and K. Saito, Jpn. J. Appl. Phys. **40**, 500 (2001).

H. Katagiri, N. Sasaguchi, S. Hando, S. Hoshino, J. Ohashi, and T. Yokota, Miyazaki, Japan (1996) pp. 745.

H. Katagiri, N. Sasaguchi, S. Hando, S. Hoshino, J. Ohashi, and T. Yokota, Sol. Energy Mater. Sol. Cells **49**, 407 (1997).

H. Katagiri, Thin Solid Films **480-481**, 426 (2005).

H. Wang, Int. J. Photoenergy **2011**, 801292 (2011).

I. D. Olekseyuk, L. D. Gulay, I. V. Dydchak, L. V. Piskach, O. V. Parasyuk, and O. V. Marchuk, J. Alloys Compd. **340**, 141 (2002).

J. B. Li, V. Chawla, and B. M. Clemens, Adv. Mater. **24**, 720 (2012).

J. B. Sambur, T. Novet, and B. A. Parkinson, Science **330**, 63 (2010).

J. He, L. Sun, S. Chen, Y. Chen, P. Yang, and J. Chu, J. Alloys Compd. **511**, 129 (2012).

J. J. Scragg, D. M. Berg, and P. J. Dale, J. Electroanal. Chem. **646**, 52 (2010).

J. J. Scragg, P. J. Dale, and L. M. Peter, Thin Solid Films **517**, 2481 (2009).

J. J. Scragg, P. J. Dale, L. M. Peter, G. Zoppi, and I. Forbes, Phys. Status Solidi B **245**, 1772 (2008).

J. M. Luther, P. K. Jain, T. Ewers, and A. P. Alivisatos, Nat. Mater. **10**, 361 (2011).

J. Madarász, P. Bombicz, M. Okuya, and S. Kaneko, Solid State Ionics **141–142**, 439 (2001).

J. P. Perdew, K. Burke, and M. Ernzerhof, Phys. Rev. Lett. **77**, 3865 (1996).

J. Paier, R. Asahi, A. Nagoya, and G. Kresse, Phys. Rev. B **79**, 115126 (2009).

K. Ito, and T. Nakazawa, Jpn. J. Appl. Phys. **27**, 2094 (1988).

K. Jimbo, R. Kimura, T. Kamimura, S. Yamada, W. S. Maw, H. Araki, K. Oishi, and H. Katagiri, Thin Solid Films **515**, 5997 (2007).

K. Maeda, K. Tanaka, Y. Fukui, and H. Uchiki, Sol. Energy Mater. Sol. Cells **95**, 2855 (2011).

K. Maeda, K. Tanaka, Y. Nakano, and H. Uchiki, Jpn. J. Appl. Phys. **50**, 05FB08 (2011).

K. Moriya, K. Tanaka, and H. Uchiki, Jpn. J. Appl. Phys. **46**, 5780 (2007).

K. Ramasamy, M. A. Malik, and P. O'Brien, Chem. Sci. **2**, (2011).

K. S. Leschkies, R. Divakar, J. Basu, E. Enache-Pommer, J. E. Boercker, C. B. Carter, U. R. Kortshagen, D. J. Norris, and E. S. Aydil, Nano Lett. **7**, 1793 (2007).

K. S. Leschkies, T. J. Beatty, M. S. Kang, D. J. Norris, and E. S. Aydil, ACS Nano **3**, 3638 (2009).

K. Tanaka, M. Oonuki, N. Moritake, and H. Uchiki, Sol. Energy Mater. Sol. Cells **93**, 583 (2009).

K. Tanaka, N. Moritake, and H. Uchiki, Sol. Energy Mater. Sol. Cells **91**, 1199 (2007).

K. Tanaka, Y. Fukui, N. Moritake, and H. Uchiki, Sol. Energy Mater. Sol. Cells **95**, 838 (2011).

K. Wang, O. Gunawan, T. Todorov, B. Shin, S. J. Chey, N. A. Bojarczuk, D. Mitzi, and S. Guha, Appl. Phys. Lett. **97**, 143508 (2010).

K. Woo, Y. Kim, and J. Moon, Energy Environ. Sci. **5**, 5340 (2012).

L. E. Brus, J. Chem. Phys. **80**, 4403 (1984).

L. Shi, C. Pei, Y. Xu, and Q. Li, J. Am. Chem. Soc. **133**, 10328 (2011).

L. Vegard, Zeitschrift Für Physik A Hadrons and Nuclei **5**, 17 (1921).

M. Altosaar, J. Raudoja, K. Timmo, M. Danilson, M. Grossberg, J. Krustok, and E. Mellikov, Phys. Status Solidi A **205**, 167 (2008).

M. Bar, B. Schubert, B. Marsen, S. Krause, S. Pookpanratana, T. Unold, L. Weinhardt, C. Heske, and H. Schock, Appl. Phys. Lett. **99**, 152111 (2011).

M. G. Panthani, V. Akhavan, B. Goodfellow, J. P. Schmidtke, L. Dunn, A. Dodabalapur, P. F. Barbara, and B. A. Korgel, J. Am. Chem. Soc. **130**, 16770 (2008).

M. Grossberg, J. Krustok, J. Raudoja, K. Timmo, M. Altosaar, and T. Raadik, Thin Solid Films **519**, 7403 (2011).

M. Himmrich, and H. Haeuseler, Spectrochim. Acta Part A: Mol. Spectrosc. **47**, 933 (1991).

M. I. Aroyo, J. Perez-Mato, C. Capillas, E. Kroumova, S. Ivantchev, G. Madariaga, A. Kirov, and H. Wondratschek, Z. Kristallogr. **221**, 15 (2006).

M. T. Htay, Y. Hashimoto, N. Momose, K. Sasaki, H. Ishiguchi, S. Igarashi, K. Sakurai, and K. Ito, Jpn. J. Appl. Phys. **50**, 032301 (2011).

N. B. Mortazavi Amiri, and A. Postnikov, Phys. Rev. B **82**, 205204 (2010).

N. Kamoun, H. Bouzouita, and B. Rezig, Thin Solid Films **515**, 5949 (2007).

N. Momose, M. T. Htay, T. Yudasaka, S. Igarashi, T. Seki, S. Iwano, Y. Hashimoto, and K. Ito, Jpn. J. Appl. Phys. **50**, 01BG09 (2011).

N. Nakayama, and K. Ito, Appl. Surf. Sci. **92**, 171 (1996).

O. E. Semonin, J. M. Luther, S. Choi, H. Chen, J. Gao, A. J. Nozik, and M. C. Beard, Science **334**, 1530 (2011).

O. Gunawan, T. K. Todorov, and D. B. Mitzi, Appl. Phys. Lett. **97**, 233506 (2010).

P. A. Fernandes, P. M. P. Salome, and A. F. da Cunha, Thin Solid Films **517**, 2519 (2009).

P. Dai, X. Shen, Z. Lin, Z. Feng, H. Xu, and J. Zhan, Chem. Commun. **46**, 5749 (2010).

P. Fernandes, P. M. P. Salome, and A. F. da Cunha, Semicond. Sci. Technol. **24**, 105013 (2009).

P. Giannozzi, S. Baroni, N. Bonini, M. Calandra, R. Car, C. Cavazzoni, D. Ceresoli, G. L. Chiarotti, M. Cococcioni, I. Dabo, A. D. Corso, S. d. Gironcoli, S. Fabris, G. Fratesi, R. Gebauer, U. Gerstmann, C. Gougoussis, A. Kokalj, M. Lazzeri, L. Martin-Samos, N. Marzari, F. Mauri, R. Mazzarello, S. Paolini, A. Pasquarello, L. Paulatto, C. Sbraccia, S. Scandolo, G. Sclauzero, A. P. Seitsonen, A. Smogunov, P. Umari, and R. M. Wentzcovitch, J. Phys. : Condens. Matter **21**, 395502 (2009).

P. Hohenberg, and W. Kohn, Phys. Rev. **136**, B864 (1964).

P. K. Sarswat, M. L. Free, and A. Tiwari, Phys. Status Solidi B **248**, 2170 (2011).

P. M. P. Salomé, P. A. Fernandes, and A. F. da Cunha, Phys. Status Solidi C **7**, 913 (2010).

Q. Guo, G. M. Ford, W. Yang, B. C. Walker, E. A. Stach, H. W. Hillhouse, and R. Agrawal, J. Am. Chem. Soc. **132**, 17384 (2010).

Q. Guo, H. W. Hillhouse, and R. Agrawal, J. Am. Chem. Soc. **131**, 11672 (2009).

Q. Liu, Z. Zhao, Y. Lin, P. Guo, S. Li, D. Pan, and X. Ji, Chem. Commun. **47**, 964 (2011).

R. B. V. Chalapathy, G. S. Jung, and B. T. Ahn, Sol. Energy Mater. Sol. Cells **95**, 3216 (2011).

R. D. Deegan, O. Bakajin, T. F. Dupont, G. Huber, S. R. Nagel, and T. A. Witten, Nature **389**, 827 (1997).

R. Schurr, A. Hölzing, S. Jost, R. Hock, T. Voβ, J. Schulze, A. Kirbs, A. Ennaoui, M. Lux-Steiner, A. Weber, I. Kötschau, and H. -. Schock, Thin Solid Films **517**, 2465 (2009).

R. W. G. Wyckoff, Crystal Structures, (Wiley, New York, 1963), pp. 110.

S. Ahmed, K. B. Reuter, O. Gunawan, L. Guo, L. T. Romankiw, and H. Deligianni, Adv. Energy Mater. **2**, 253 (2012).

S. Ahn, S. Jung, J. Gwak, A. Cho, K. Shin, K. Yoon, D. Park, H. Cheong, and J. H. Yun, Appl. Phys. Lett. **97**, 021905 (2010).

S. Baroni, S. de Gironcoli, A. Dal Corso, and P. Giannozzi, Rev. Mod. Phys. **73**, 515 (2001).

S. C. Riha, B. A. Parkinson, and A. L. Prieto, J. Am. Chem. Soc. **131**, 12054 (2009).

S. Chen, A. Walsh, J. Yang, X. G. Gong, L. Sun, P. Yang, J. Chu, and S. Wei, Phys. Rev. B **83**, 125201 (2011).

S. Chen, J. Yang, X. G. Gong, A. Walsh, and S. Wei, Phys. Rev. B **81**, 245204 (2010).

S. Chen, X. G. Gong, A. Walsh, and S. Wei, Appl. Phys. Lett. **94**, 041903 (2009).

S. M. Pawar, B. S. Pawar, A. V. Moholkar, D. S. Choi, J. H. Yun, J. H. Moon, S. S. Kolekar, and J. H. Kim, Electrochim. Acta **55**, 4057 (2010).

S. R. Hall, J. T. Szymanski, and J. M. Stewart, Can. Mineral. **16**, 131 (1978).

S. Schorr, H. Hoebler, and M. Tovar, Eur. J. Mineral. **19**, 65 (2007).

T. A. Witten, and L. M. Sander, Phys. Rev. Lett. **47**, 1400 (1981).

T. Franzl, T. A. Klar, S. Schietinger, A. L. Rogach, and J. Feldmann, Nano Lett. **4**, 1599 (2004).

T. Gurel, C. Sevik, and T. Cagin, Phys. Rev. B **84**, 205201 (2011).

T. K. Todorov, K. B. Reuter, and D. B. Mitzi, Adv. Mater. **22**, E156 (2010).

T. M. Friedlmeier, N. Wieser, T. Walter, H. Dittrich, and H. W. Schock, Belford, UK (1997), pp. 1242.

T. Maeda, S. Nakamura, and T. Wada, Jpn. J. Appl. Phys. **50**, 04DP07 (2011).

T. Prabhakar, and N. Jampana, Sol. Energy Mater. Sol. Cells **95**, 1001 (2011).

T. Sekine, M. Izumi, T. Nakashizu, K. Uchinokura, and E. Matsuura, J. Phys. Soc. Jpn. **49**, 1069 (1980).

T. Tanaka, A. Yoshida, D. Saiki, K. Saito, Q. Guo, M. Nishio, and T. Yamaguchi, Thin Solid Films **518**, S29 (2010).

T. Tanaka, D. Kawasaki, M. Nishio, Q. Guo, and H. Ogawa, Phys. Status Solidi C **3**, 2844 (2006).

T. Tanaka, T. Nagatomo, D. Kawasaki, M. Nishio, Q. Guo, A. Wakahara, A. Yoshida, and H. Ogawa, J. Phys. Chem. Solids **66**, 1978 (2005).

T. Todorov, M. Kita, J. Carda, and P. Escribano, Thin Solid Films **517**, 2541 (2009).

T. Todorov, O. Gunawan, S. J. Chey, T. G. de Monsabert, A. Prabhakar, and D. B. Mitzi, Thin Solid Films **519**, 7378 (2011).

T. Washio, T. Shinji, S. Tajima, T. Fukano, T. Motohiro, K. Jimbo, and H. Katagiri, J. Mater. Chem. **22**, 4021 (2012).

U.S. Energy Information Administration, *Annual Energy Outlook* (U.S. Department of Energy, Washington, DC, 2011).

U.S. Energy Information Administration, *International Energy Outlook* (U.S. Department of Energy, Washington, DC, 2011).

V. G. Rajeshmon, C. S. Kartha, K. P. Vijayakumar, C. Sanjeeviraja, T. Abe, and Y. Kashiwaba, Sol. Energy **85**, 249 (2011).

V. I. Klimov, Nanocrystal Quantum Dots, (CRC Press, 2009).

W. A. Tisdale, K. J. Williams, B. A. Timp, D. J. Norris, E. S. Aydil, and X. Y. Zhu, Science **328**, 1543 (2010).

W. Ki, and H. W. Hillhouse, Adv. Energy Mater. **1**, 732 (2011).

W. Kohn, and L. J. Sham, Phys. Rev. **140**, A1133 (1965).

W. P. Lee, and A. F. Routh, Langmuir **20**, 9885 (2004).

W. Shockley, and H. J. Queisser, J. Appl. Phys. **32**, 510 (1961).

W. U. Huynh, J. J. Dittmer, and A. P. Alivisatos, Science **295**, 2425 (2002).

X. Chen, H. Wada, A. Sato, and M. Mieno, J. Solid State Chem. **139**, 144 (1998).

X. Lu, Z. Zhuang, Q. Peng, and Y. Li, Chem. Commun. **47**, 3141 (2011).

Y. B. K. Kumar, P. U. Bhaskar, G. S. Babu, and V. S. Raja, Phys. Status Solidi A **207**, 149 (2010).

Y. K. Jung, J. I. Kim, and J. K. Lee, J. Am. Chem. Soc. **132**, 178 (2010).

Y. Wang, and H. Gong, J. Electrochem. Soc. **158**, H800 (2011).